An investigation into the grid compliance of the slip synchronous permanent magnet wind generator

by

Andries Theodorus Spies

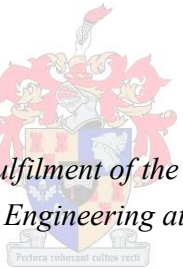

Thesis presented in partial fulfilment of the requirements for the degree Master of Science in Engineering at Stellenbosch University

Supervisor: Prof M.J. Kamper
Department of Electrical & Electronic Engineering

March 2013

Declaration

By submitting this thesis electronically, I declare that the entirety of the work contained therein is my own, original work, that I am the sole author thereof (save to the extent explicitly otherwise stated), that reproduction and publication thereof by Stellenbosch University will not infringe any third party rights and that I have not previously in its entirety or in part submitted it for obtaining any qualification.

Date: March 2013

Summary

The slip synchronous permanent magnet generator (SSG) is a direct-driven direct-grid connected generator developed to alleviate the need for expensive gearboxes and solid-state power converters on wind turbine generators. This study identifies certain key areas where the current wind turbine generator (WTG) system does not comply with the grid code for wind energy facilities (WEF) as specified by the National Energy Regulator of South Africa.

The current WTG system does not have a reactive power compensation device. The main focus in this study is the development of an on-load tap changer (OLTC) transformer to control the terminal voltage of the generator. By controlling the terminal voltage of the generator the excitation-mode of the SSG can be changed allowing for control over the reactive power output of the SSG. An OLTC transformer utilising a solid-state assisted mechanical diverter circuit is built and tested to determine the viability of using an OLTC as a reactive power control device.

Practical test results show that the OLTC can successfully control the terminal voltage of the SSG without interrupting the load current. The required accuracy regarding power factor control capability was not met due to the large change in reactive power output per tap change operation. A method of using small shunt capacitor banks to provide additional reactive power in between consecutive tap changes is evaluated in simulation. Simulation results show that the addition of these small shunt capacitor banks dramatically improves the reactive power control accuracy.

Additionally the grid code specifies that a WEF must have the ability to curtail the active power output during frequency disturbances. The effects of frequency disturbances on the SSG output is simulated and it was found that the SSG will comply with the minimum connection requirements as specified in the grid code. A method of using an IGBT switched DC load to limit the active power output of the WEF is developed and simulated. From the simulation results it was found that the proposed active power curtailment device will meet the minimum power curtailment response time requirements as specified in the grid code.

Opsomming

Die glip sinchroon permanente magneet generator (SSG) is 'n direkte dryf, direkte netwerk gekoppelde wind generator wat ontwikkel is om behoefte aan duur ratkaste en drywing elektroniese omsetters te verlig. Hierdie studie identifiseer sekere sleutel areas waar die huidige wind generator opstelling nie aan die netwerk kode spesifikasie soos uiteengesit deur die Nasionale Energie Reguleerder van Suid-Afrika voldoen nie.

Die wind turbine generator stelsel beskik nie oor 'n reaktiewe drywing beheer meganisme nie. Die belangrikste fokus in hierdie studie is die ontwikkeling van 'n transformator tap wisselaar wat gebruik sal word om die generator se terminale spanning te beheer. Deur die terminaal spanning te beheer kan die opwekking modus van die generator verander word om dan die uittree reaktiewe drywing te beheer. 'n Tap wisselaar wat gebruik maak van 'n drywingelektronies gesteunde meganiese skakelaar is ontwikkel en getoets om die lewensvatbaarheid van die tegniek te ondersoek.

Praktiese toets resultate toon dat die tap wisselaar suksesvol beheer oor die generator se terminaal spanning kon uitvoer, sonder om die las-stroom te onderbreuk. Ongelukkig is die vereiste akkuraatheid ten opsigte van die reaktiewe drywing beheer nie gehaal nie. Die rede hiervoor is dat die verandering in uittree reaktiewe drywing baie groot is vir opeenvolgende tap verstellings. 'n Metode waar twee klein kapasitor banke geskakel word om reaktiewe drywing te lewer, tussen opeenvolgende tap veranderinge, is deur middel van simulasie ondersoek. Die simulasie resultate toon aan dat die toevoeging van die kapasitors 'n drastiese verbetering in die beheerbaarheid van die uittree reaktiewe drywing het.

Verder spesifiseer die netwerk kode ook dat 'n wind plaas oor die vermoë moet beskik om die aktiewe drywing te verminder tydens 'n netwerk frekwensie versteuring. Die effek wat 'n frekwensie versteuring op die SSG het, is deur middel van simulasie ondersoek en daar is gevind dat die SSG aan die netwerk verbinding spesifikasie sal voldoen. 'n Metode waarby 'n IGBT geskakelde GS las gebruik word om die aktiewe drywing van die wind generator te beperk is ondersoek en gesimuleer. Vanaf die simulasie resultate is daar gevind dat die drywing beperkings toestel aan die minimum drywing en reaksie tyd spesifikasies soos vereis sal voldoen.

Acknowledgements

I would like to thank the following people:

- my supervisor Prof Kamper for his guidance throughout this study,
- the technical personnel and students working at the EMLab for all the times they came to give me a helping hand and
- my parents for all the support and guidance throughout my studies,
- and finally a special thanks to my close friends and flatmate, Hendrik Odendal, for sitting with me in the lab till late at night so that I could complete my practical tests.

Finally I thank God for giving me the blessings I have received that allows me to follow my dream.

Table of Content

List of Figures

List of Tables

List of Symbols

Symbol	Description	Unit
Generic Quantities:		
J	Inertia	kg.m^2
N	Turns	#
p	Poles	#
P	Active power	W
Q	Reactive power	var
T	Torque	N.m.
Z	Impedance	Ω
C	Capacitance	F
E	Induced voltage	V
I	Current	A
L	Inductance	H
R	Resistance	Ω
V	Voltage	V
X	Reactance	Ω
f	Frequency	Hz
θ	Power factor angle	degrees or rad
ω	Frequency	rad/s
Magnetic Quantities:		
$\mathcal{F}$	Motor motive force (MMF)	A.turns
$\mathcal{R}$	Reluctance	A.Wb^{-1}
Φ	Magnetic flux	Wb
A	Cross-sectional area of conductor	m^2
B	Magnetic flux density	T
H	Magnetic field intensity	A.turns/m
l	Length of conductor	m
λ	Flux linkage	Wb/turns
μ	Permeability	H/m
ρ	Resistivity	Ω/m
General subscripts:		
1, 2	Primary and secondary	
A	Armature	
a, b, c	abc phases	
d, q	d-axis and q-axis from Park transform	
e	electrical	
eq	Equavalent	
i	Integral	
LL	Line-to-line	
m	PM-rotor	
oc	Open circuit	
p	Proportional	
r	IG-rotor	
s	SG-stator	
sc	Short circuit	
sle	Electrical slip	
t	Turbine	
α, β	Alpha and beta waveforms from Clarke transform	
ϕ	Per phase	

List of abbreviations

AC	Alternating current
DFIG	Doubly-fed induction generator
DC	Direct current
FACTS	Flexible AC transmission systems
GCC	Grid connection circuit
GS	Gelykstroom (Afrikaans translation of direct current)
IG	Induction generator
MGSV	Mentor Graphics SystemVision
MMF	Motor motive force
NERSA	National Energy Regulator of South Africa
OLTC	On-load tap changer
PF	Power factor
PM	Permanent magnet
PMIG	Permanent magnet induction generator
PMSG	Permanent magnet synchronous generators
Q	Reactive power [var]
SCIG	Squirrel cage induction generator
SG	Synchronous generator
SSG	Slip synchronous permanent magnet generator
SST	Solid-state transformer
STATCOM	Static synchronous compensator
SVC	Static VAR compensator
VHDL-AMS	Verilog Hardware Description Language – Analog and Mixed Signal
VSC	Voltage-sources converter
WEF	Wind energy facility
WTG	Wind turbine generator

Chapter 1. Introduction

This is the introductory chapter of a study regarding the technical requirements for the grid connection of a new type of electrical generator. This generator was designed for use as a wind power generator and this is the focus throughout the study.

1.1. Motivation for renewable energy research

Modern society is dependent on energy. Without large amounts of electrical energy the average household would not be able to function properly. All industrial plants require electricity and even a small disturbance in the availability of electricity has large financial implications and hampers economic growth. In short: the global economic machine requires abundant amounts of electrical energy to operate and grow. Figure 1.1 below shows the World Electrical Usage in kWh/capita, Figure 1.2 shows the World Population. Using the information from the two graphs below the total amount of electrical energy used worldwide can be calculated, the result is shown in Figure 1.3. The amount of electrical energy used in the world increases as the world population increases. If Figure 1.1 and Figure 1.4 are compared then it is clear that there is a correlation between the usage per capita and the Gross Domestic Product, GDP, per capita.

Using this information it is clear that as long as the world economy and population grows, the need for electrical energy will also increase. Traditional means of generating the electrical power we require are not sustainable. Coal power stations spew large amounts of greenhouse gasses in the atmosphere and although the process of nuclear fission does not produce any greenhouse gasses, it does produce radioactive waste that has to be disposed of carefully. Gas and oil are also used to generating electrical power. All of these sources have finite amount of fuel left and are not sustainable.

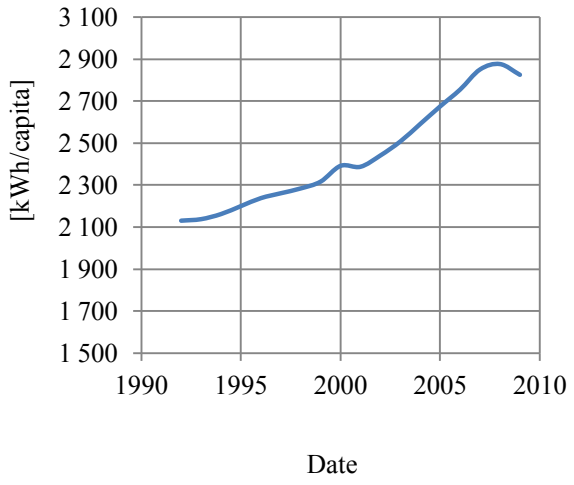

Figure 1.1: World electrical usage per capita [1].

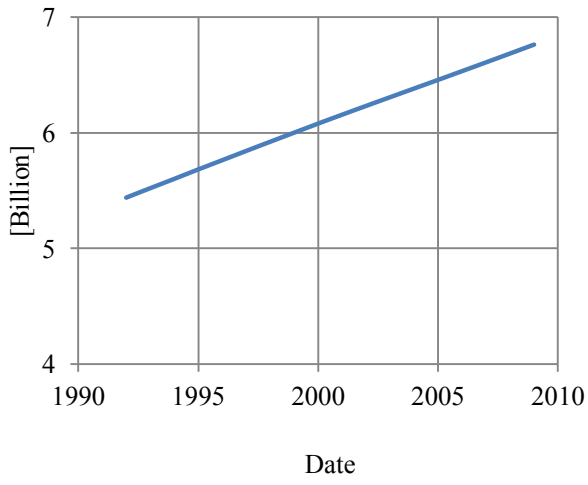

Figure 1.2: Total world population [1].

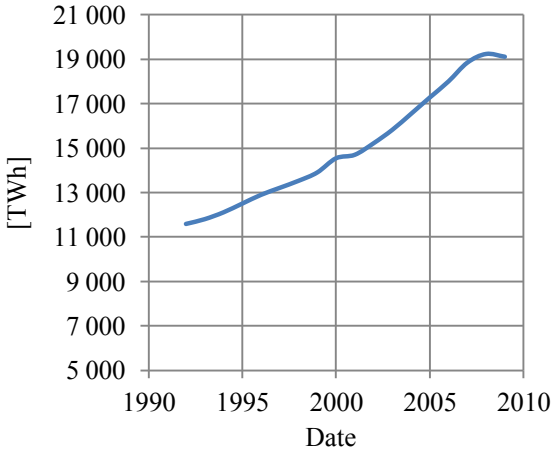

Figure 1.3: Total world electrical usage.

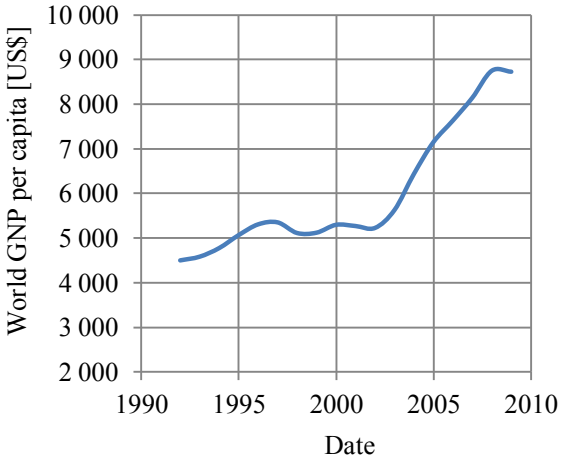

Figure 1.4: World GDP per capita [1].

1.2. Wind power generation

From all the endeavours to provide cleaner and affordable electrical energy, wind power seems to stand out as the main contender. Wind power generation is a renewable energy source and creates no emissions during operation. Figure 1.5 below shows the current installed capacity for wind power generation. Even though the world growth rate is starting to decline the trend continues that the installed wind capacity doubles every three years. Many western countries, including North America and especially European countries are showing signs of stagnation and a decrease in new installations, but due to the recent nuclear disaster in Japan and the oil spill in the Gulf of Mexico it is expected that governments will start to reinforce their wind energy policies. The World Wind Energy Association expects global capacity of 1 500 GW by 2020 [2].

Africa had an installed capacity of 906 MW during 2010, with Egypt and Morocco having the largest installed share. South Africa has a current installed capacity of about 10 MW, but 700 MW of new wind projects are expected to be installed by the year 2013. In Africa special consideration should be given to small scale rural electrification. The major barrier for wind energy in Africa is the lack of financial resources [2].

About 20% of the world population still do not have access to electricity; most of these people are situated in remote rural areas that are difficult to access. In Africa alone there are half a billion people without electricity (80% in rural areas). Small scale wind energy development has large potential in these remote areas, since it is possible to install several small turbines instead of a single large unit. In most rural or stand-alone installations, small wind turbines will form part of a hybrid power generation system creating a mini-grid. Typically wind power is combined with solar or diesel systems, depending on the demand of the client or community [3].

The South African government has just approved 562 MW of wind power projects as part of a larger renewable energy tender [4].

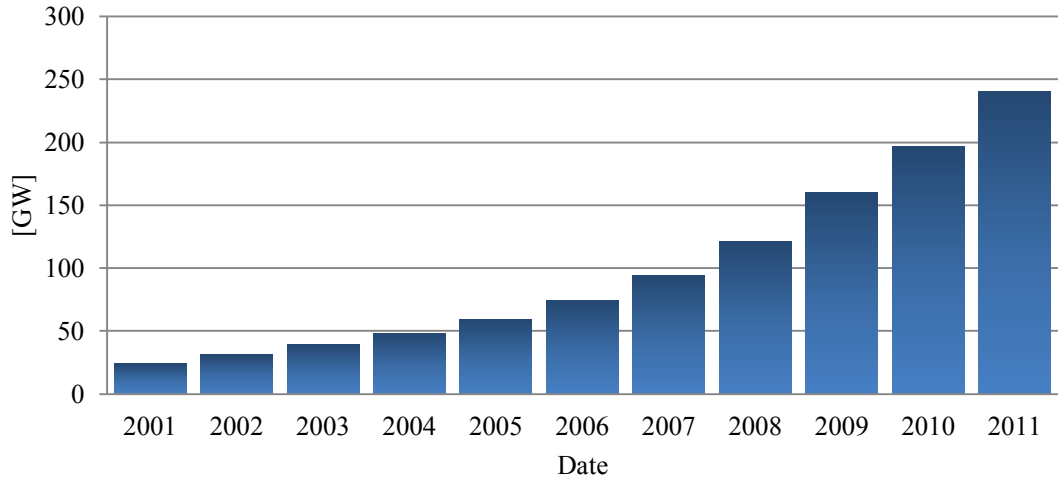

Figure 1.5: World total wind power generation installed capacity [2].

Figure 1.6: Joby airborne wind turbine (Rana 2) [5].

Figure 1.7: Altaeros airborne wind turbine [6].

1.3. Technological developments

Although wind has been used as a power source, not necessarily generating electricity, for more than a thousand years, new technology is still being developed to increase the efficiency with which power can be collected from the wind. The first "large scale" generation of electricity using wind power was built in 1888 in Cleveland, Ohio by Charles Brush. He used a windmill with a 17 meter rotor and a 50:1 gearbox to power a DC generator. Since then far more sophisticated wind power plants have been developed [7].

In recent years the wind power sector has developed many new and innovative technologies to harness the power of the wind. Companies are striving to increase blade efficiency and reduce noise and vibrations. Some companies, like Solar Aero, are even looking at bladeless wind turbines based on an old patent by Tesla. Other companies, like Joby Energy Inc and Altaeros Energies, are exploring technology to harness high altitude wind by using airborne wind turbines as shown in Figure 1.6 and Figure 1.7.

In the 1990s wind turbines commonly consisted of a gearbox and high speed asynchronous squirrel cage induction generator (SCIG) that could be directly connected to the utility grid, normally via a

step-up transformer. This concept requires reactive power for the generator. Reactive power compensation was done using a capacitor bank. A basic layout of a SCIG based WTG is shown in Figure 1.8. A soft starter was used for smooth grid connection [8]. Today this type of configuration retains less than 1% of the current world market share [9].

A popular variation of the induction generator (IG) known as doubly-fed induction generator (DFIG) can operate at variable turbine speeds, allowing for greater power collection. The stator is connected to the grid, while the rotor is connected through a power electronic converter that controls the frequency of the wound rotor. The power converter also performed reactive power compensation and allowed for smooth grid connection [8]. Figure 1.9 shows the layout for a DFIG with a partially rated converter.

Another popular configuration uses a full rated power converter connected in series with the generator to achieve full variable speed. The power converter still performs reactive power compensation and allows for smooth grid connection at any speed. Various different types of generators can be used, including SCIGs, DFIGs and permanent magnet synchronous generators (PMSG) [8]. Figure 1.10 shows the layout for various generators connected via a full rated converter. Variable-speed wind turbines with DFIGs have been the dominant technology since about 2002 [9].

The Slip Synchronous Permanent Magnet Generator (SSG) was developed to alleviate the need for heavy gearboxes and expensive power electronic converters. The direct drive permanent magnet (PM) generator allows for directly grid connectable system which is less complex and more cost effective. The PM generator designed is an induction machine mounted on a synchronous machine; more detail regarding the generator is given in Chapter 2. Figure 1.11 shows layout of the generator directly connected to a wind turbine and the grid [10][11]. The manner in which the reactive power is controlled is evaluated in this thesis. Since the machine uses PMs, the excitation and thus the reactive power consumption, can be controlled by changing the terminal voltage. Alternatively a capacitor bank(s) or some other reactive power controller could be used.

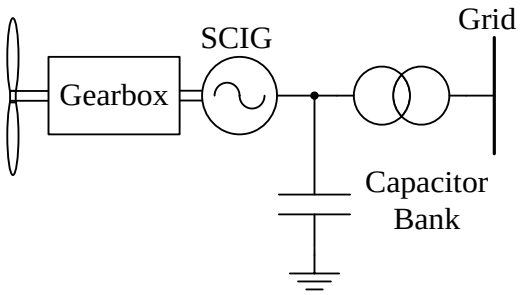

Figure 1.8: SCIG with a gearbox and capacitor bank [8].

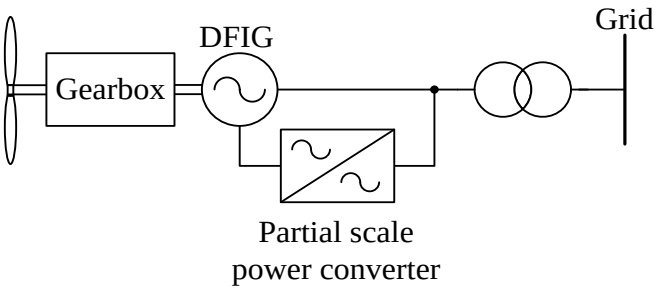

Figure 1.9: DFIG with a partially rated power converter [8].

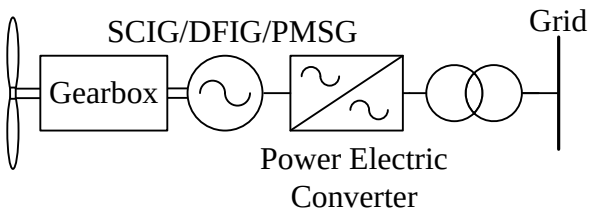

Figure 1.10: Various generator types using a gearbox and full rated power converter [8].

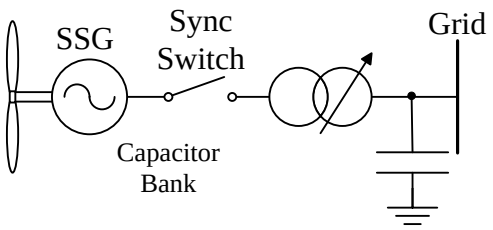

Figure 1.11: Proposed layout for a SSG based wind energy facility utilizing a tapped step up transformer with a capacitor bank connected on the MV or HV transmission line.

1.4. Problem statement

Integrating wind farms into the current electrical grid does pose some problems. Wind power generation plants tend to introduce voltage instability into electrical grids due to the uncontrollable nature of the energy source. As the wind speed increases and decreases, at irregular intervals, the output current changes. Since wind power generation plants are often situated in rural areas and connected to weak electrical grids (with low short circuit levels), large voltage variations and possible phase voltage imbalance due to added voltage instability is of huge concern [12] [13].

Reactive power is absorbed by transformers and induction machines in order to create magnetic fields. Even transmission lines are inductive. On the other hand reactive power can be provided by either using capacitor banks or operating synchronous generators under specific conditions. Excessive reactive power will cause unnecessary voltage drops on the transmission line due to the increased current magnitude [12].

It is apparent that for wind power generation to be taken seriously, the wind energy facility, WEF, must be able to connect to the national electrical grid without causing instability. Because of this natural instability caused by wind power generation most countries have specifications to which a wind power facility must comply.

The National Energy Regulator of South Africa, NERSA, is the regulatory authority regarding electricity in South Africa. NERSA has specific technical standards regarding the connection requirements for wind energy facilities (WEF). The connection requirements can be divided into five groups; frequency, voltage, power factor control, active power curtailment and low (and high) voltage ride through.

1.5. Approach

This thesis focuses on connecting a small scale slip synchronous wind turbine generator, WTG, to the electrical grid of South Africa while adhering to the technical specification of NERSA. During this study the various aspects of the Grid code (frequency, voltage, reactive power) requirement is discussed. Some aspects regarding the grid connection have been completed in a previous study [14] and [15] and the results from this study are reviewed in Chapter 3. The primary focus is the development of adequate voltage and reactive power control mechanisms. The secondary focus is the development of a suitable power curtailment device for use during frequency disturbances.

Although a small 15 kW generator is used throughout this study, the actual focus is on developing technology and techniques for wind farms utilizing generators on the megawatt scale.

1.6. Objectives

- Study the grid code of South Africa and identify areas where the SSG based WTG does not comply with the requirements.
- Propose, design, simulate and test possible solutions to these problematic areas focussing on reactive power and voltage control.
- Design, simulate and test an IGBT-based electric brake circuit for use during grid synchronisation and active power curtailment.

1.7. Thesis layout

Background regarding wind power generation and the motivation for this research is given in Chapter 1. The generator technology used throughout this study is discussed in Chapter 2, while the method by which this generator is currently connected to the grid is discussed in Chapter 3.

Chapter 4 evaluates and compares the use of a thyristor based electric braking circuit and an IGBT-rectifier braking circuit to limit the active power output of the WEF. The dynamic response of the SSG due to frequency disturbances is simulated in Chapter 5.

Various on-load tap changer transformer topologies are discussed and compared in Chapter 6. An OLTC using a solid-state assisted mechanical diverter circuit is designed and built in Chapter 7. The OLTC is modelled and simulated in Chapter 8.

A method of using the OLTC with shunt capacitor banks to control the reactive power output of the WEF is simulated in Chapter 9. The OLTC is practically tested in Chapter 10. The conclusions and recommendation follow in Chapter 11.

Chapter 2. The slip synchronous generator

The slip synchronous generator was developed in [11] to alleviate the need for heavy gearboxes and expensive power electronic solid-state converters in wind power generators systems. Although this new generator type is based upon the principles of the standard PMIG it has several advantages regarding cost, reliability and construction complexity. This chapter gives a short overview of the workings of the slip synchronous generator, and describes the mathematical model used to simulate the generator in the VHDL-AMS modelling language.

2.1. Permanent magnet induction generator working characteristics

The permanent magnet induction generator (PMIG), as shown in Figure 2.1, differs from the traditional induction generator in that the magnetisation is provided by the permanent magnets mounted on a free rotating rotor; instead of taking excitation current from the armature winding terminals [16]. Note the additional voltage source when comparing the equivalent circuits for an IG with a PMIG, Figure 2.2 and Figure 2.3. The use of permanent magnets to provide the excitation current is very beneficial to the power factor of the generator since less reactive power is needed. PMIGs also tend to be more efficient when compared to normal IGs [10].

Another advantage of the PMIG is that the IG-rotor cage can be directly connected to the prime-mover when using a large diameter, high pole generator. This means there is no need for a gearbox. A soft grid connection, without needing a solid state power converter, can be realized when using a. asynchronous induction machine with slip. Removing the gearbox and power converter is lead to lower costs and higher reliability [10].

The main drawback of the PMIG concept is the constructional complexity [10]. It is especially noted in [16] where the authors warn that due to the strong magnets special care should be taken when assembling the generator to avoid damaging the magnets or possibly injuring personnel.

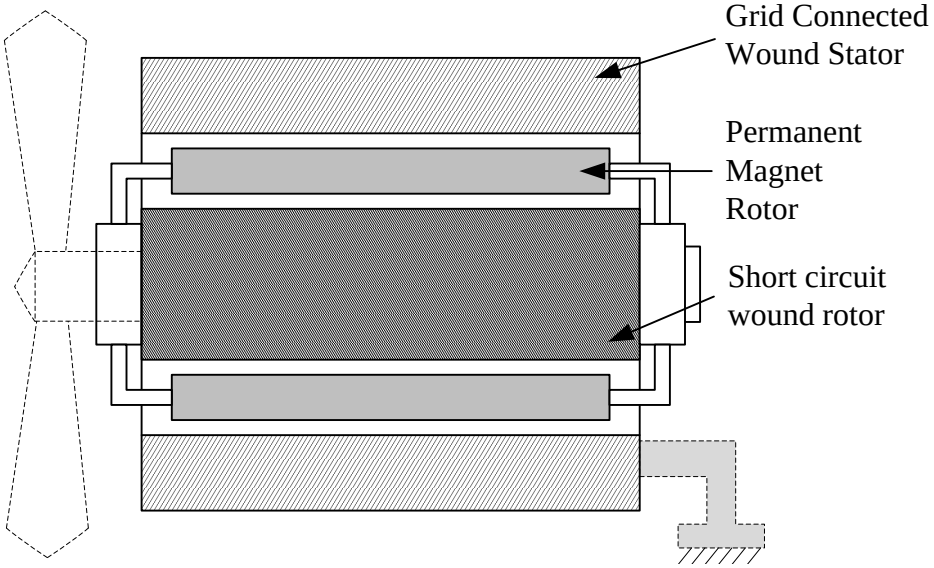

Figure 2.1: Cross-section side view of a conventional PMIG.

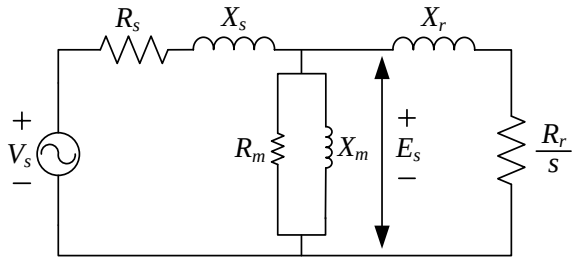

Figure 2.2: Equivalent circuit for an IG.

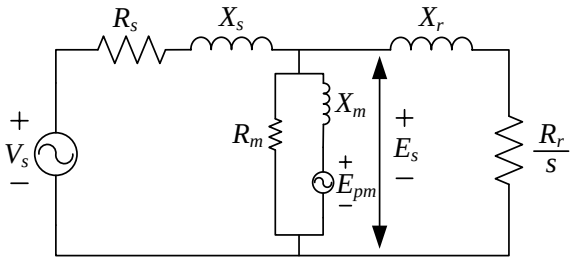

Figure 2.3: Equivalent circuit for an PMIG [10]

2.2. The slip synchronous generator concept

The slip synchronous generator (SSG), or initially called the split PMIG, is basically two PM generators linked by a free rotating PM-rotor. A side view of the SSG is shown in Figure 2.4. The equivalent circuit for the SSG is shown in Figure 2.5. The one machine is a SG with its stator connected to the grid. The other machine is an IG with its short-circuited rotor mechanically connected to the prime mover. The PM-rotor rotates at synchronous speed, as dictated by the synchronous generator (SG) pole count. The IG runs at slip speed relative to the synchronously rotating PM-rotor. The main advantage of the SSG concept is that it is much easier to construct, and the IG and SG can be designed independently [11].

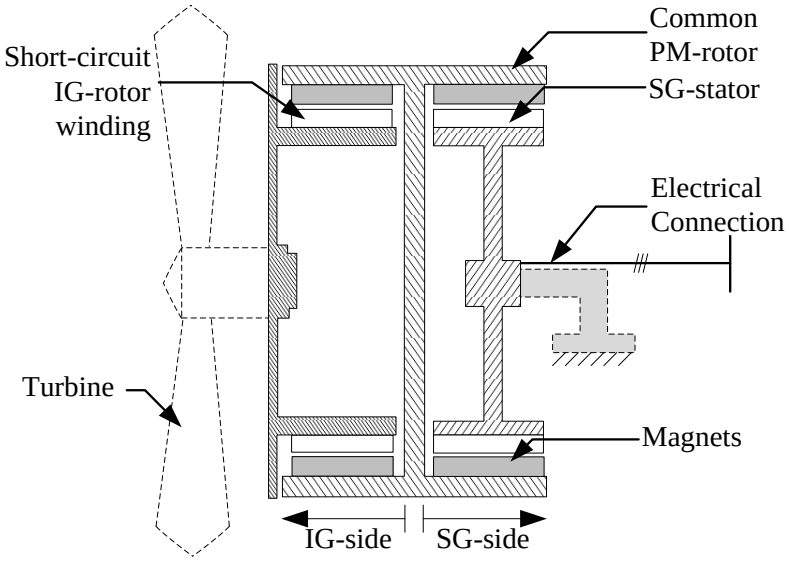

Figure 2.4: The slip synchronous permanent magnet generator.

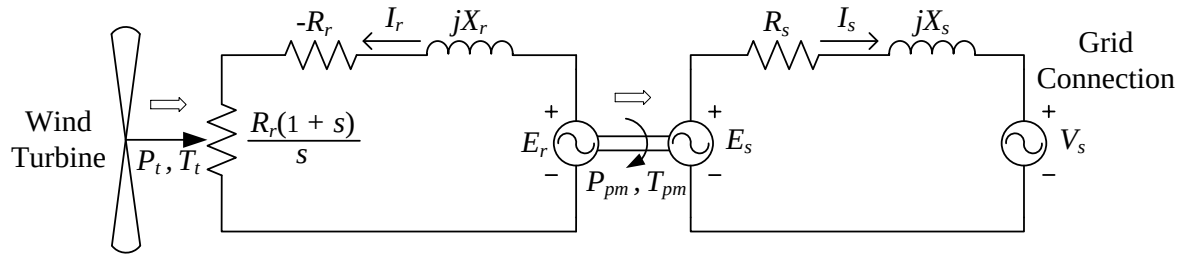

Figure 2.5: Equivalent circuit diagram for the SSG [11][17].

2.3. Dynamic modelling of the SSG

Extensive modelling of the SSG is done in [17]. As shown in Figure 2.5 the SSG can be modelled as two separate decoupled machines. Positive power flow is taken from the turbine, connected to the

short circuited IG-rotor, via the PM-rotor and SG-stator to the grid. The dq-equivalent circuit for the IG and SG is shown in Figure 2.6 to Figure 2.9. The dynamic equation describing the IG and SG respectively is given by equation (2.1) and (2.2):

$$\begin{aligned} 0 &= -i_{qr}R_r - L_{qr}\frac{di_{qr}}{dt} - \omega_{sle}L_{dr}i_{dr} + \omega_{sle}\lambda_{mr}\,, \\ 0 &= -i_{dr}R_r - L_{dr}\frac{di_{dr}}{dt} - \omega_{sle}L_{qr}i_{qr}\,, \end{aligned} \tag{2.1}$$

$$\begin{aligned} v_{qs} &= -i_{qs}R_s - L_{qs}\frac{di_{qs}}{dt} - \omega_e L_{ds}i_{ds} + \omega_e\lambda_{me}\,, \\ v_{ds} &= -i_{ds}R_s - L_{ds}\frac{di_{ds}}{dt} - \omega_e L_{qs}i_{qs}\,, \end{aligned} \tag{2.2}$$

where ω_{sle} is the electrical slip speed given in (2.3),

$$\omega_{sle} = (\omega_t - \omega_m)\frac{p}{2}\,, \tag{2.3}$$

with ω_t the turbine speed, ω_m the speed of the PM-rotor and p is the number of poles. ω_e is the electrical frequency at the stator terminals. In (2.1) and (2.2) the subscripts "r" and "s" refer to the IG-rotor and SG-stator respectively. The flux linkage due to the permanent magnets for the IG and SG are respectively λ_{mr} and λ_{ms}.

The torques generated in the IG and SG, as shown in Figure 2.4, are given by

$$T_s = \tfrac{3}{4}p\left[(L_{qs} - L_{ds})i_{ds}i_{qs} + \lambda_{ms}i_{qs}\right], \tag{2.4}$$

$$T_m = \tfrac{3}{4}p\left[(L_{qr} - L_{dr})i_{dr}i_{qr} + \lambda_{mr}i_{qr}\right], \tag{2.5}$$

where T_s is the counter torque generated in the SG and T_m is the torque acting on the PM-rotor. The dynamics of the turbine plus slip rotor, and PM-rotor is expressed in (2.6) and (2.7) as

$$T_t = T_m + J_t\frac{d\omega_t}{dt}\,, \tag{2.6}$$

$$T_m = T_s + J_m\frac{d\omega_m}{dt}\,, \tag{2.7}$$

where T_t is the torque applied on the main shaft of the IG-rotor. J_t and J_m are the inertias of the turbine, including IG-rotor, and the PM-rotor respectively. The friction losses are ignored in the model.

Using the design parameters and dynamic equations, a VHDL-AMS model for the prototype 15 kW SSG (using a single layer IG) has been created in [17]. After the publication of [17] the author also defined the parameter values for the 15 kW SSG using a double layer IG. The model parameters are given in Table 2.1 below.

Table 2.1: Model parameters for the 15 kW SSG using a double layer IG

$J_t =$	300 kg.m^2	$R_r =$	2.341 µΩ	$L_{dr} =$	0.127 µH	$L_{ds} =$	15 mH
$J_m =$	10 kg.m^2	$R_s =$	380 mΩ	$L_{qr} =$	0.09 µH	$L_{qs} =$	15 mH
$p =$	40	$f_e =$	50 Hz	$\lambda_{mr} =$	3.693 mWb	$\lambda_{ms} =$	1.0171 Wb

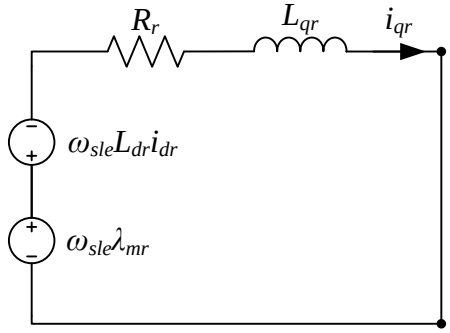

Figure 2.6: Equivalent circuit slip-rotor q-axis [17].

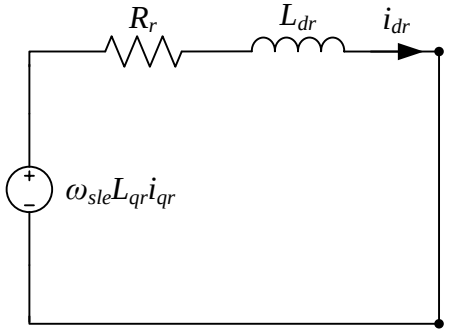

Figure 2.7: Equivalent circuit slip-rotor d-axis [17].

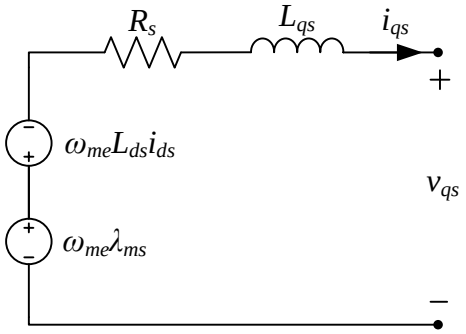

Figure 2.8: Equivalent circuit stator q-axis [17].

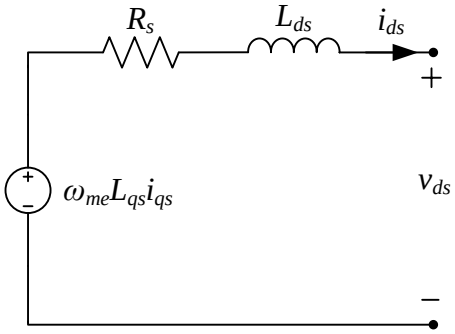

Figure 2.9: Equivalent circuit stator d-axis [17].

2.4. Simulated efficiency and power factor angle

Using the dynamic model described above the current angle (to determine power factor) and total generator efficiency is simulated for various terminal voltage levels. The simulation setup is showed in Figure 2.10. The ideal transformer is used to change the terminal voltage, V_T. The current angle of the line current, I_{line}, shown in Figure 2.11 is determined relative to the voltage angle at the generator terminals. Since the model used does not take into account the iron losses in the stator, the simulated efficiency will be much higher than the measured efficiency. Figure 2.12 shows the simulated efficiency of the generator. The efficiency is determined my comparing the input power with the active power output at the generator terminals.

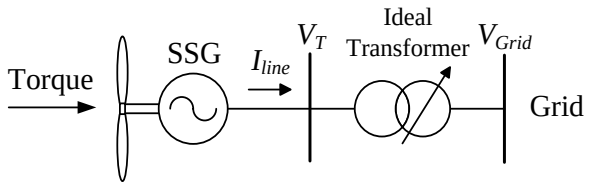

Figure 2.10: Line diagram of the circuit used during simulation and actual tests.

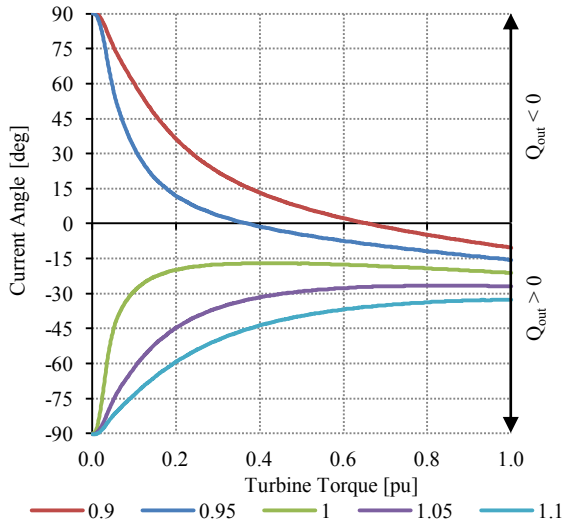

Figure 2.11: Simulated current angle of the stator with terminal voltage a parameter in per unit.

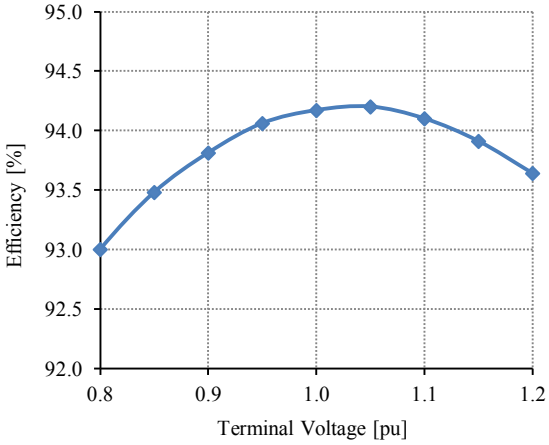

Figure 2.12: Simulated efficiency for various terminal voltages.

2.5. Conclusion regarding the response of the SSG to changes in the terminal voltage

From the simulation results it would appear that the reactive power output of the generator can be increased by decreasing the terminal voltage. The downside is that the efficiency of the SSG will decrease as the voltage decreases. The actual current angle and efficiency response to terminal voltage changes will need to be measured during testing. As previously mentioned the dynamic model used during simulation does not take into account the iron losses in the stator. This will affect the simulated efficiency.

Chapter 3. Connecting to the grid

The SSG can be connected to the grid without a solid-state power converter. The following chapter discusses the grid connection circuit (GCC) for the SSG as developed in [14]. In this chapter a short overview is given of the technique proposed and tested in [14], and the possible improvements regarding the electrical braking circuit used during synchronisation is presented in simulation.

3.1. Challenges

Generally connecting a SG based WTG directly onto the grid poses problems under fluctuating wind conditions. As the wind speed fluctuates, the torque angle changes, directly affecting the output power of the generator. This causes oscillations and possibly instability. The inclusion of the PM slip rotor in the SSG acts as a low pass filter against sudden torque changes caused by fluctuating winds [14].

According to [14] the challenge with connecting the small scale SSG to the grid under variable wind speeds is due to the lack of pitch control to regulate the turbine torque and thereby the speed. It can be assumed that larger wind turbine systems would have the ability to control the torque applied to the main generator shaft by means of active pitch control.

3.2. Grid connection circuit for a small scale SSG

The GCC connects the generator to the grid without the benefit of turbine torque control. The wind provides the necessary torque for the turbine to accelerate. The speed and/or rate of acceleration are controlled by an electrical braking system. Once synchronisation conditions are met, the SSG is connected directly to the grid. If wind speeds exceed the maximum rated speed (12 m/s for the prototype 15 kW SSG) the system is set to engage standby mode until wind speeds recover to safe operating region. The synchronizing circuit developed in [14] is shown in Figure 3.2 below.

Figure 3.1: Photo of the GCC.

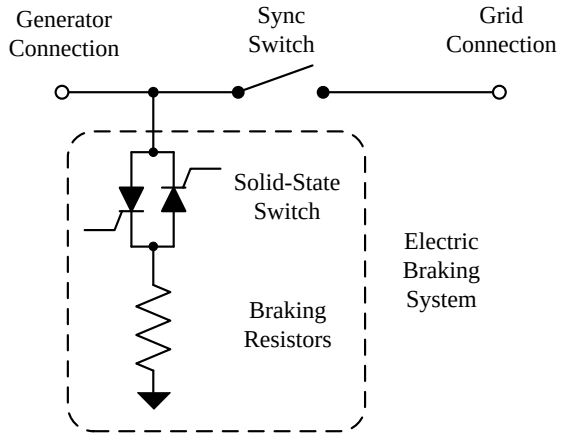

Figure 3.2: Synchronizing Circuit utilizing a thyristor based electric brake circuit [14].

3.3. Determining voltage and frequency

Under normal grid conditions there are three conditions that must be met before the generator may be connected to the grid. The rms voltage magnitude of the generator and grid must be the same and the voltages in the *abc* reference frame must also be in phase. The generator voltage frequency must be slightly higher than the grid-voltage's frequency [18].

The rms voltage, voltage phase angle, and voltage frequency is determined by first calculating the $\alpha\beta$ voltage magnitudes for the grid and generator, using the Clarke Transform as shown in (3.1).

$$\begin{bmatrix} v_\alpha \\ v_\beta \end{bmatrix} = \frac{2}{3}\begin{bmatrix} 1 & 0.5 & -0.5 \\ 0 & \frac{\sqrt{3}}{2} & -\frac{\sqrt{3}}{2} \end{bmatrix}\begin{bmatrix} v_a \\ v_b \\ v_c \end{bmatrix} \tag{3.1}$$

The vector magnitude and angle, as defined in Figure 3.3, is determined using (3.2). The frequency is determined by differentiating the phase angle as in (3.3).

$$\begin{aligned} |v_{\alpha\beta}| &= \sqrt{{v_\alpha}^2 + {v_\beta}^2} \\ \phi_{\alpha\beta} &= \tan^{-1}\frac{v_\beta}{v_\alpha} \end{aligned} \tag{3.2}$$

$$f_{\alpha\beta} = \frac{d\phi_{\alpha\beta}}{dt} \tag{3.3}$$

The phase difference between the generator and grid voltage vectors is illustrated in Figure 3.4. If the two vectors have the same amplitude, zero phase difference, $\Delta\phi = 0°$, and rotates at the same angular frequency, i.e. $\Delta f = 0$ Hz, the generator sync switch in Figure 3.2 may be closed.

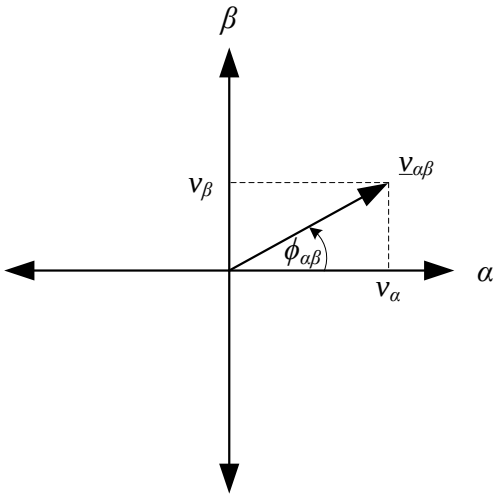

Figure 3.3: Compiling voltage vector from v_α and v_β.

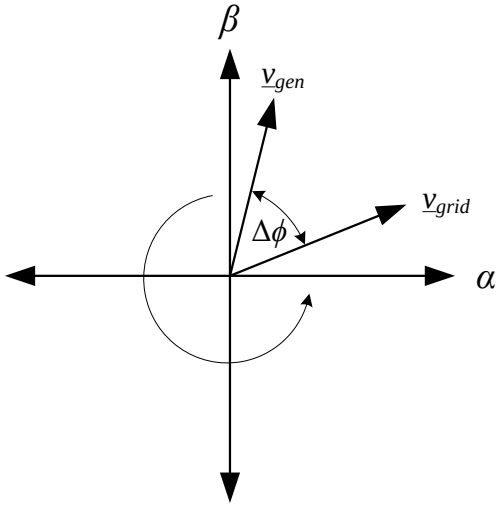

Figure 3.4: Rotating $\alpha\beta$ voltage vectors.

3.4. Speed control mechanism

The electric brake circuit designed in [14] consists of a three phase back-to-back thyristor module connected between a dumping load and the generator as shown in Figure 3.2. The fire angle delay of the thyristors is controlled with the control loop as shown in Figure 3.5. The model parameters as given in Table 3.1 and determined in [14] are used in the following simulations.

Table 3.1: Model parameters used in thyristor based speed control simulation

$K_i =$ 20	$R =$ 6 Ω	$L_s =$ 477 µH
$K_p =$ 15	$R_s =$ 0.15 Ω	$V_{source} =$ 325 V

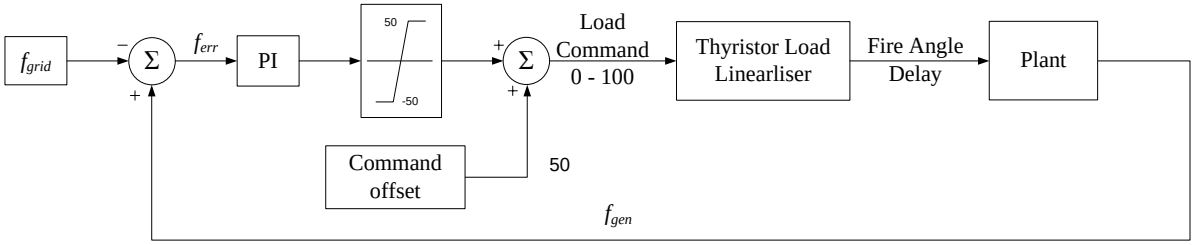

Figure 3.5: Speed control loop [14].

3.4.1. Speed control simulations using a thyristor based braking circuit

A model for the braking circuit is created using the VHDL-AMS modelling language. The circuit as shown in Figure 3.6 is simulated using the Mentor Graphics SystemVision (MGSV) program at maximum rated wind speed (11 $m.s^{-1}$). Using a lookup table the torque-speed relationship for the current wind turbine was approximated as shown in Figure 3.7. The simulation result for the turbine speed is shown in Figure 3.8. The maximum overshoot during the simulation is 0.1 p.u. and the electric brake circuit takes about 5 seconds before the generator frequency is within the band required for synchronisation. After 11.85 seconds the conditions as described in 3.3 are met and the synchronisation switch is closed. The generator is now connected to the grid. An extract of the voltage and current waveforms are shown in Figure 3.10 and Figure 3.11 respectively. Note the distortion on the voltage waveform. Due to the distortion the thyristor controller has difficulty triggering the thyristors at the right time.

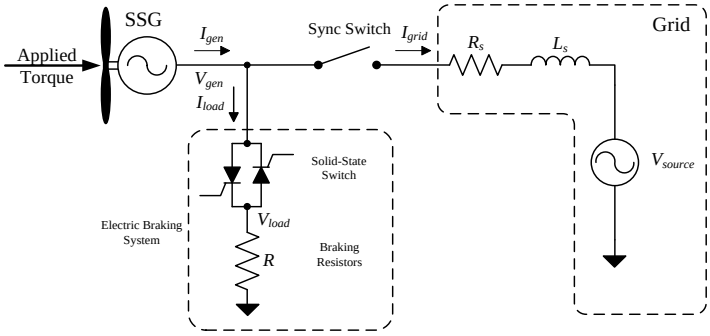

Figure 3.6: Circuit used to simulate the effectiveness of thyristor based speed control on the SSG.

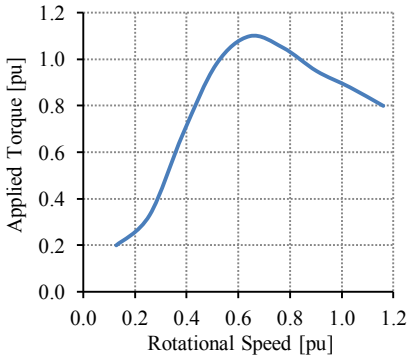

Figure 3.7: Applied torque vs. speed at maximum rated wind speed.

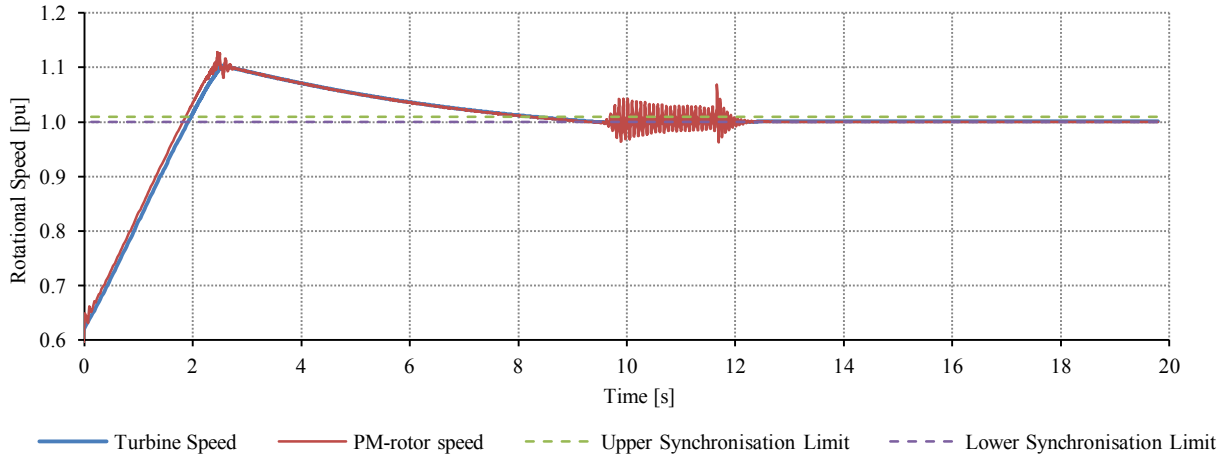

Figure 3.8: Simulated rotational speed for thyristor based speed control at maximum rated wind speed.

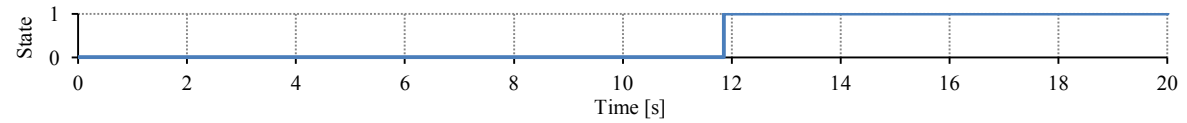

Figure 3.9: Simulated state of the synchronisation switch.

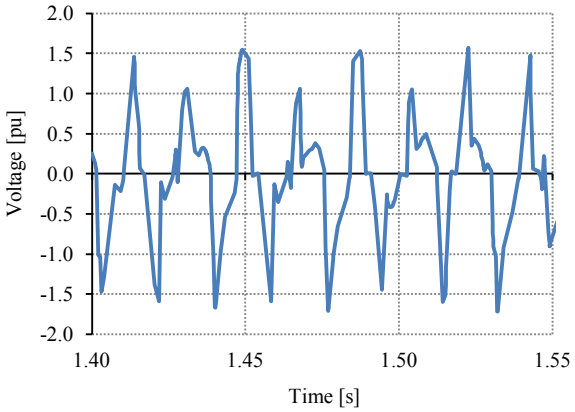

Figure 3.10: Extract of the per phase voltage during thyristor based speed control simulation at maximum rated wind speed.

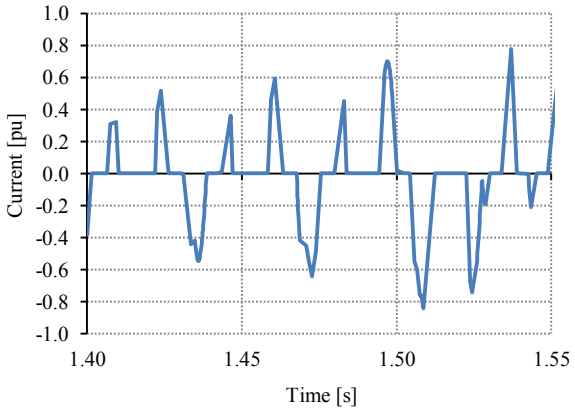

Figure 3.11: Extract of the line current during thyristor based speed control simulation at maximum rated wind speed.

3.4.2. Practical results

Practical results conducted by [19] showed that the thyristor based brake circuit works very well, but due to the high harmonic distortion (THD) the SSG generates excessive audible noise. The author of [19] recommended that the use of an uncontrolled diode rectifier driving a DC dumping load that is controlled by a chopper circuit be investigated as a possible replacement for the thyristors braking circuit.

3.5. IGBT-based speed control

A proposed method to decrease the THD is to use a rectifier-IGBT based braking circuit shown in Figure 3.12 to replace the thyristor braking circuit used in [14]. The development of the IGBT-braking circuit is discussed in section 4.5. The control logic is kept as designed in [14]. The linearization function, shown in the speed control loop in Figure 3.5, is removed since the power

absorbed by the IGBT-rectifier circuit is linearly dependant on the duty cycle. This was not the case with the thyristor circuit. The IGBT operates at a switching frequency of 10 kHz and switches a dc load. Using the multi-run function of the MGSV package the optimal dc load value is determined to be 7 Ω.

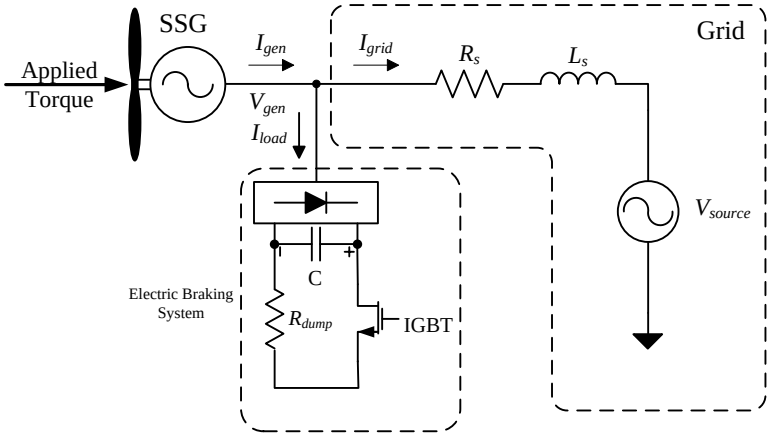

Figure 3.12: SSG with IGBT-based electrical braking circuit

3.5.1. Speed control simulations using an IGBT-rectifier based braking circuit

After substituting the thyristor brake with the IGBT-based brake as shown in Figure 3.12 the simulation as described in the previous section is repeated. The results are shown in Figure 3.13 to Figure 3.16. It is immediately apparent that the IGBT-brake circuit shows better characteristics regarding waveform shape. The overshoot and settling time may be improved if the PI controller constants are tuned for this circuit. Currently the same values are used as determined in [14] for the thyristor circuit.

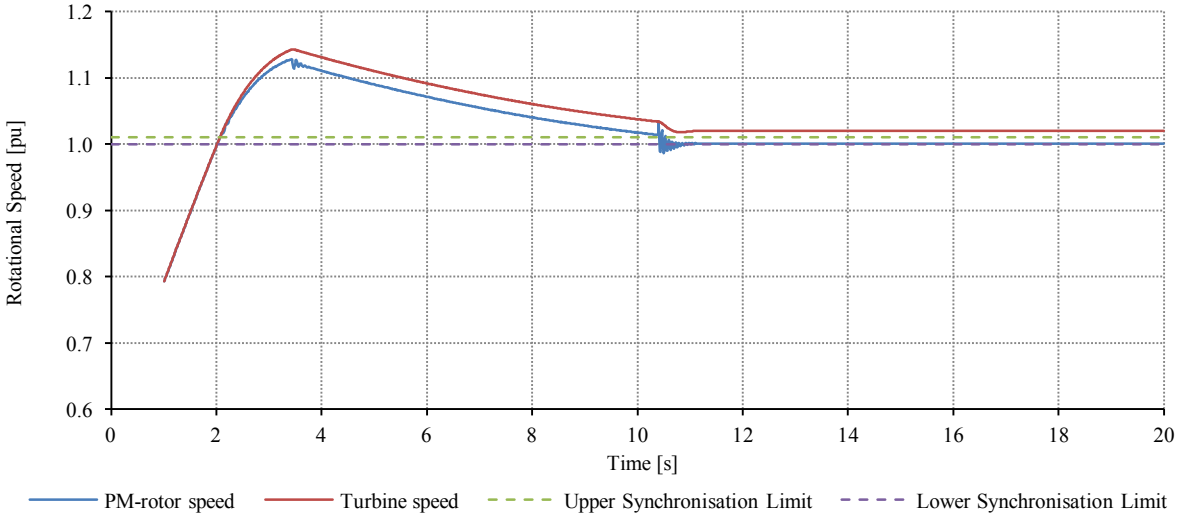

Figure 3.13: Simulated rotational speed for IGBT-rectifier based speed control at maximum rated wind speed.

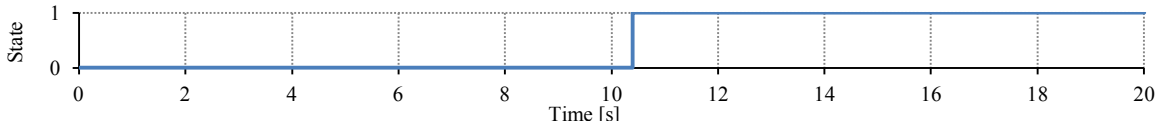

Figure 3.14: Simulated state of the synchronisation switch.

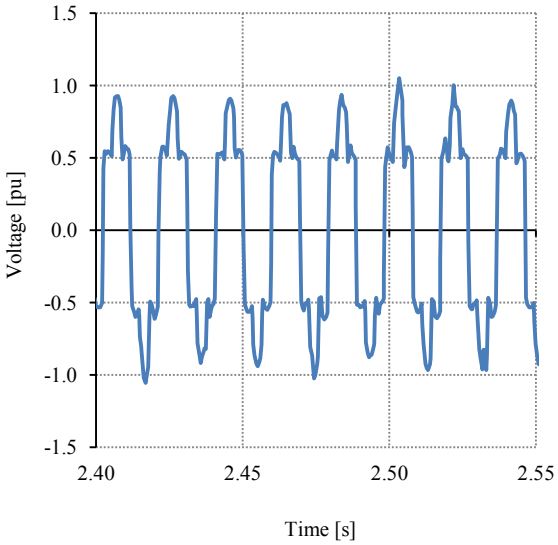

Figure 3.15: Extract of the per phase voltage during thyristor based speed control simulation at maximum rated wind speed.

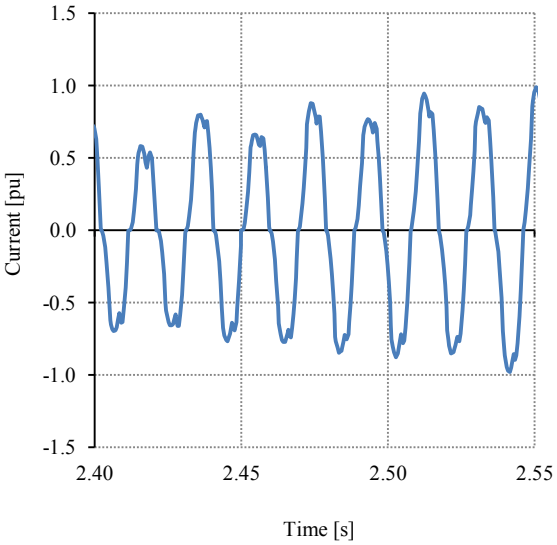

Figure 3.16: Extract of the line current during thyristor based speed control simulation at maximum rated wind speed

3.6. Conclusion regarding the grid connection unit

The simulation results show that the IGBT-rectifier circuit has better current characteristics. The IGBT-rectifier circuit must be tested in practice before it can seriously be considered as a replacement for the thyristor braking circuit.

Chapter 4. Active power curtailment

As specified by NERSA a WEF must have the capability to control the active power output during both normal operation and during frequency disturbances. On larger generators (>100 kW) one could expect the use of pitch control to decrease the torque provided by the wind turbine and thus decrease the output power. Generators equipped with solid-state power converters can limit the active power output by switching a load on the DC bus. The 15 kW SSG wind turbine considered in this thesis is not equipped with pitch control or a power converter and an alternative method for controlling the active power output is simulated in this chapter.

4.1. Requirements for active power curtailment

The grid code specifies that the WEF have the ability to ramp down the active power output at a minimum rate of 1% of the WEF's rated power capacity per second. This ability is required normally called upon during frequency disturbances where the WEF must curtail the active power output if the grid frequency is increasing. The settings and various power set-points are different for each WEF and is specified by the system operator [20].

4.2. Traditional braking mechanisms

There are various braking mechanisms that can be used to curtail the active power. These can be categorised as aerodynamic, mechanical or electromagnetic. A basic mechanical layout for a wind turbine nacelle is shown in Figure 4.1.

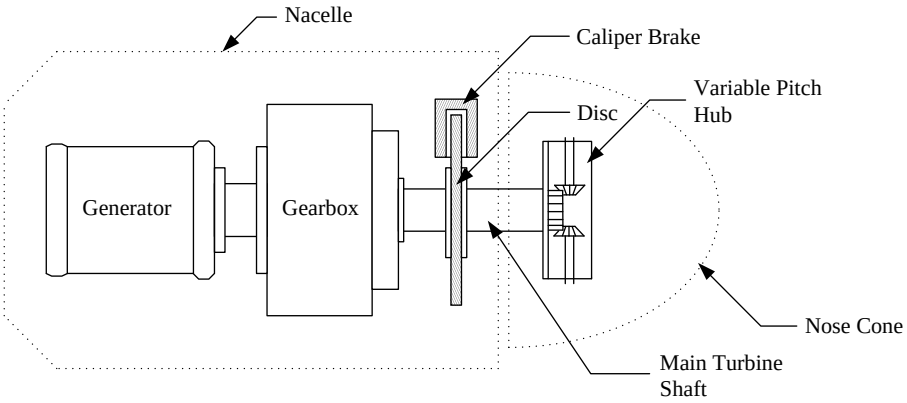

Figure 4.1: Basic layout of a large wind turbine showing the mechanical brake and the pitch control hub. The electromagnetic braking devices are not shown in this figure.

4.2.1. Aerodynamic braking

Two popular aerodynamic methods for limiting the turbine torque on variable speed WEF's are passive stall control, where the rotor blades are designed to stall at high wind speeds, and pitch angle control, where the aerodynamic efficiency of the rotor blades are changed by adjusting the wind angle of attack as shown in Figure 4.2 [21].

Figure 4.3 shows the workings of a pitch control concept for small wind generators. The angle of attack, in Figure 4.2, is varied by moving the shaft as indicated in Figure 4.3.

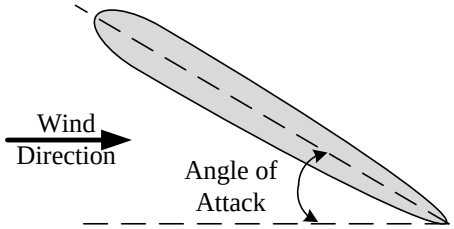

Figure 4.2: Angle of attack for an air foil.

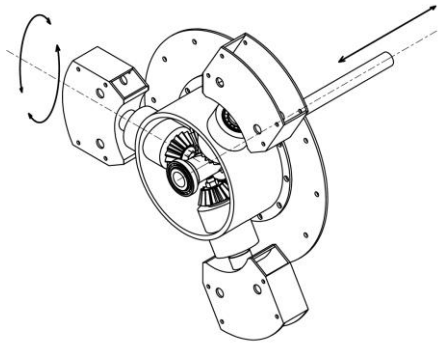

Figure 4.3: Pitch controller concept for a small wind turbine [22].

4.2.2. Mechanical braking

Wind turbines are often equipped with a mechanical disc or drum brake. The purpose of this brake is not to limit the output power, but rather to act as a failsafe brake during maintenance. If a mechanical braking system was used for constant power curtailment, the maintenance cost associated with brake wear would be too high.

4.2.3. Electromagnetic braking using a solid state power converter

The solid-state power converter setup as shown in Figure 4.4 is the standard setup for various generator types. By implementing the correct control loop functions, the power converter can limit the rotational speed and the active power output of the generator. Furthermore the active power delivered to the grid can be limited by controlling the DC bus voltage by dumping the excess energy on the resistors as shown in Figure 4.4 [21].

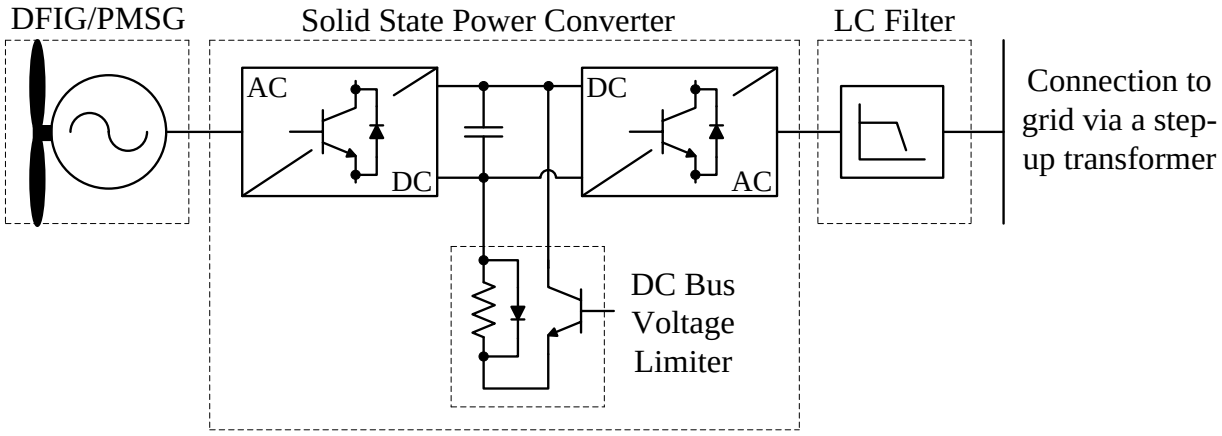

Figure 4.4: Solid-state power converter connected to the generator and the grid [21].

4.3. System currently used on the small SSG based wind turbine

Although it is conceivable that a larger (> 50kW) SSG based wind turbine would have a pitch controller the current small (15kW) SSG based wind turbine does not have the benefit of either a pitch controller or a solid-state power converter. That means that there is currently no method of controlling the output power of the generator.

Speed control during grid synchronisation

In[14] an electric brake circuit, as shown in Figure 4.5, was developed to control the rotational speed of the generator for synchronisation. While the SSG is unconnected to the grid, the generator

electrical frequency is controlled by controlling the load torque using a controllable load. Currently a thyristor based electrical brake circuit is used to control the generator speed during the grid synchronisation process. This same circuit can also be utilized to limit the active power output of the WEF since each SSG must be equipped with a braking circuit in order to synchronise the generator with the network. By increasing the fire angle of the thyristors, the power absorbed by the load can be controlled.

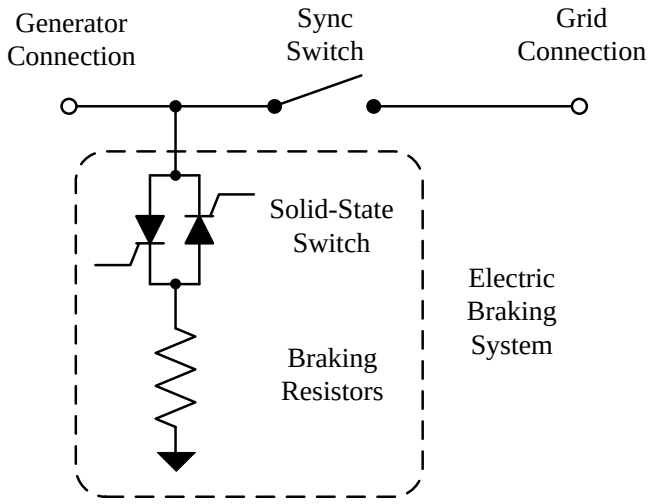

Figure 4.5: Thyristor based brake circuit used for speed control during grid synchronisation.

4.4. Thyristor based power curtailment

In this section the use of the thyristor braking circuit, as designed in [14], for active power curtailment purposes is discussed. Each SSG will need to be equipped with an electrical braking circuit.

4.4.1. Principle

Using a three phase back-to-back thyristor module connected between a dumping load and the generator as shown in Figure 4.5, the active power delivered to the grid can be limited. By changing the fire angle, α, as shown in Figure 4.6 and Figure 4.7 the voltage applied to the dumping resistors can be controlled. The voltage can be calculated using equations (4.1) to (4.4), where V_m is the maximum amplitude of the voltage waveform. The rms voltage calculated in equation (4.4) equals the voltage applied to the load resistor, V_{load}. The per phase active power absorbed in the load is given by equation (4.5) where V_{load} is the per phase RMS voltage applied to the load.

$$V_{rms} = \sqrt{\frac{1}{T}\int_0^T f(\theta)^2\, d\theta} \tag{4.1}$$

$$f(\theta) = V_m \sin\theta \tag{4.2}$$

$$V_{rms} = \sqrt{\frac{{V_m}^2}{\pi}\left(\int_0^{\alpha} \sin\theta^2\, d\theta\right) + \left(\int_{\alpha}^{\pi} \sin\theta^2\, d\theta\right)} \tag{4.3}$$

$$= \sqrt{\frac{{V_m}^2}{2\pi}\left[(\pi - \alpha) + \frac{\sin(2\alpha)}{2}\right]} \tag{4.4}$$

$$P_{dump} = \frac{V_{load}^2}{R_{load}} \tag{4.5}$$

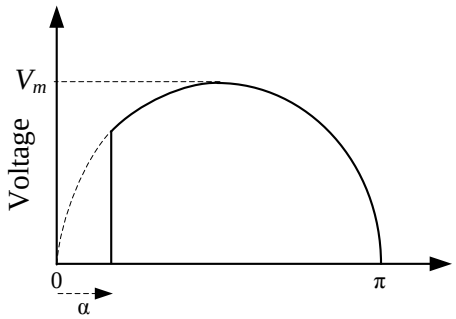

Figure 4.6: Thyristor fire angle.

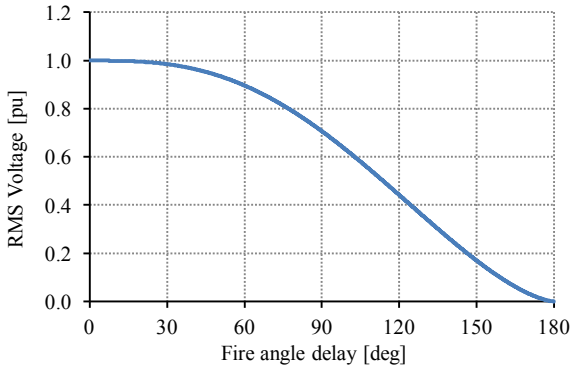

Figure 4.7: Load voltage due to fire angle delay control.

4.4.2. Single phase simulation to determine the load current waveform

The single phase circuit shown in Figure 4.8 is simulated in MGSV. The purpose of the simulation is to determine the load current waveform shape when using a thyristor based electric braking circuit. This waveform is later compared to the load waveform of the IGBT-based electric braking circuit.

The circuit shown in Figure 4.8 is based on the thyristor braking circuit developed in [14] and consists of a 230 V ideal voltage source operating at 50 Hz, a 7 Ω resistor and an ideal thyristor module. The thyristor module receives a firing angle as an input. The circuit setup is shown in Figure 4.8. The rated maximum power that the circuit can dump is given in equation (4.6). The fire angle delay is varied during the simulation and the active power absorbed in the load is calculated and given in Figure 4.9. The simulated voltage and current waveforms are shown in Figure 4.10 and Figure 4.11 for fire angles as indicated in the figures. The harmonic content for Figure 4.10 and Figure 4.11 is shown in Figure 4.12. As seen in Figure 4.12 there is significant 2nd, 3rd and 5th harmonics present in the current waveform.

The electric braking circuit can dump more than the rated power of the 15 kW SSG. This would seem unnecessary, but the circuit was initially designed to operate only when the generator is unconnected to the grid. When a load is applied to the SSG while it is not connected to the grid, the terminal voltage will drop and causes the full rated dumping ability of the braking circuit to be far lower than determined in equation (4.6).

$$P_{dump,3\phi} = \frac{3V_{load}^2}{R_{load}} = \frac{3(230)^2}{7} = 22.67 \text{ [kW]} \tag{4.6}$$

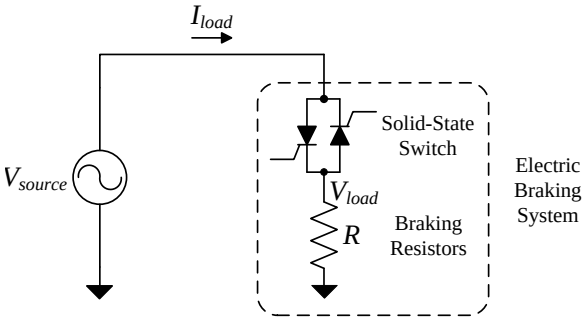

Figure 4.8: Single phase thyristor based electric brake simulation setup.

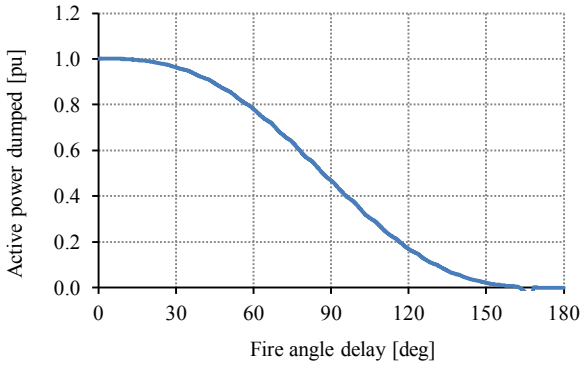

Figure 4.9: Active power dumped in resistors during fire angle delay control simulation.

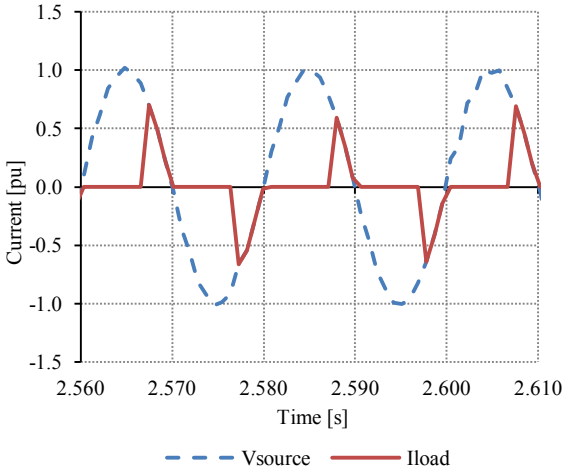

Figure 4.10: Simulated load current waveform during large fire angle delay values.

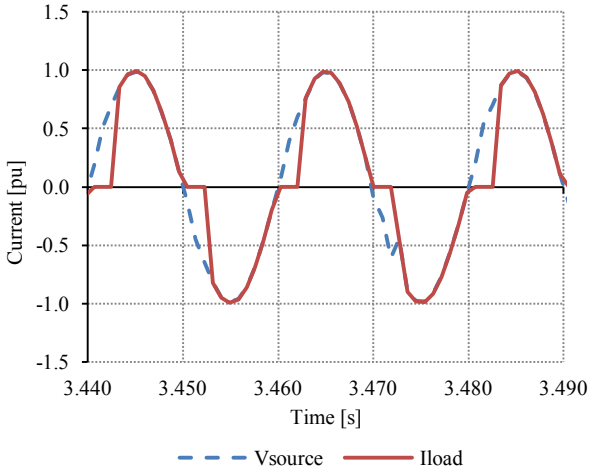

Figure 4.11: Simulated load current waveform during little fire angle delay values.

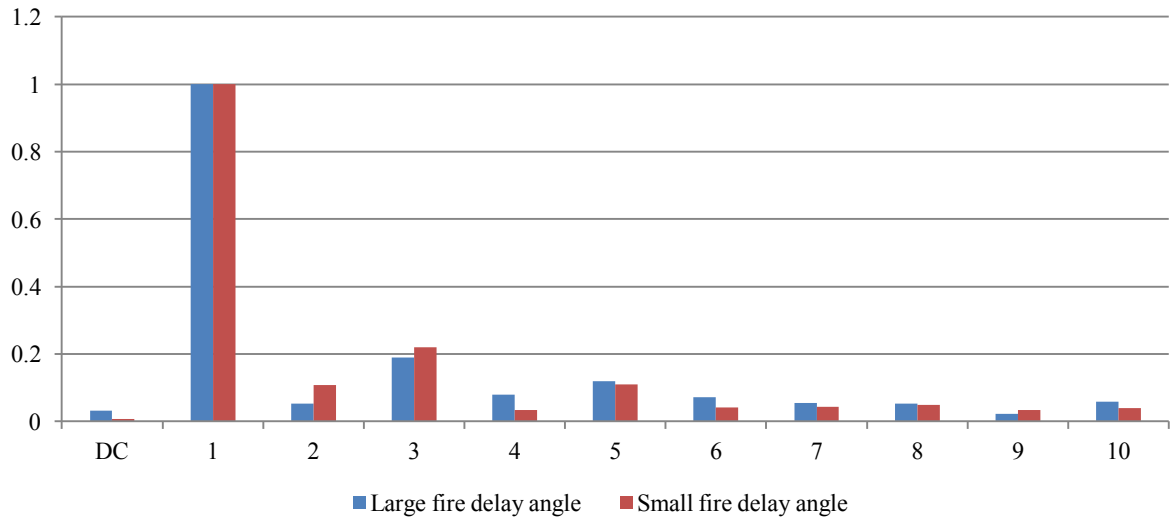

Figure 4.12: Harmonic content for the thyristor controlled current waveform.

4.4.3. Simulation with the generator connected to the grid

In the next simulation the generator is connected to the grid while rated torque is applied. The electric brake circuit is inserted in parallel with the generator and the grid as shown in Figure 4.13. The grid

model consists of an ideal 400 V_{LL} voltage source operating at 50 Hz. The source impedance $(R_s + jwL_s)$ is 0.15 + j0.15 Ω. The fire angle is decreased until the electric brake circuit draws maximum power.

Some simulation results are shown in Figure 4.14 to Figure 4.16 where the rated power is 15 kW. When the fire angle delay is 0˚ degrees, 22 kW is dumped on the resistor bank. Since the generator can only deliver 15 kW at rated torque, the difference (7 kW) is drawn from the grid. As the fire angle increases, less power is drawn from the grid. When the fire angle is at 70 degrees the load dumps 15 kW of power and no power is delivered or absorbed from the grid. Thereafter increasing amounts of active power is delivered to the grid, until the fire angle reaches 180 degrees and the thyristors turn off. The per phase grid current is shown in Figure 4.15 and Figure 4.16. In Figure 4.16 no actual active power is transmitted to the grid.

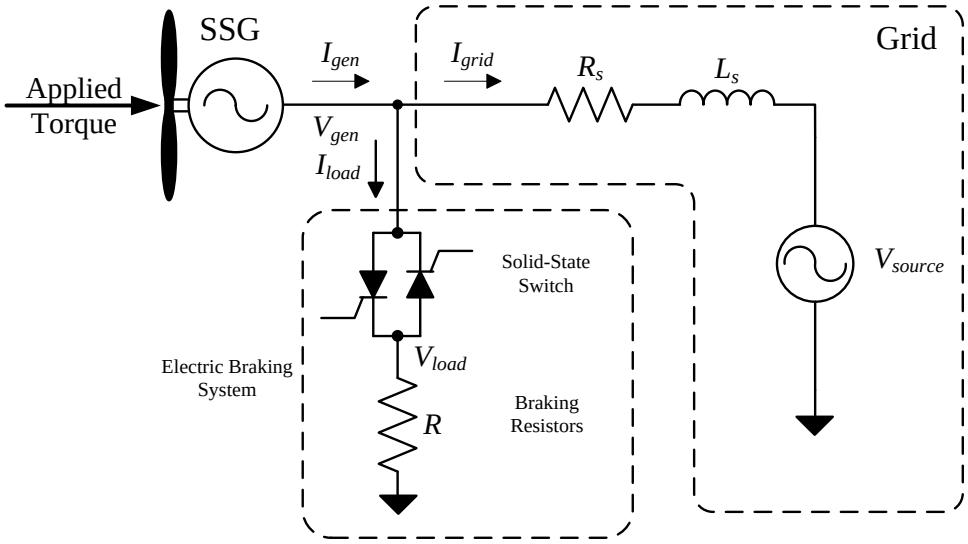

Figure 4.13: Per phase circuit of the grid connected SSG with thyristor based electric brake circuit.

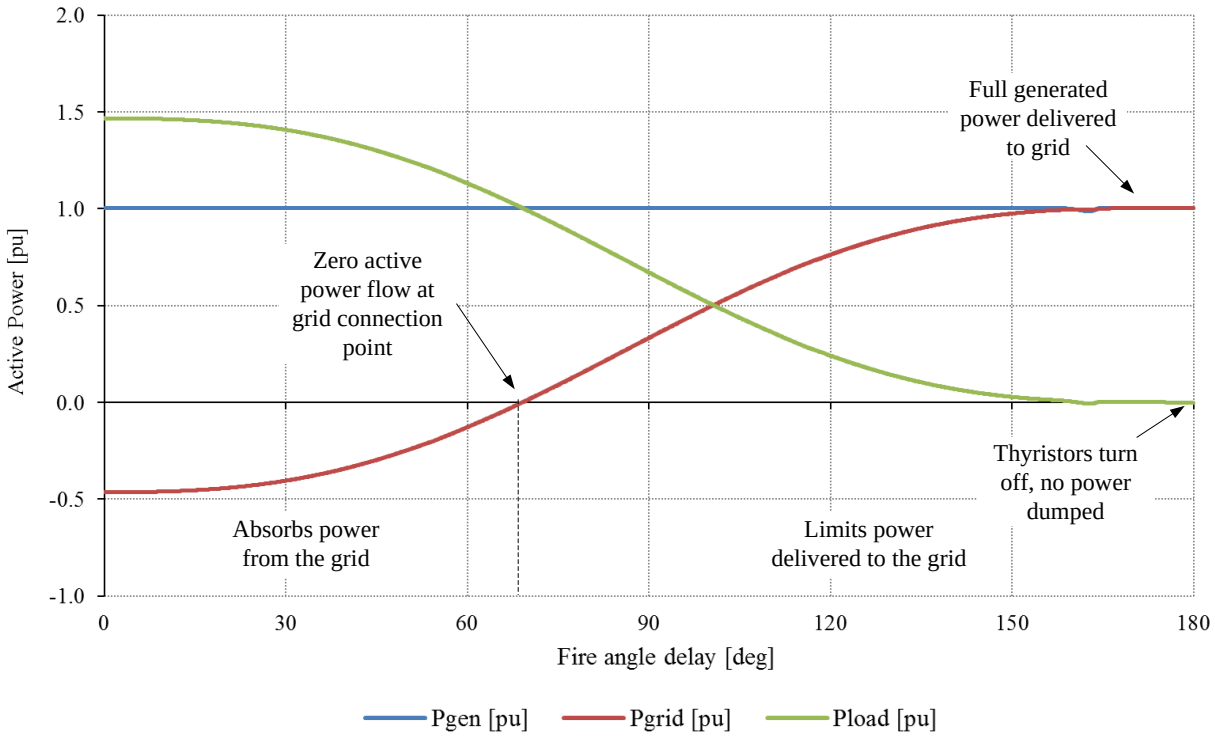

Figure 4.14: Simulation active power delivered to the grid at various fire delay angles.

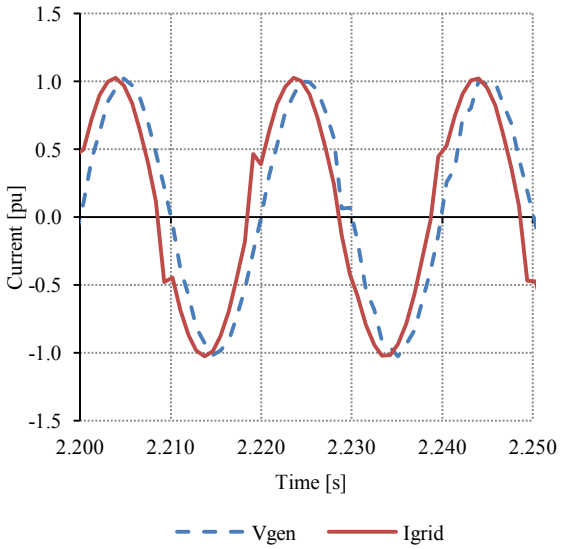

Figure 4.15: Grid current waveform for little amount of power dumped in the load.

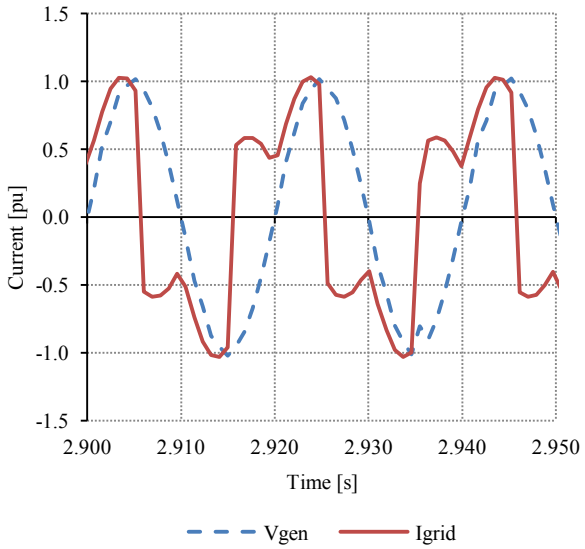

Figure 4.16: Grid current when all of the active power is dumped in the load.

4.5. IGBT-rectifier based power curtailment

4.5.1. Principle

An alternative method of active power curtailment is proposed using an IGBT switching a load on a rectified circuit. This circuit, shown in Figure 4.17, is similar to the dc bus voltage limiter shown in Figure 4.4. The active power dumped in the load is directly proportional to the duty cycle, *D*, of the IGBT switch. The theoretical power absorbed by the electric brake is calculated using (4.7) to (4.9),

$$V_{dc} = \frac{3\sqrt{3}V_{peak}}{\pi} \tag{4.7}$$

$$I_{dc} = \frac{V_{dc}D}{R_{load}} \tag{4.8}$$

$$P_{load} = \frac{{V_{dc}}^2 D}{R_{load}} \tag{4.9}$$

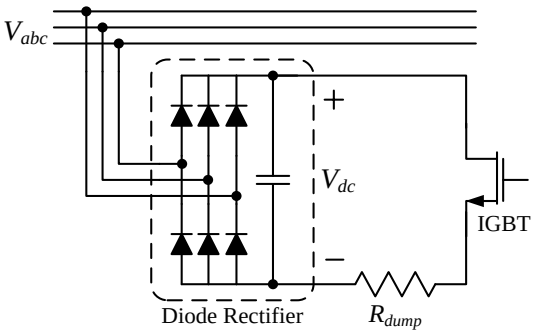

Figure 4.17: IGBT-rectifier based electric braking circuit.

4.5.2. Simulation to determine the load current waveform

The purpose of this simulation is to determine the load current waveform for an IGBT-rectifier based electric braking circuit. The waveform shape can then be compared to the load current waveform shape for a thyristor based electric braking circuit. The comparison will help to understand any differences with regard to the harmonic content when using the electric braking circuits to limit the active power output of a generator.

If this IGBT-rectifier circuit is implemented it would also be used to control the speed of the generator for synchronisation. The circuit shown in Figure 4.18 is simulated in MGSV. The three phase voltage source consists of an ideal 230 V RMS voltage source operating at 50 Hz. The source has a series impedance of 0.15 + j0.15 Ω. The IGBT is switched with a 10 kHz PWM signal. The resistor has a value of 7 Ω and a 10 µF capacitor was used to stabilize the dc bus. Using equations (5.9) to (5.11) and ignoring the voltage drop across the diodes, the maximum power absorbed in the dumping resistor is calculated to be 36 kW. During the simulation the duty cycle of the PWM signal was increased as shown in Figure 4.19. The corresponding simulation results are shown in Figure 4.20 to Figure 4.21. When comparing the current waveform shapes in Figure 4.21 and Figure 4.22 to those in Figure 4.15 and Figure 4.16, it becomes apparent that the IGBT-rectifier based dumping circuit generates more sinusoidal shaped waveforms. The harmonic content for the waveforms shown in Figure 4.21 and Figure 4.22 is shown in Figure 4.23. From Figure 4.23 it can be seen that there is significant 5th and a little 7th harmonic present in the current waveform. The harmonic content is very low when compared to the harmonic content in the thyristor controlled load current.

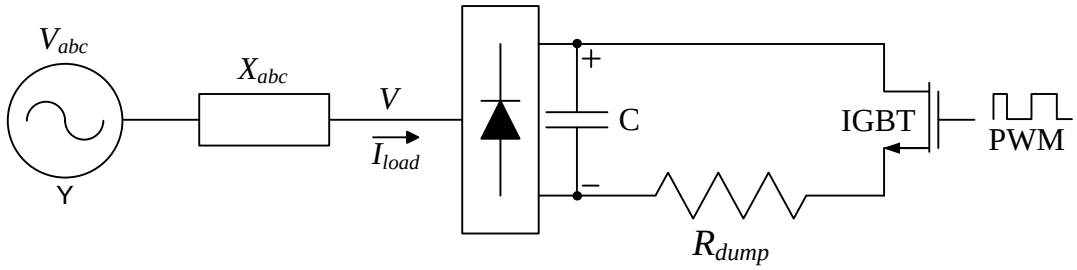

Figure 4.18: Simulation circuit for an IGBT brake connected to the grid.

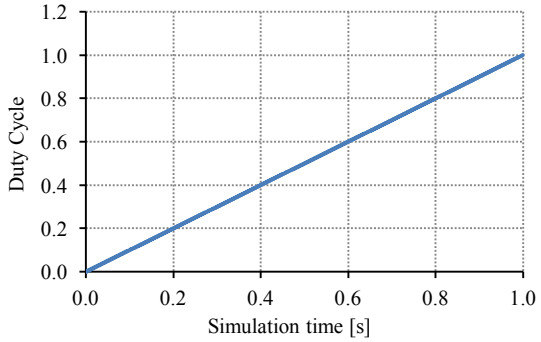

Figure 4.19: Input duty cycle increasing with simulation time.

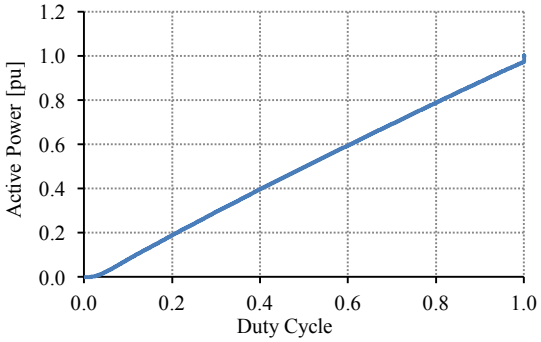

Figure 4.20: Simulated load braking power versus duty cycle.

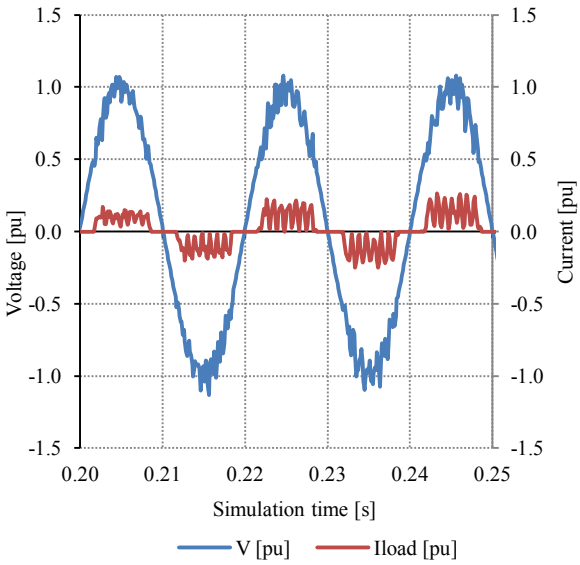

Figure 4.21: Extract of the per phase voltage and line current waveforms at low 20% duty cycle.

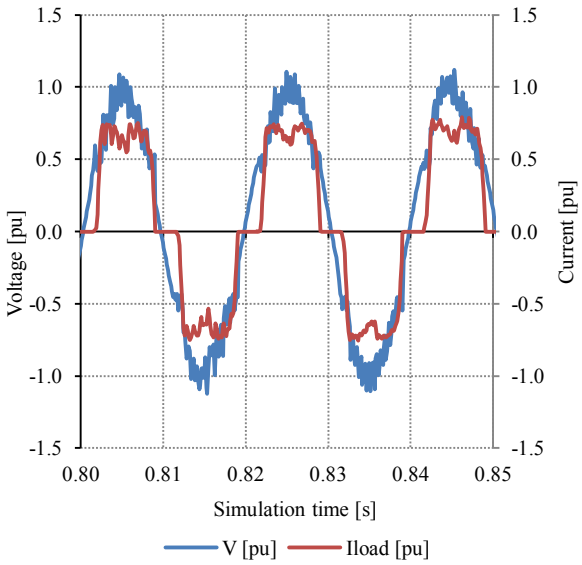

Figure 4.22: Extract of the per phase voltage and line current waveforms at 80% duty cycle.

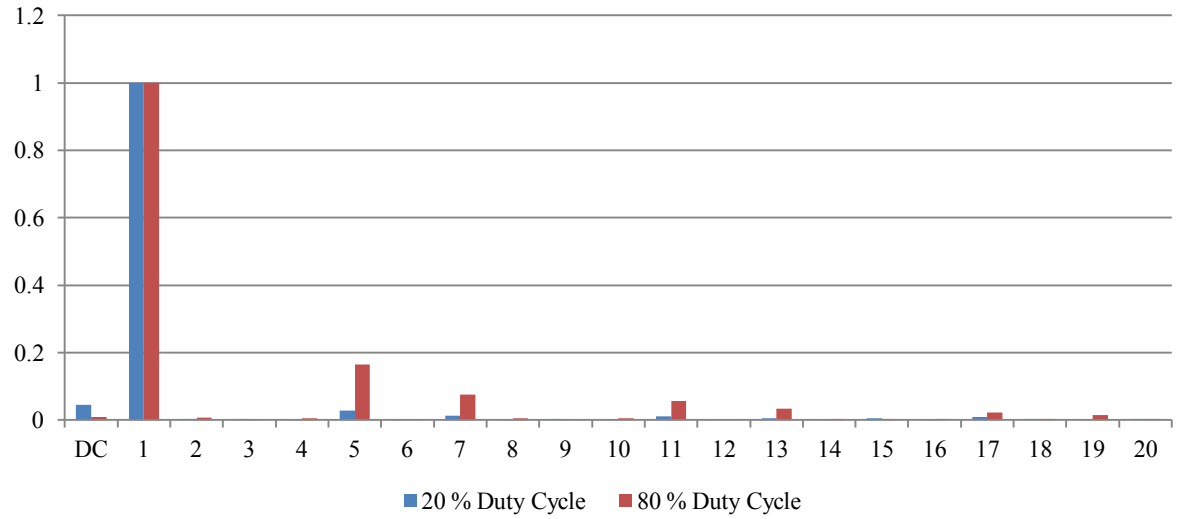

Figure 4.23: Harmonic content of the load current waveform for the IGBT braking circuit connected to the grid.

4.5.3. Simulation with the IGBT-brake and generator connected to the grid

In the next simulation rated torque is applied to the generator model while the generator is connected to the grid. The electric IGBT brake circuit is connected in parallel with the generator and the grid as shown in Figure 4.24. The grid model again consists of an ideal 230 V per phase voltage source operating at 50 Hz. The source impedance $(R_s + jwL_s)$ is 0.15 + j0.15 Ω. The duty cycle of the IGBT is increased until the electric brake circuit draws maximum power. The applied duty cycle is shown in Figure 4.25.

Since the electrical braking circuit can absorb up to 36 kW and the generator is rated to deliver 15 kW at rated torque, the electric braking circuit will start to absorb active power from the grid when the duty cycle exceeds 40%. Some simulation results are shown in Figure 4.26 to Figure 4.28. Figure 4.26 shows the active power output for various duty cycle values. Figure 4.27 and Figure 4.28 show

the grid voltage and current waveforms for 20% and 40% duty cycles respectively. At 20% duty cycle 50% of the rated generator power is dumped into the load. At 40% duty cycle all of the generator active power is dumped into the load. The current waveform shown in Figure 4.28 is purely inductive and no active power is flowing at the grid connection point. The harmonics content of the current shown in Figure 4.27 and Figure 4.28 is shown in Figure 4.29.

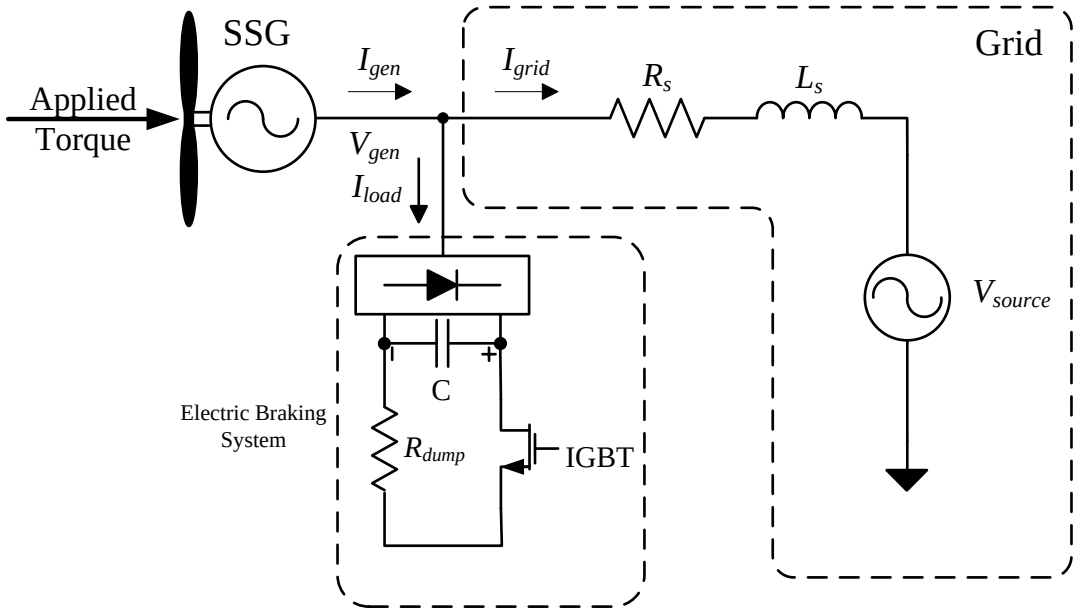

Figure 4.24: Single line diagram of a 3-phase SSG with IGBT-based electrical braking circuit.

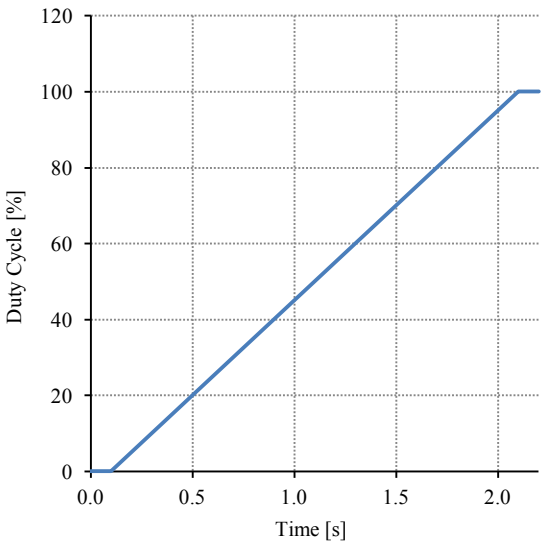

Figure 4.25: IGBT duty cycle increasing with simulation time.

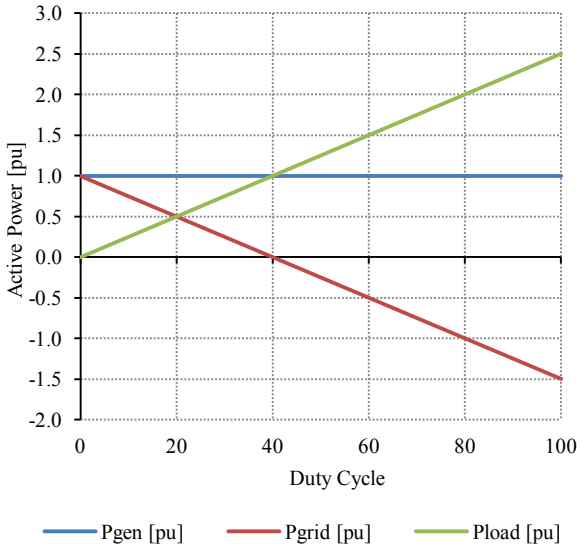

Figure 4.26: Simulated active power delivered to the grid at various duty cycle values.

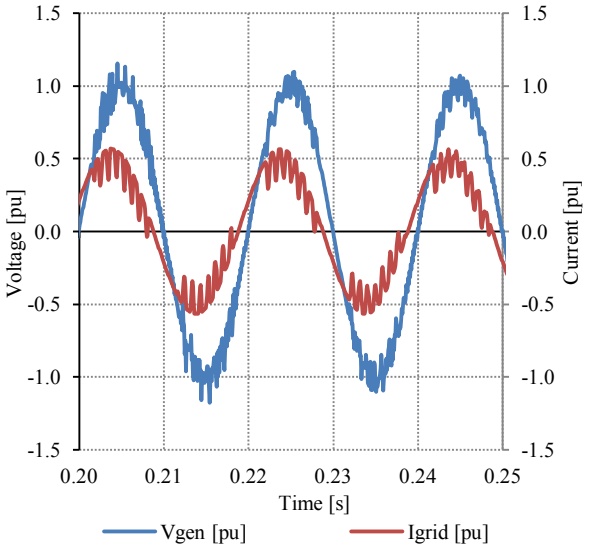

Figure 4.27: Per phase voltage and line current waveform at the grid connection point for 20% duty cycle.

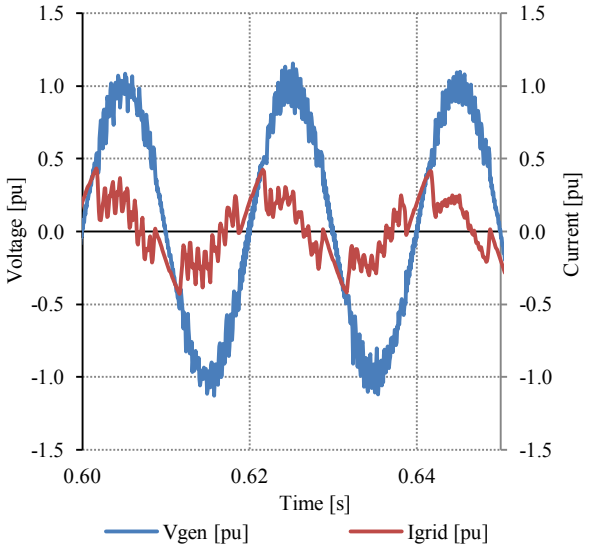

Figure 4.28: Per phase voltage and line current waveform at the grid connection point for zero active power flow.

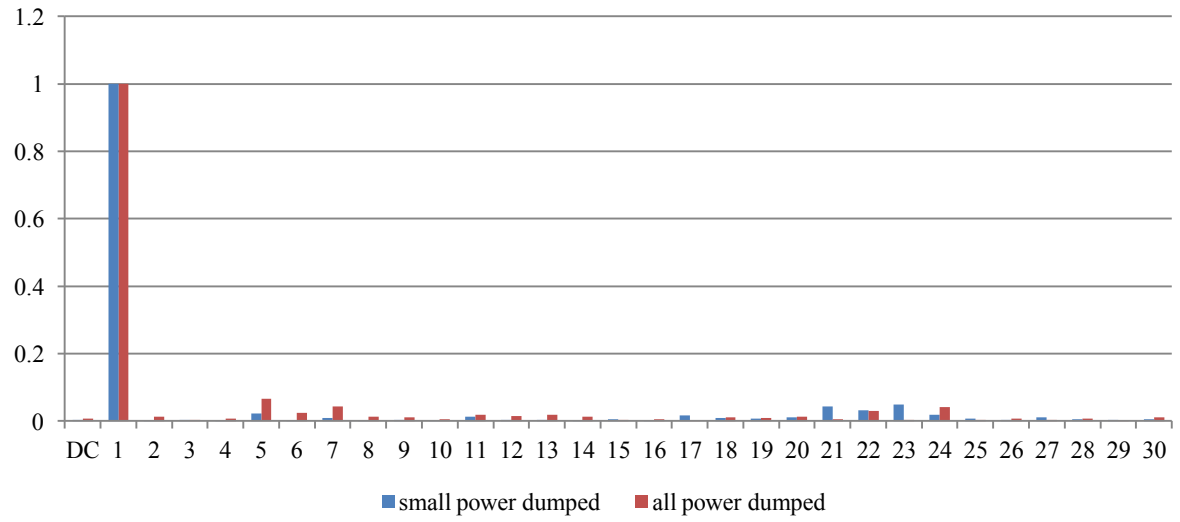

Figure 4.29: Harmonic content of the grid current waveform for active power curtailment using the IGBT-rectifier braking circuit

4.6. Conclusion with regards to active power curtailment

As discussed in 4.1 the WEF must have the capability to curtail the active power output at a minimum rate of 1% rated power per second. Both braking circuits, thyristor and IGBT, have a fast response time and should work very well even without active pitch control. However when comparing the harmonic content of the two methods, the IGBT-rectifier circuit appears to cause less distortion to the grid current waveform. From these simulation results it seems that the IGBT-rectifier circuit should be considered as a replacement for the thyristor based speed control device and serve as active power limiter during frequency disturbances.

Chapter 5. Frequency disturbance requirements

In the South African grid code NERSA specifies the minimum connection requirements for the WEF with regard to frequency disturbances. The WEF is required to stay connected to the grid for a predetermined amount of time, as well as curtail the active power output depending on the level of the disturbance. In this chapter a quick overview is given with regards to the effect of grid frequency disturbances on the SSG.

5.1. Grid code specifications

In the following section the grid code specifications regarding WEF connection and power curtailment during frequency disturbances is discussed.

5.1.1. Connection requirement

According to NERSA the WEF must be designed with the minimum capability of operating within the frequency range of 47 Hz to 52 Hz for a 50 Hz system, for the duration as shown in Figure 5.1. The WEF must also remain connected to the network during frequency changes of up to 0.5 Hz per second, provided that the frequency is still within the operating range as shown in Figure 5.1. Thereafter the individual wind turbines are allowed to disconnect as approved by the system operator [20].

5.1.2. Active power curtailment requirement

The WEF must incorporate a frequency response system. The frequency response system must curtail the active power output during a frequency disturbance, as shown in Figure 5.2. If the grid frequency rises above 50.15 Hz the WEF must act to ramp down the active power output at a minimum rate of 1% of the WEF's rated power capacity per second until the specified output power level is reached. Once the frequency rises to a level above point D, in Figure 5.2, the WEF may disconnect from the network. If the grid frequency is below the normal range, and is in the process of recovering, the WEF must also ramp down the active power as shown by line A-B in Figure 5.2. The points A, B, C, D and E depend on a combination of the frequency, active power and the curtailment set-point settings. These settings are different for each WEF and are specified by the system operator [20].

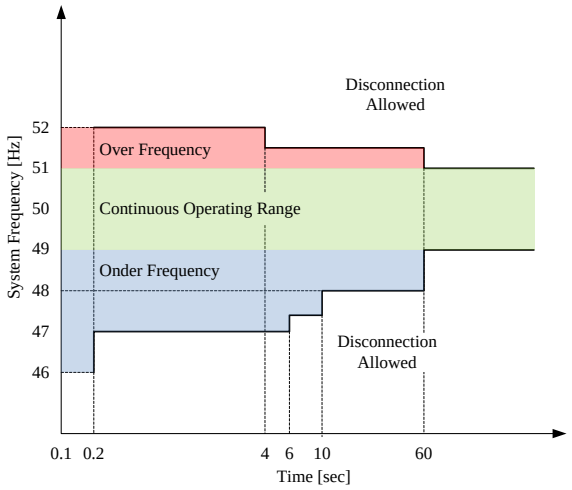

Figure 5.1: Minimum frequency operating range of a WEF connected to a 50 Hz system (during a system frequency disturbance) [20].

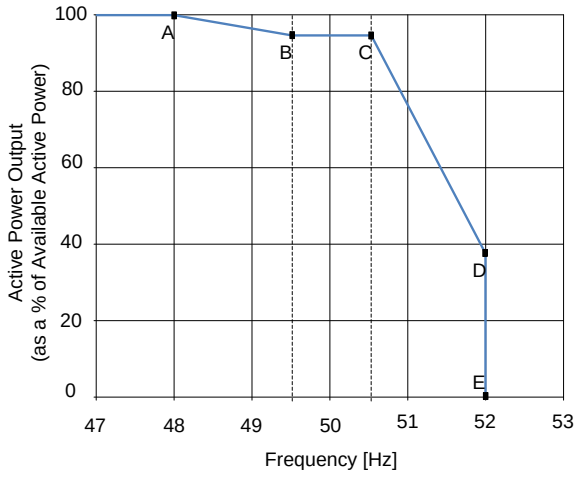

Figure 5.2: Power frequency control curve [20].

5.2. Influence of variations in voltage frequency on the SSG

The steady-state response of a synchronous generator with regards to electrical frequency is well documented. Under steady state conditions it can be shown that an increase in electrical frequency will cause an increase in turbine speed, leading to a decrease in torque and torque angle (assuming constant input power). The decrease in torque angle will lead to a decrease in the output power of the generator.

The question remains regarding the dynamic response of the SSG with regard to electrical frequency disturbances. The transient currents can be calculated by using the dynamic dq-equations that describes the SSG.

The d- and q-axis currents can be solved using the SG dq dynamic equations as given by (5.1) and (5.2). Using the inverse Park's transform, these current values are used to calculate the generator *abc* current. It should be noted that because the position reference in the Park transform is calculated by integrating the electric frequency, its rate of change will increase as the electrical frequency increases.

$$v_{qs} = -i_{qs}R_s - L_{qs}\frac{di_{qs}}{dt} - \omega_e L_{ds} i_{ds} + \omega_e \lambda_{me} \tag{5.1}$$

$$v_{ds} = -i_{ds}R_s - L_{ds}\frac{di_{ds}}{dt} - \omega_e L_{qs} i_{qs} \tag{5.2}$$

The torque applied by the SG-stator on the PM-rotor can be calculated using (5.3). Assuming that the q- and d-axis inductances are equal, which is the case with the SSG, then (5.3) can be simplified as given in (5.4).

$$T_s = \frac{3}{4}p\left[\left(L_{qs} - L_{ds}\right)i_{ds}i_{qs} + \lambda_{ms}i_{qs}\right] \tag{5.3}$$

$$= \frac{3}{4}p\lambda_{ms}i_{qs} \tag{5.4}$$

The torque generated by the IG and applied to the PM-rotor is described by (5.5).

$$T_m = \frac{3}{4}p\left[\left(L_{qr} - L_{dr}\right)i_{dr}i_{qr} + \lambda_{mr}i_{qr}\right] \tag{5.5}$$

The turbine speed can be calculated using (5.6) and (5.7).

$$T_t - T_m = J_t\frac{d\omega_t}{dt} \tag{5.6}$$

$$\omega_t = \frac{1}{J_t}\int (T_t - T_m)dt + \omega_{t0} \tag{5.7}$$

Table 5.1 summarises the expected transient response of the generator during changes in the grid frequency.

Table 5.1: Expected transient response of the generator due to frequency changes

Increasing electrical frequency:	Decrease in IG-slip Decrease in PM-rotor and SG-stator torque Decrease in output power
Decreasing electrical frequency:	Increase in IG-slip Increase in PM-rotor and SG-stator torque Increase in output power

5.3. Frequency disturbance simulations

Using MGSV the response of the SSG to worst case frequency disturbances is simulated. As shown in Figure 5.3 the grid frequency is changed at a rate of 0.5 Hz per second from 50 Hz to 52 Hz and back. Figure 5.4 through Figure 5.8 show the results of the frequency disturbance simulation. As shown in Figure 5.4 rated power is applied to the generator throughout this simulation. The grid frequency at time zero in the simulation is equal to the nominal 50 Hz grid frequency as shown in Figure 5.3. The grid voltage is kept at nominal value. The resulting output power, turbine speed and output current are shown in Figure 5.4, Figure 5.6, and Figure 5.8 respectively. It is also interesting to note the relatively large impact a frequency disturbance has on the transient slip, which directly impacts the current and power delivered during the disturbance.

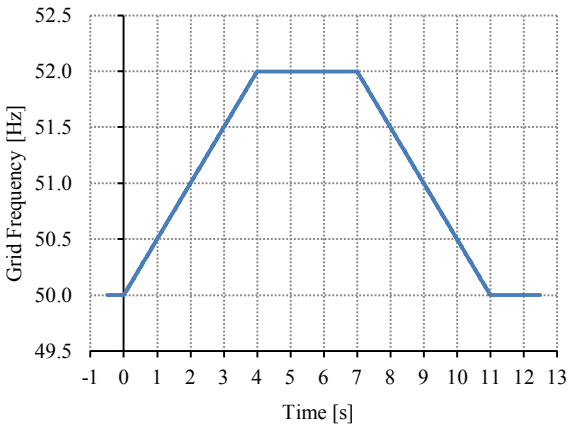

Figure 5.3: Electrical frequency changing at a maximum rate of 0.5 Hz/second.

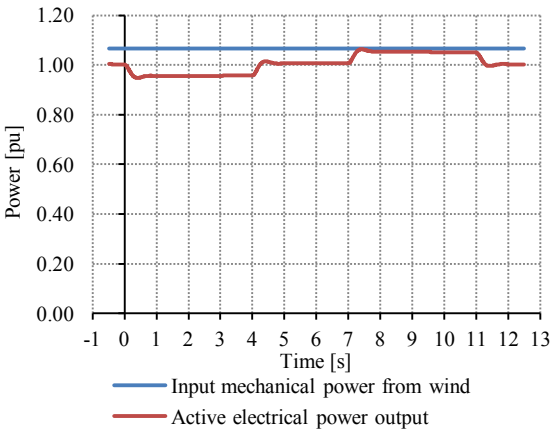

Figure 5.4: Simulated change in output power with changes is frequency.

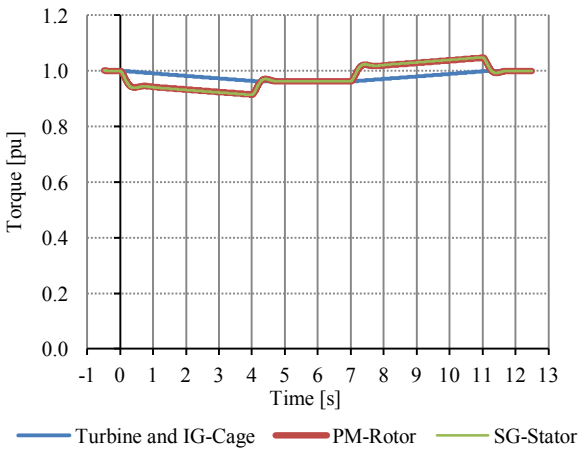

Figure 5.5: Simulated torque changes with frequency change.

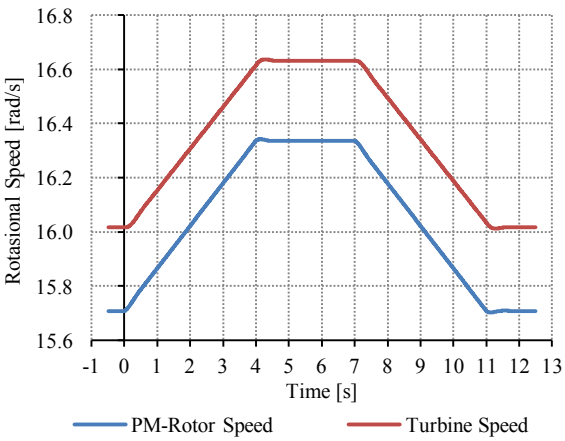

Figure 5.6: Simulated speed changes with frequency changes.

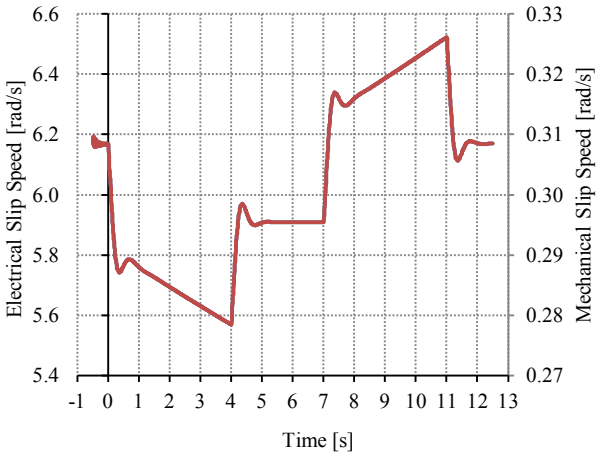

Figure 5.7: Simulated change in IG-rotor slip with frequency change.

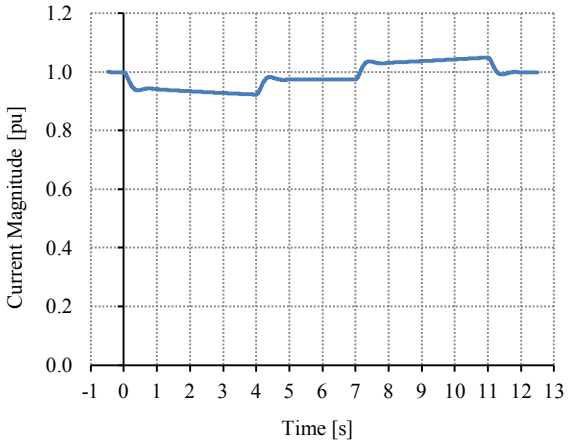

Figure 5.8: Simulated change in generator output current with frequency change.

5.4. Conclusion with regards to the frequency response of the SSG

Looking at the results of the worst case frequency disturbance simulation a few remarks can be made regarding the response of the SSG.

Depending on the rate of frequency change the output current amplitude could increase to 1.1 p.u. as shown in Figure 5.8. All components should be rated to handle at least 10% over current for duration of not less than 4 seconds. Faster changes in grid frequency will lead to higher over currents, but the generator is allowed to disconnect if the frequency changes faster than 0.5 Hz/sec.

The rotational speed of the turbine is slightly influenced by frequency changes. As shown in Figure 5.6 the turbine speed will change during a frequency disturbance. It is necessary that the turbine components be designed with the capability of operating at higher than rated speeds.

The simulations also show how the generator output decreases as the grid frequency increases, and increases as the grid frequency decreases. Although the natural response of the generator with regards to output power is comparable to the required system response, some form of active power curtailment is required to further limit the output power if needed.

From the simulation results it would seem that the SSG should not have any problems complying with the frequency disturbance requirements as specified in the grid code of South Africa.

Chapter 6. On load tap changer topologies

An on-load tap changer (OLTC) transformer is used to change the voltage on a line. OLTC transformers can be grouped into three different categories: mechanical (classic), electronically assisted (hybrid), or fully electronic (solid state). The different topologies have different advantages and disadvantages. The various tap changer topologies are compared in this chapter to determine which type will work best with the small scale SSG WTG concept.

6.1. Mechanical tap changers

There are two types of mechanical tap changers. The first is the basic type and is normally used for off-load tap changes, on distribution level transformers. This type of tap changer has only so called selector switches. The second type is a bit more complex; instead of having only selector switches, secondary switches are placed in series to the selector switch circuit. These secondary switches are known as the diverter switches or the diverter circuit. Most other OLTC topologies are derived from these two types of tap transformers.

6.1.1. Basic tap changer

The voltage on distribution level (400V) is controlled by changing the tap ratio of the transformer. These taps are normally changed off-load. Figure 6.1 shows the circuit diagram for the most basic of tap changing transformers. As can be seen each tap has a selector switch. As the taps are changed the number of windings that are conducting current is changed. Thus creating a variable turns transformer. In most applications these switches are rotating mechanical switches and need to be changed manually while the transformer is isolated from the network [23][24] [25]. When mechanical switches are used, it is preferred that the switchgear is placed on the high voltage winding, to decrease the current handling capacity of the switch.

There are certain cases where the above configuration is used for on-load mechanical switching. However these transformers suffer from arcing between contacts; which leads to an increased rate of transformer oil pollution and thus maintenance [23] [25]. In some cases, when the transformer taps are changed on-load, vacuum switches[1] are used to interrupt the load current [23].

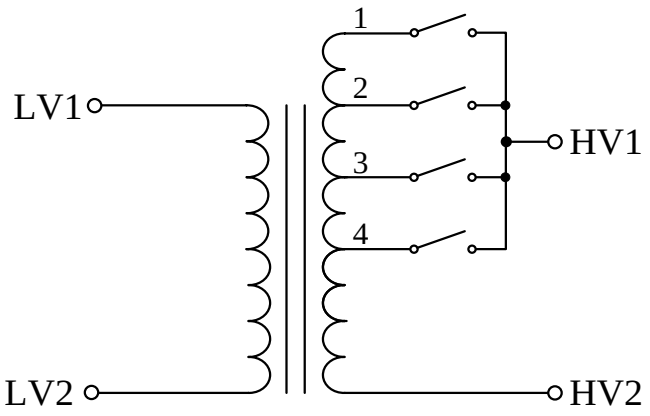

Figure 6.1: Basic tap changing transformer.

[1] The use of vacuum switches decrease the arcing and contact wear that occur during switch operation

Switch specifications
It should also be noted that all of the switches used in this type of configuration need to be rated at the rated voltage and load current of the transformer. The rating of the switches should also take into account the larger inrush current value[2] and at least one switch should be able to handle fault currents.

Disadvantage
The following disadvantage was identified in [23]:

- Maintenance Cost – Due to regular maintenance of the load switches and the changing of equipment due to problems related to contact wear; bearings, carbonized transformer oil, loose parts and oils leaks. The maintenance cost is high. Mainly the high maintenance cost is due to arcing which occurs during tap changing operation.

This topology is not well suited for on-load operation. The use of solid-state switches in place of the mechanical switches is discussed later in this chapter (6.2.1).

6.1.2. Classic OLTC
The classic OLTC is defined here as a purely mechanical system incorporating no semi-conductor device and comprising a tap changer selector section, a diverter section and some associated sensing and control systems. The diverter operates under load but in such a way that the load current is not interrupted. The tap transformer configuration described here is used mostly on high power transformers.

The diverter section suffers from heavy contact wear due to the unavoidable arcing; limiting the life of the diverter subsystem as contact material is lost at every operation. The arc at contact break dissipates considerable energy due to the large inter-tap current and is therefore the most significant cause of contact wear.

Figure 6.2 shows a representation of a commercially available oil-immersed OLTC system. The selector circuit does not switch under load. The diverter switch operates under load, and arcing occurs as the diverter arm moves from terminal A to D [25][26].

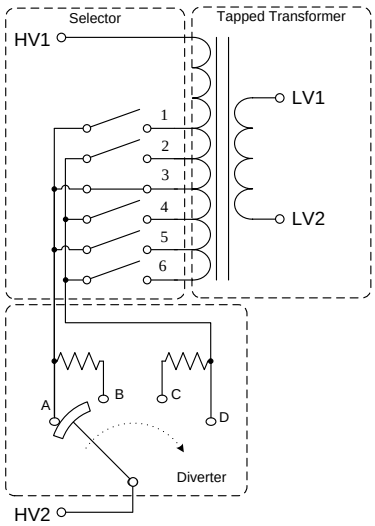

Figure 6.2: Classic On-Load Tap Changer [25][26].

[2] When a transformer is first energized, a current much larger than rated transformer current can flow for several cycles [**5**]. These currents are up to 5 times the rated current [**33**].

Contact wear

The tap change process involves the transfer of load current between electrical contacts and the momentary creation of an inter-tap circulating current, limited in magnitude by the diverter resistors, at the midpoint of the diverter movement.

The unavoidable arcing at the diverter contacts inherently limits the life of the diverter subsystem as contact material is lost at every operation, eventually necessitating the replacement of these parts. The arc at contact break dissipates considerable energy due to the large inter-tap current and is therefore the most significant cause of contact wear.

The actual commutation process is performed by the extinction at current zero-crossing of the electrical arc that is formed between contact surfaces at contact separation [26].

Operation

Figure 6.3 shows a simplified version of the switch operations during an on-load tap changing. The following is a short description of the events as the taps are changed from tap 3 to 4. In Figure 6.3(a) the load current is flowing through the selector switch at tap 3 and goes through the diverter circuit at contact A. In Figure 6.3(b) the selector tap switch 4 is selected. No current is flowing through tap 4 since the diverter switch is still at contact A. In order to change the tap, the diverter switch has to move from contact point A to contact point D. In Figure 6.3(c) the mechanical diverter switch has starts to move, first only contact point A is selected, then A-B, then B-C, then C, then C-D, then finally in Figure 6.3(d) contact D is selected. As the mechanical switch moves from B to C large inter-tap currents flow, as these currents are broken arcing occurs. When contact D is selected the entire load current is flowing through the selector tap switch number 4. The number 3 switch may then be opened.

In most cases a rotating switch is used for the selector circuit, but not for the diverter. The reason is that a rotating switch operating under load would have uneven wear due to arcing [25][26].

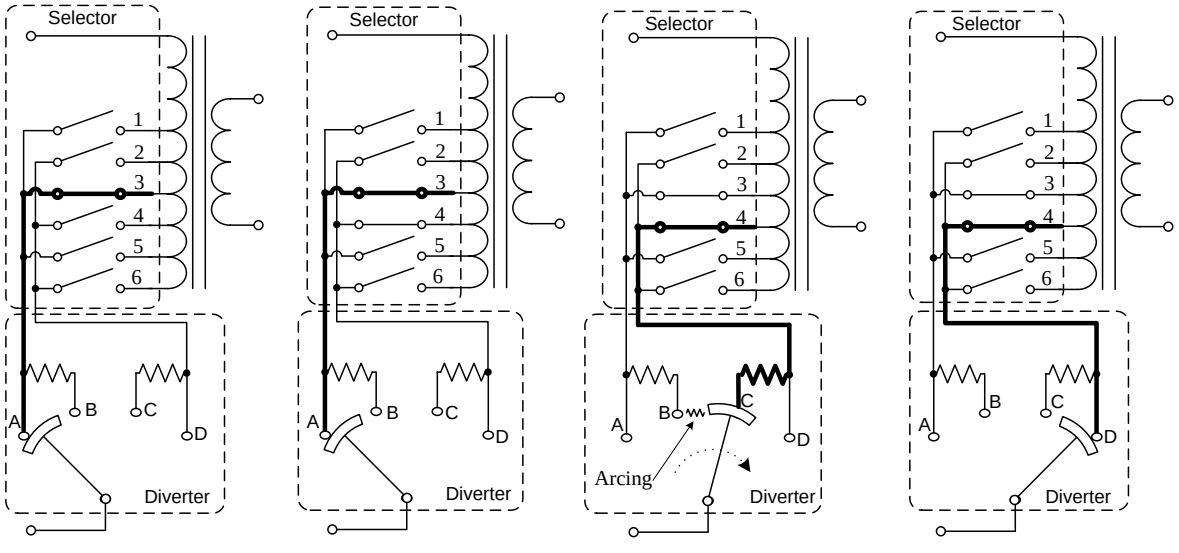

Figure 6.3: Basic switch operation for a classic mechanical OLTC.

Advantages
The following advantages are identified by [26]:

- Electrical simplicity – no aging of electric parts, high temperatures requires careful selecting and designing of electrical sensors or actuators. The mechanical system is very reliable; a purely electrically managed system may require multiple redundant sensing and control systems to provide the same level of fault tolerance.
- Interconnected simplicity – Without electric components electric isolation requirements may be significantly eased. In oil-immersed systems, the number of oil seals required for connections entering and leaving the transformer tank may also be reduced.
- Maintenance simplicity – A large mechanical system is relatively easy to dissemble and test, even for relatively unskilled workers. The same cannot be said for complex electrical systems.

Disadvantages
The following disadvantages are identified by [26] and [23]:

- Mechanical complexity – the mechanical system required to sequence the tap change steps is complex, complex drive mechanism, large number of specialist parts that leads to high costs.
- Physical size – The system must be designed around the mechanical layout necessary for synchronized operation of the selector and diverter but must also incorporate the standoff distances required between the tap connections and the separate phases which may result in conflicting design goals.
- Speed limitation – Mechanical systems are limited by the maximum speed they can achieve before parts become overstressed or fail. Resulting in a relative low maximum tap change speed.

6.2. Fully power electronic OLTC

Due to the limitations of purely mechanical OLTC various power electronic alternatives have been considered. A completely solid-state driven transformer eliminates the need for expensive maintenance due to arcing. It also has the benefit of higher tap change or output voltage change times [26][23].

6.2.1. Solid-state selector switches

The following circuit, Figure 6.4, is derived from the basic mechanical tap transformer shown in Figure 6.1. The selector circuit mechanical switches are replaces with high-power solid-state switches. There is no diverter circuit since no arcing will take place. There is no need for a complicated mechanical drive system since all of the switches can be controlled electronically.

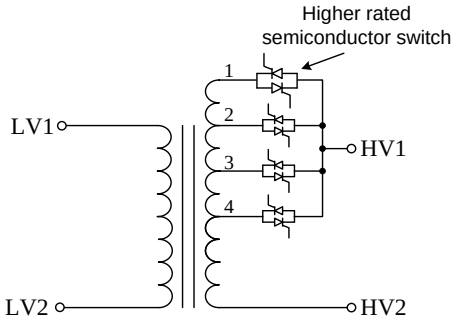

Figure 6.4: A single phase circuit OLTC implementing a solid-state switch selector circuit [24].

Solid-state Specifications
To help lower cost it is only necessary to oversize the solid-state switches at tap 1 to handle short circuit and overload currents, the other switches can have a lower current rating. This said the system needs to be designed to automatically select tap 1 in the case of overloads or faults. All switches will need to be able to handle fault currents for at least 10 ms otherwise they will break before the system can select tap 1. The specific rating of the switches will depend on which side of the transformer they are situated. If for example the taps are on the HV side of the transformer, the switches (switch 1 will have higher values for protection) will need to be rated at least the rated voltage and current values of the HV side of the transformer [24].

Advantages
The following advantages are identified in [23] and [24]:

- Response time – The solid-state devices can switch faster than their mechanical counterparts. Estimated time between consecutive tap changes 1 to 2 cycles.
- Wear – There is no moving parts and no arcing. This will lead to lower transformer oil contamination and possibly to longer intervals between maintenance, depending on the lifetime of the solid-states.

Disadvantages
The following disadvantages are identified in [23] and [24]:

- Costs – Large high-power solid-state devices are more expensive than mechanical switches. This design requires many such devices and is much more expensive than simple mechanical switches.
- Current handling – Solid-state devices have lower surge current handling capabilities than mechanical switches.
- Reliability – The solid-states will have to offer lifetime's equivalent to the mechanical system they are replacing. They will need to be able to operate under extreme conditions, including possibly high temperatures and humidity. Both of these will have a severe impact on both the reliability and efficiency of the electrical system.
- Wear mechanisms – It is much harder to determine the remaining live of a solid-state. With mechanical switches the wear can be visually observed.
- Power loss – Even though high efficiency is expected, in excess of 98%, the efficiency is lower than that of mechanical switches due to conduction losses in the solid-state switches.

6.3. Electronically assisted hybrid OLTC
Due to the inherent disadvantages of both mechanical and solid-state switches, various hybrid OLTC systems have been considered. Hybrid OLTC use both solid-states, to reduce arcing, and mechanical switches, for better efficiency. Three different options are considered. All of the topologies described here are derived from the classic mechanical OLTC used in high power tap transformers discussed in 6.1.2.

6.3.1. Solid-state diverter circuit
The simplest hybrid OLTC is one where the mechanical diverter switches are replaces by two solid-state switches, A and B in Figure 6.5. By substituting the mechanical switches in the diverter, all arcing is eliminated. Because there is no arcing there would be a considerable reduction in transformer oil contamination, associated with contact wear due to electrical arcing. Furthermore the need for inter-tap resistors is eliminated, since there would be no inter-tap currents.

Assuming, that for distribution level (11kv/400V), single tap changes were performed, single thyristors or GTO devices would be more than capable of handling the full load current in the on-state and block the inter-tap voltage in the off-state [26].

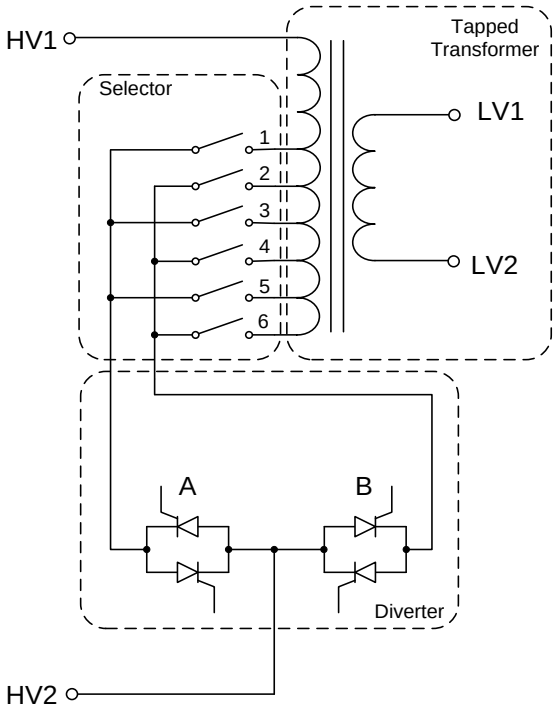

Figure 6.5: Single phase circuit for a OLTC implementing a solid-state diverter circuit.

Switch Specifications
The mechanical switches used in the selector circuit need only by able to block the voltage and conduct the rated current of the transformer. They are never needed to operate under load and need not be oversized to deal with fault currents.

The solid-state switches in the diverter circuit will need to be rated to block at least the rated voltage of the transformer. The solid-states will also need to be able to handle inrush and fault currents.

Advantages:
The following advantages are identified by [26]:

- No arcing – There is no arcing in the transformer during tap changes.
- Contamination – Due to the fact that there is no arcing, and thus no contact wear, the amount of transformer oil contamination is considerably less.

Drawbacks:
The following drawbacks are identified by [26]:

- Power loss – When comparing the power loss in the solid-state switches to that of the mechanical diverter switch, it is apparent that the solid-state switches will be less efficient due to conduction losses. The mechanical switch has a very small resistive voltage drop over the contacts, while the solid-states have a much higher forward voltage drop. The extra power loss leads to the need for thermal management.

- Reliability – The mechanical switches are known for their reliability. The solid-states will have to offer lifetime's equivalent to the mechanical system they are replacing.
- Wear mechanisms – It is much harder to determine the remaining live of a solid-state. With mechanical switches the wear can be visually observed.
- Costs – Large solid-state devices is significantly more expensive than simple mechanical switches.

6.3.2. Solid-state assisted diverter circuit

The following diverter switch topology is more complex than the one discussed above, in 6.3.1. The circuit in Figure 6.6 uses mechanical switches with bypass thyristors to reduce arcing without compromising efficiency. This approach, dubbed the "*thyristor assisted mechanical on load tap changer*", differs from the classic mechanical tap changer, discussed in 6.1.2, only during the tap change operation. The thyristors are responsible for the make and break of current, reducing arcing, and the mechanical switches conduct during normal operation, no power loss in steady state [27] [23].

Tests done on this type of tap changer showed an improvement in the lifetime of the mechanical switch by 75 times, when compared to a mechanical switch without bypass thyristors [28].

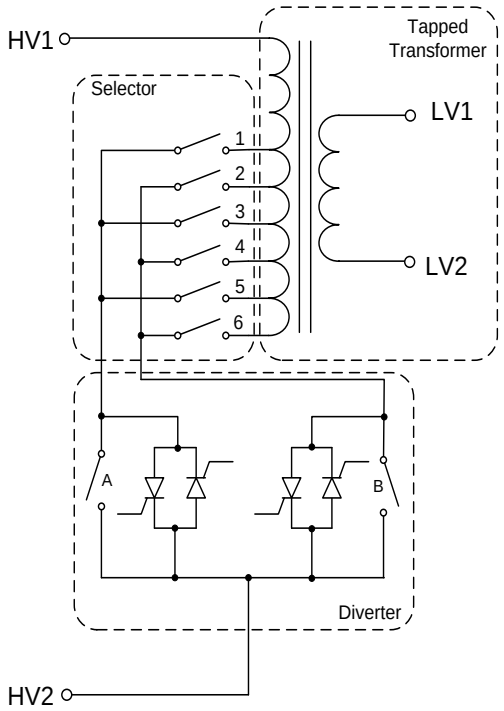

Figure 6.6: A single phase circuit of an OLTC implementing a solid-state assisted mechanical diverter circuit.

Switch Specifications

The tap selector should be rated to carry the rated current of the transformer, but not make or break this current. The mechanical switches (A and B) in the diverter and the thyristors should be able to conduct the rated current, break the rated current and block the rated voltage. The mechanical switches should also be able to handle fault current values until protection sets in [27].

Advantages

The following advantages are identified in [23], [27] and [26]:

- Arcing – Less arcing lead to longer switch life and reduces the need for routine maintenance.
- Power loss – There is very little power loss in the diverter circuit since the thyristors only conduct for a short period of time. The mechanical switches, which carry the current during steady state operation, are very efficient and can be modelled as short circuits.

6.3.3. Active diverter sub circuit

A tap changer transformer with an active hybrid diverter circuit was developed in [26],[29] and[28]. Figure 6.7 shows the circuit diagram for the diverter circuit. The selector circuit stays unchanged.

This circuit differs from the one discussed in 6.3.2 with the addition of a *controlled source circuit*, the grey area in Figure 6.7. Again the solid-state pairs are tasked with carrying current only while a tap change is in progress. The *controlled source* is used as an alternative current path during this time. Steady state current is carried by the mechanical switches (S_L and S_R). The voltage source V_A is *an H-bridge*[3] circuit consisting of high power MOSFET transistors. The use of a *controlled voltage/current source* enables the diverter circuit to create zero-voltage and zero-current conditions across the mechanical switches. This completely removes the need for mechanical switches to operate under load, also removing all arcing in the tap changer [26] [29] [28].

Tests done on this type of tap changer showed an improvement in the lifetime of the mechanical switch by 130 times, when compared to a mechanical switch without bypass thyristors. It is likely that the switch will fail due to other mechanical issues and not contact erosion caused by arcing [28].

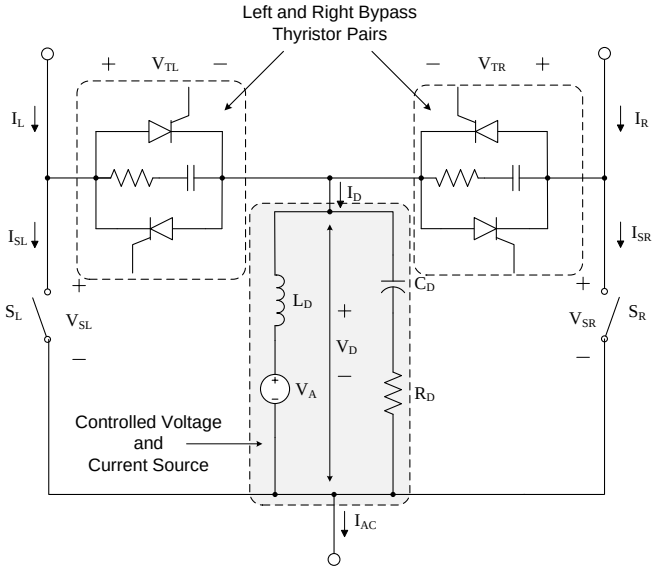

Figure 6.7: Single phase active diverter circuit for a OLTC transformer [29].

Operation

The following is a short description of the procedure used to create zero-current and zero-voltage conditions during tap switching operations, as described in [29]:

Zero-current may be created by triggering the corresponding *thyristor pair* into conduction and operating the *controlled source* in current mode, such that it produces a current equal to the load

[3] An H-bridge is an electronic circuit which enables a voltage to be applied in either direction

current. Now that all the current is flowing through the *controlled source* the switch S_L can be opened, as can be seen in Figure 6.8.

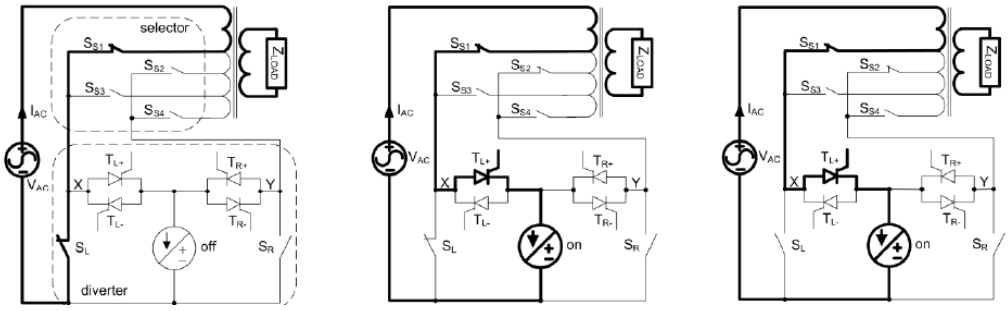

Figure 6.8: Opening a switch under zero-current conditions [29].

Zero-voltage may be created by triggering the *thyristor pair* into conduction and operating then *controlled source* in voltage mode so that the voltage across the closing switch is zero. If the voltage across SR is zero, the switch may be closed without arcing; operation can be seen in Figure 6.9.

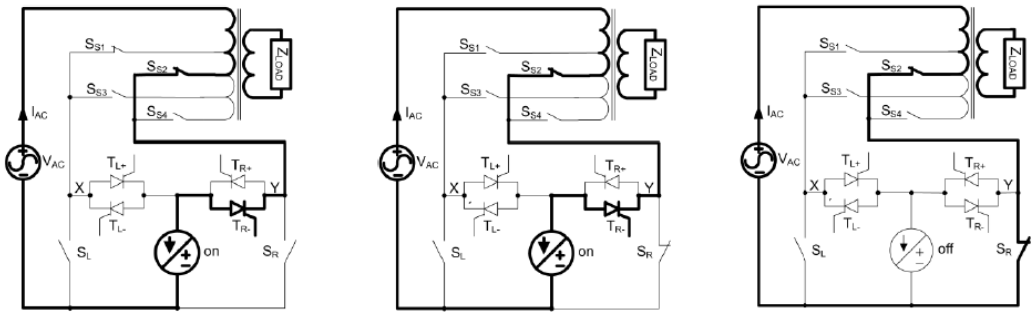

Figure 6.9: Closing a switch under zero-voltage conditions [29].

Chapter 7. Design and assembly of the OLTC transformer

In this chapter the development and assembly of the on-load tap changer utilising a solid-state assisted mechanical diverter circuit is discussed.

7.1. Comparing the relevant switchgear topologies

In the previous chapter various tap changer topologies are discussed. Table 7.1 gives a comparison of three of these tap changer topologies that meet the needs of this study. The topologies are compared based on expected switchgear price and the total complexity of the system. Other factors such as switch arcing are also taken into account.

Table 7.1: Comparison of the identified on load tap changer topologies

Topology Type:	Expected switchgear cost per transformer tap[4]:	Complexity of the switch control:	Other factors:
Solid-state selector switches	A solid state switch is required for each tap leading to high cost per transformer tap.	Only consists of selector switches. Very simple switch control needed.	No arching Very fast switch rate Conduction loss in solid-state switches
Solid-state diverter circuit	A small mechanical or electromechanical switch is required per transformer tap. In addition two solid-state switches are required. The per-tap price decreases as the number of taps increase.	The addition of the diverter circuit increases the complexity of the switch control when compared to the solid-state selector switch method above.	No arching Conduction loss in solid-state switches
Solid-state assisted mechanical diverter circuit	A small mechanical or electromechanical switch is required per transformer tap. In addition two solid-state switches and two mechanical or electromechanical switched are required. The per-tap price decreases as the number of taps increase but is slightly more expensive than the solid-state diverter circuit method.	The addition of the bypass switches slightly increases the complexity of the diverter control when compared to the solid-state diverter circuit switch method above.	Very low arching No conduction losses

[4] The solid-state switches are many times as expensive as the electromechanical contactors used during this study. Three-phase thyristor package was in excess of R 2000 (excluding fire angle control module), while 32A contactor was only R 382. Prices as on July 2011.

7.2. Chosen switchgear topology

On average a typical tapped transformer makes a tap change every 40 minutes. Due to the variable nature of the wind and the associated load changes the tapped transformer will be expected to make a tap change at least every 10 minutes. After careful consideration the Solid-state assisted diverter circuit topology shown in Figure 7.1 was chosen. This design allows for near arc-less tap changes due to the solid-state switches. The steady state conduction losses associated with solid-state switches are negated by the use of bypass switches. Using this type of switchgear topology should increase the maintenance interval by at least four times.

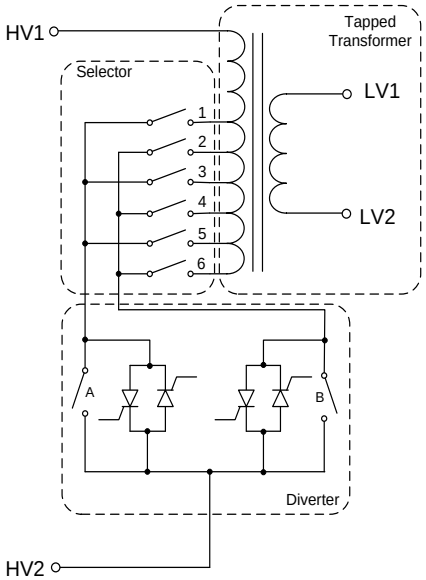

Figure 7.1: Solid-state assisted mechanical diverter circuit.

7.3. Components

As shown in Figure 7.1 the Solid-state assisted mechanical diverter circuit consists of a tapped transformer, a selector sub-circuit and a diverter sub-circuit. The system also requires control electronics. The mentioned components are discussed in this section. The design choice is made to design the switchgear to handle 150% the rated power of the generator being tested. That means that the switches and wiring must be able to continuously conduct at least 30 A. The three phase protection breaker between the transformer switchgear and the grid is also set to 30 A.

7.3.1. Tapped transformer

A small (30 kVA) three phase transformer is available for this project. The transformer was initially built to determine the effects of different voltages on the SSG, thus the inconsistent tap sizes. The transformer primary side is connected to the 400 V supply in the lab. For actual large scale use, at higher voltages, a star-delta transformer with uniform tap sizes should be used. The technical specification for the transformer used during practical testing of the switchgear is given in Table 7.2. A front and side photo of the transformer is shown in Figure 7.2 and Figure 7.3 respectively. The secondary voltage is varied by connecting the live grid wire to different tap terminals on the primary side. Nominal (1:1 ratio) voltage is achieved when live wire is connected to the number 3 tap.

Table 7.2: Transformer Specifications

Rated Values:												
Power Rating:	30 kVA			Number of Taps:								12
Max RMS Current:	43 A			Connection Type:								Y – Y
Primary Voltage:	390 V_{LL}			Core Material:								.35 mm silicon steel
Primary Tap #:	1	2	3	4	5	6	7	8	9	10	11	12
Secondary Voltage:	470	430	390	376	363	349	335	322	308	294	281	267

Figure 7.2: Front view of the 30 kVA tapped transformer used in this study.

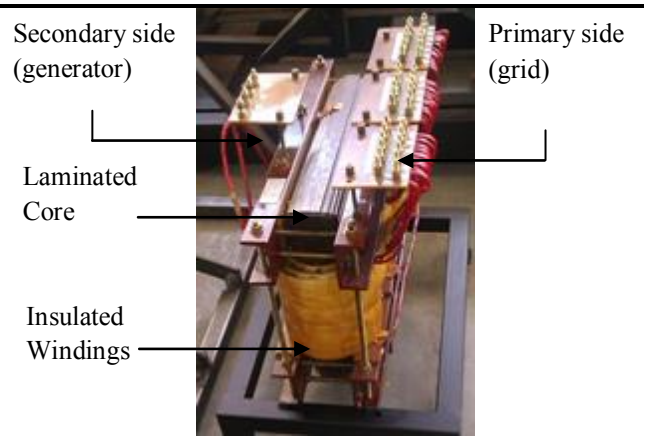

Figure 7.3: Side view of 30 kVA tapped transformer used in this study.

7.3.2. Selector sub-circuit

The selector sub-circuit consists of 12 mechanical or electromechanical switches used to select the transformer tap. As described in 8.3.2 the selector sub-circuit of the OLTC shown in Figure 7.1 does not operate under load, and needs only be rated with the capability to conduct the required amount of current and block the rated voltage. The Lovato BF18 range of contactors, shown in Figure 7.4, is rated to operate inductive loads of up to 18 A at 440 V. However according to the datasheet the contactor is rated to conduct 32 A. This switch is ideal for use in the selector sub-circuit. Since the transformer has 12 taps, the selector circuit will also require 12 BF18's. The even and the odd numbered contactors are connected between the transformer tapped terminals to a mutual bus as shown in Figure 7.5. The mutual bus is the connection point between the selector and diverter sub-circuits.

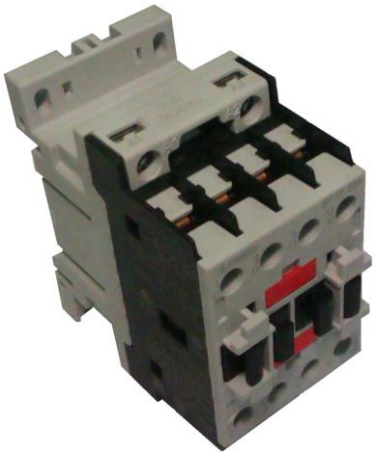

Figure 7.4: Lovato BF18 Contactor.

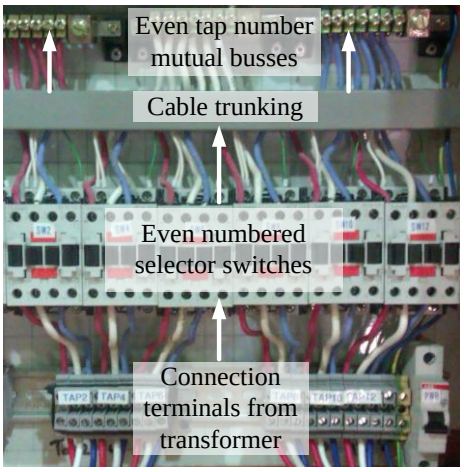

Figure 7.5: Photo of the connection between the tapped transformer terminals and the mutual bus.

7.3.3. Diverter sub-circuit

The diverter sub-circuit consists of two bypass switches and two three-phase back-to-back thyristors as shown in Figure 7.1. The diverter sub-circuit is situated between the relevant mutual bus and the grid protection breaker. The 30 A class-D[5] grid protection breaker is situated between the diverter circuit and the grid connection terminals. More details regarding the electrical connection are given in section 7.4 .

Bypass Switches

Although excessive arcing is not expected in the bypass switches it was decided to buy a pair that is rated to operate under rated current conditions. The current through and voltage over the bypass switch must be measured during switching operations to determine if a smaller switch can be used in future versions of the design. The Lovato BF32 range can conduct 56 A and is rated to switch inductive current of up to 32 A.

Solid-state switches

SEMIKRON is a well-known supplier of power electronic switches and semi-conductor related hardware. After talking with their technicians it was decided that the W3C3 package (3 back-to-back thyristor modules mounted on a heat sink) using SKKT 57/16 thyristors is adequate to test the OLTC. The maximum rated values of the thyristor package is given in Table 7.3. The rated current and voltage values for the thyristors are more than twice the required amounts, but this is the smallest available package. A photo of the W3C3 package is shown in Figure 7.6. The thyristors are controlled by the SEMIKRON RT380T control module in shown in Figure 7.7. This control module allows for easy control over the fire angle delay of the W3C3 package.

Table 7.3: Solid-state switch rated values and accompanying component costs[6]

	Rated Voltage [V]	Rated Current @ 35 ˚C [A]	Rated Current @ 80 ˚C [A]	Unit Price
SKKT 57/16 E	1700	95	55	R 1987.60
RT380T Driver				R 3198.00

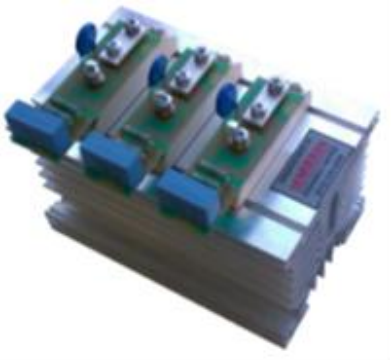

Figure 7.6: SEMIKRON W3C3 Thyristor pack.

Figure 7.7: SEMIKRON RT380T Driver module.

[5] Class-D is a slow breaker allowing for inrush currents of up to 10 times the tripping current for 100 ms.
[6] Prices in South Africa on July 2011

7.3.4. Control Electronics

The removable Texas Instruments F28335 DSP shown in Figure 7.8 is used to control the OLTC switches and in the future also the capacitor banks. The Digital Signal Processor (DSP) is mounted on the main controller board shown in Figure 7.10.

Outputs

Due to the high number of switches being controlled an extension board is required as shown in Figure 7.11. The two boards are mounted on top of each other and connected with a ribbon cable. The controller has the ability to switch up to 23 contactors.

Two digital to analog converters (DACs) are mounted on the main control board. These are used to send a voltage signal to the thyristor driver module.

Inputs

The main control board has the ability to measure six voltage signals. Three of these ports are used to measure the *abc* grid voltage at the diverter side of the protection breaker. The other three ports are not currently used. Figure 7.9 shows a separate circuit board containing three current probes used to measure the current flowing into the grid. This board is also connected to the main controller board.

Figure 7.8: Texas Instruments F28335 DSP.

Figure 7.9: Circuit board containing the current probes.

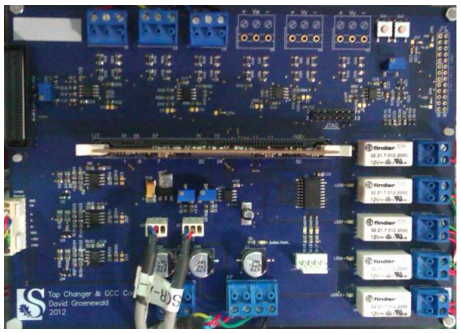

Figure 7.10: Main controller board housing a TI DSP.

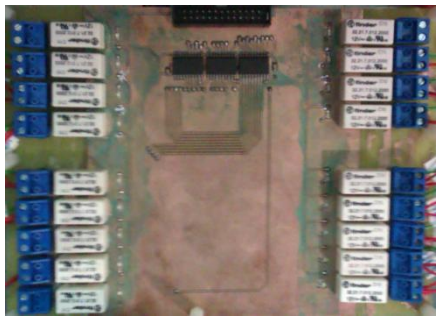

Figure 7.11: Extension board containing multiple relays used to switch the contactors.

7.4. Enclosure layout and assembly

The switches and other control hardware are mounted in an orange enclosure with the heat sinks mounted on top of the enclosure. The entire enclosure is mounted on a frame that sits above the transformer.

7.4.1. Transformer frame

The tapped transformer is mounted on a foot piece to enable the entire construction to be moved with a pallet jack. A frame is mounted over the transformer. The sides of the frame are normally closed to protect the public from the live transformer terminals. A photo of the transformer inside the enclosed

frame is shown in Figure 7.12. The enclosure housing the switchgear is mounted on top of the transformer frame.

Figure 7.12: Front view of the tapped transformer mounted inside an enclosed frame.

Figure 7.13: Front view photo of the enclosure housing the switchgear mounted on top of the transformer frame.

7.4.2. Enclosure layout

The proposed component layout for the transformer switchgear and other hardware is shown in Figure 7.14. A partial wire diagram for the odd numbered taps is shown in Figure 7.16. Switch 13 and 14 is for future use, possibly to switch capacitors. A photo of the actual enclosure with the internal components is shown in Figure 7.15.

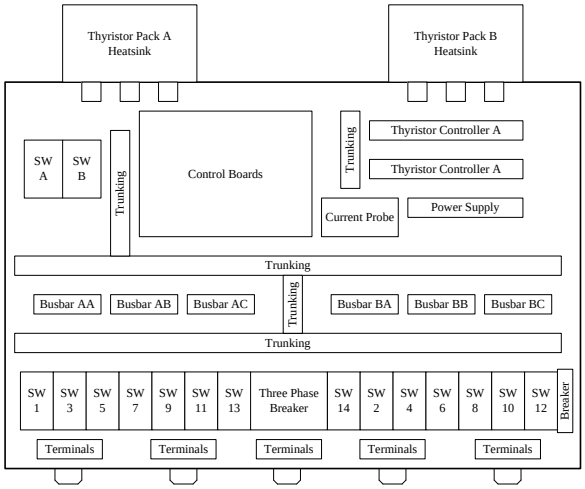

Figure 7.14: Component layout in electrical enclosure for the prototype OLTC.

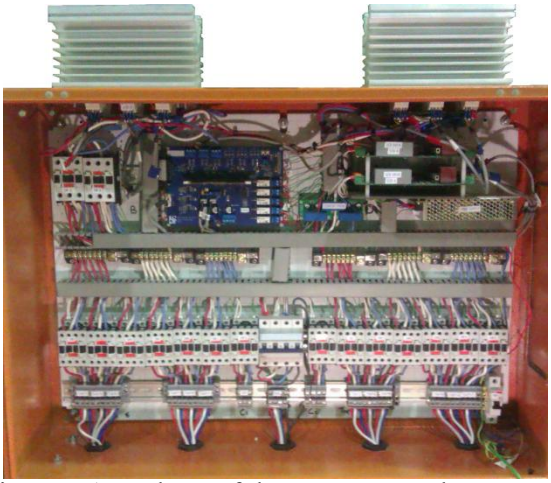

Figure 7.15: Photo of the components layout inside the enclosure.

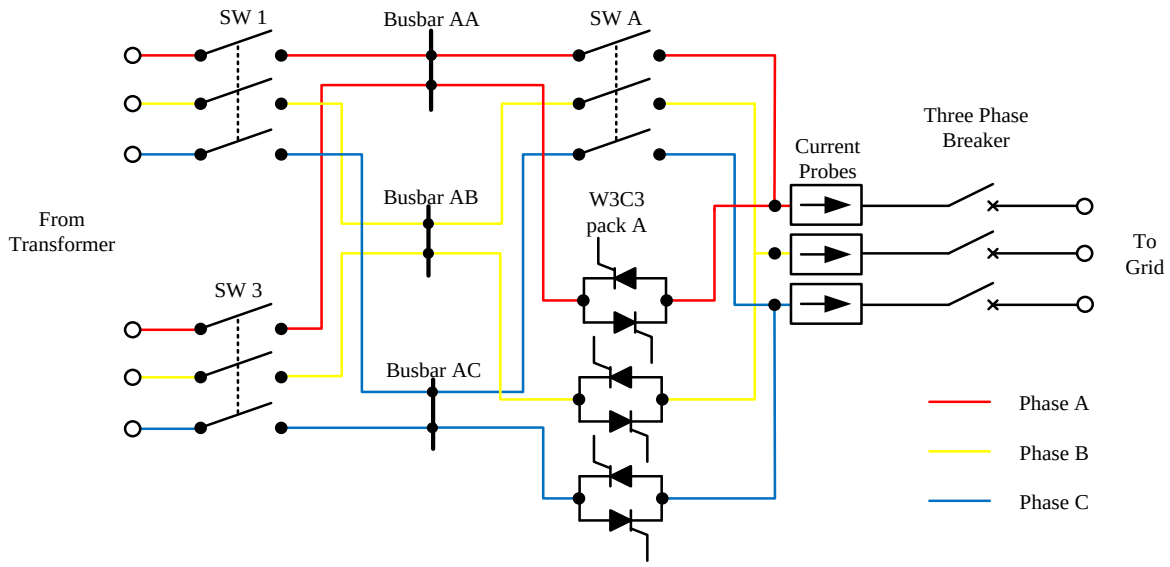

Figure 7.16: Partial component wiring diagram.

Chapter 8. Modelling and simulation of the OLTC transformer

In this chapter the various models created using the VHDL-AMS modelling language to simulate the performance and operation of an OLTC transformer is discussed. Accurate modelling allowed for the development and simulating of various programming functions before the prototype OLTC is tested. The inrush current and tap change operation are also described and simulation results are presented in this chapter.

8.1. VHDL-AMS modelling language

The models in this study were created by using the VHDL-AMS modelling language. The Verilog Hardware Description Language – Analog and Mixed Signal extension (VHDL-AMS) is a strict superset of the well known VHDL hardware description language. Meaning that it supports the well-known VHDL language plus the specific statements made for analog and mixed signal modelling. VHDL-AMS has become an industry standard mixed-signal description language for electronic and multi-domain systems and is used in various simulation programs such as Simplorer and SystemVision where it allows the user to simulate program logic on hardware models. VHDL-AMS language models are interchangeable between various programs (eg. you can use a Simplorer model in SystemVision). The language also allows for both simultaneous and concurrent statements.

8.2. Simulation program used

SystemVision is a powerful simulation program created by Mentor Graphics. The program supports VHDL-AMS, Spice and C languages allowing for hierarchical design of complex multi-domain circuit elements. The program has many built in models, but allows the user to create his/her own models.

8.3. Modelling the transformer

Two models are created for the transformer. The first is a magnetic model used to simulate the inrush current and the second is an equivalent circuit model using the parameters determined during the open circuit and short circuit tests. By using the equivalent circuit model in simulations where the non-linear core effects can be neglected the simulation speed is increased considerably.

8.3.1. Magnetic model

Figure 8.1 shows the magnetic model used to simulate the effect of core saturation. The star-star connected three phase transformer is simplified by modelling as three separate single phase transformers connected in star. The interaction between the windings (electrical domain) and the core (magnetic domain) are represented by (8.1) and (8.2),

$$\mathcal{F} = Ni, \tag{8.1}$$

$$v = iR_{winding} + N\frac{d\phi}{dt}, \tag{8.2}$$

where $\mathcal{F}$ is the motor motive force (MMF) generated by the current flowing in the winding, N is the number of winding turns, i is the current in the winding, c is the voltage applied at the transformer terminal, $R_{winding}$ is the resistance of the winding and ϕ is the flux generated in the transformer core.

The equations describing the non-linear transformer core are given in (8.3) – (8.5),

$$\mathrm{MMF}_P - \mathrm{MMF}_S = \quad Hl_{core}, \tag{8.3}$$

$$B = \quad \mu H, \tag{8.4}$$

$$\phi = \quad BA_{core}, \tag{8.5}$$

where H is the field intensity, l_{core} is the equivalent length of the core, B is the flux density and A_{core} is the cross sectional area of the core. The non-linear relationship between the flux density and field intensity, μ, of the core is inserted piece wise into the model. MMF_P and MMF_S is the motor motive force source in the primary and secondary winding as indicated in Figure 8.1.

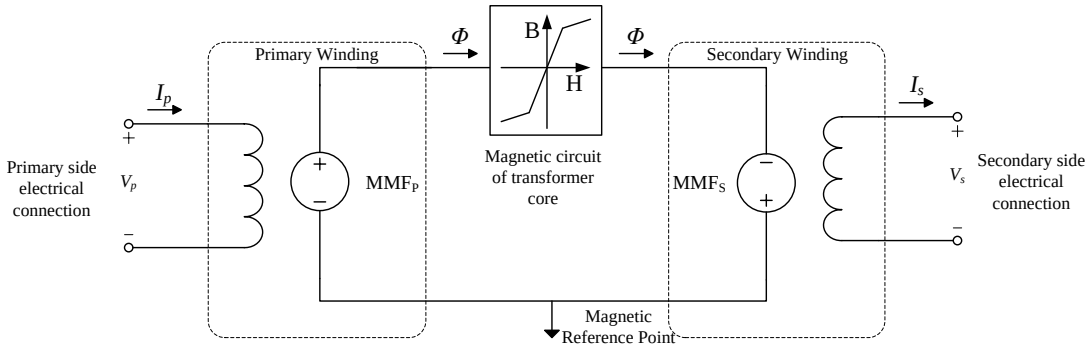

Figure 8.1: Single phase magnetic transformer model used during simulations.

8.3.2. Electrical model

The simplified electric model is used to simulate the transformer in cases where the core saturation and non-linear effects can be neglected. The star-star connected three phase transformer is simplified by modelling it as three separate single phase transformers connected in star. The circuit for the simplified single phase electrical transformer model is shown in Figure 8.2. Note that this model is very similar to the equivalent transformer model but the excitation branch is removed. The model is represented by (8.6) and (8.7),

$$v_P = \quad \frac{N_P}{N_S} v_S + R' i_P + L' \frac{dIi_P}{dt}, \tag{8.6}$$

$$i_S = \quad -\frac{N_P}{N_S} i_P, \tag{8.7}$$

where v_P and v_S is the voltage at the primary and secondary terminal of transformer respectively, i_P and i_P is the currents flowing at the terminals using the sign convention as shown in the circuit diagram. $\frac{N_P}{N_S}$ is the voltage ratio between primary and secondary side. R' and L' is the total series impedance of the transformer.

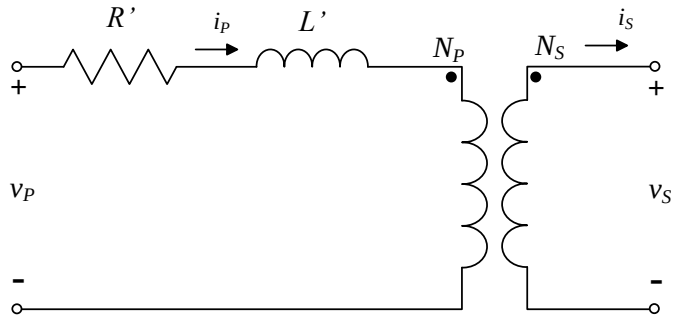

Figure 8.2: Single phase electrical transformer model used in the simulations.

8.3.3. Multi tap transformer model

The complete three-phase transformer along with the switchgear and the control functions are simulated in MGSV. The tapped transformer model is created by using the simple electrical model from section 8.3.2 along with the parameters as determined in section 8.4. The prototype transformer has 12 taps. Each tap is modelled by an individual three-phase transformer where the series impedances are scaled along with the turn ratio. The model for a single three-phase transformer is shown in Figure 8.3; the circuit on the left shows how each individual phase is connected to create the three-phase model, while the element on the right is used to represent the circuit on the left. The neutral terminals of the transformer are left unconnected. In Figure 8.3 P and S represent the primary and secondary terminals, while a, b and c refers to the various electrical phases.

As stated the transformer consists of 12 taps. The model for the 12 tap three-phase transformer is shown in Figure 8.4; the circuit on the left shows how each individual three-phase transformer model is connected to create the 12 tap three-phase model, while the element on the right is used to represent the circuit on the left. The numbers at the terminals refer to the tap number (1, 2, 3 or 4).

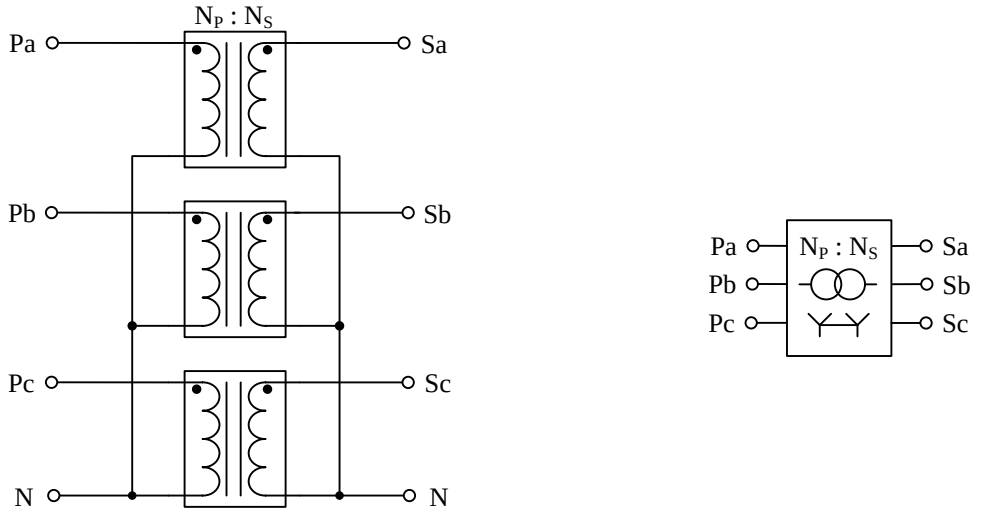

Figure 8.3: Single tap simple electrical transformer model for simulation.

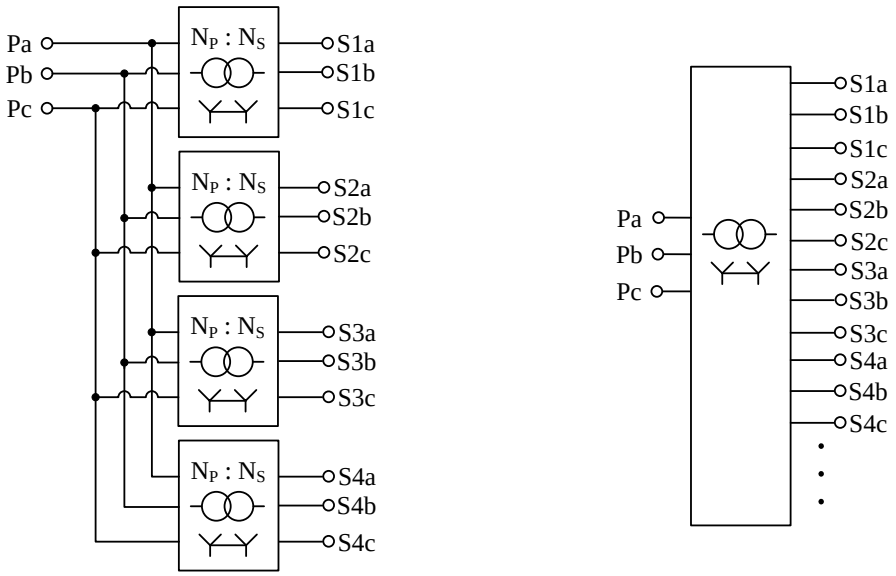

Figure 8.4: Multi tap model for a three-phase transformer used in the simulation.

8.3.4. Full OLTC transformer model

The single phase representation of the compete OLTC transformer circuit used in the simulations is shown in Figure 8.5. The model consists of the tapped transformer model shown in Figure 8.4, connected to the various selector switches and the thyristors in parallel with the bypass switches. This forms the full OLTC model used in all the tap changing simulations. This entire circuit can be represented by the symbol in Figure 8.6.

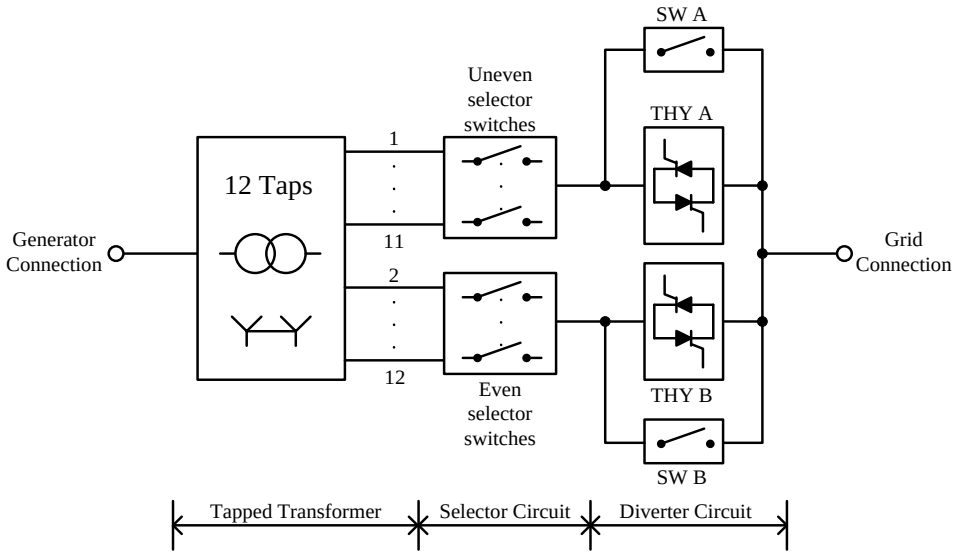

Figure 8.5: Single phase representation of the complete OLTC transformer circuit used in simulation.

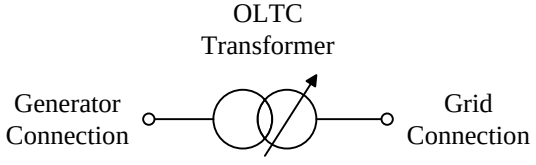

Figure 8.6: Symbol for an OLTC transformer.

8.4. Determine model parameters

In the following section the model parameters for the 30 kVA tapped transformer that is used in testing is determined. These parameters are used in the models described in the previous section.

8.4.1. Equivalent transformer core length and cross-sectional area

The measured dimensions of the transformer core are shown in Figure 8.7. The core can be represented by a magnetic circuit as shown in Figure 8.8(a), where the reluctance of the core ($\mathcal{R}$) is directly proportional to the length (l) of the core-part as given in (8.8),

$$\mathcal{R}_x \propto l_x \text{ and } \mathcal{R}_y \propto l_y. \tag{8.8}$$

The magnetic circuit in Figure 8.8(a) is reduced to the equivalent magnetic circuit in Figure 8.8(b). The equivalent reluctance of the core is given in (8.9),

$$\mathcal{R}_{eq} = \frac{2\mathcal{R}_x\mathcal{R}_y+\mathcal{R}_y{}^2}{2\mathcal{R}_x+2\mathcal{R}_y} + 2\mathcal{R}_x + \mathcal{R}_y. \tag{8.9}$$

Assuming that the core permeability and cross-sectional area is constant throughout the entire core, the equivalent core length for phase-a and phase-c is given in (8.10),

$$l_{eq,a} = \frac{2l_xl_y+l_y{}^2}{2l_x+2l_y} + 2l_x + l_y \tag{8.10}$$

Using the same methodology the equivalent core length for phase-b is given in (8.11),

$$l_{eq,b} = \frac{(2l_x+l_y)}{2} + l_y. \tag{8.11}$$

Using the measured values the equivalent core length for phase-a and phase-b is determined as 0.644 m. The equivalent core length of phase-c is 0.417m.

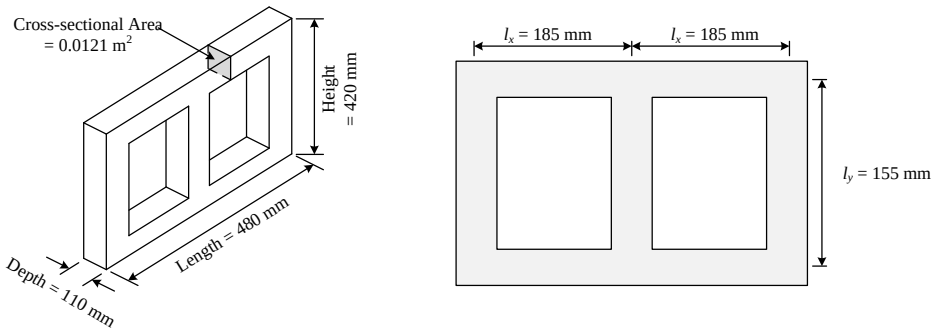

Figure 8.7: Measured dimensions of the 30 kW three phase transformer core.

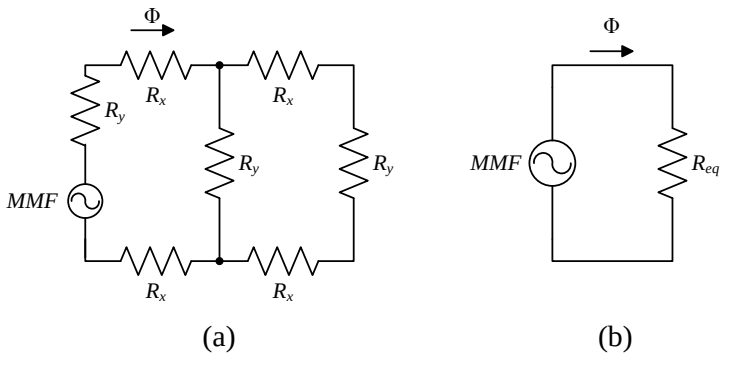

Figure 8.8: (a) Magnetic circuit for a three legged core, (b) Reduced magnetic circuit for a three legged core.

8.4.2. Transformer core magnetization curve

The transformer core appears to be manufactured from .35mm silicon steel laminations. ArcelorMittal produce different types of steel for different application. The various B-H curves for steel used in low voltage transformers were plotted in Figure 8.9. As seen in Figure 8.9 the various steel grades tend to act the same at deep saturation.

The averages of the different curves were used to create Figure 8.10. The gradient of the curve in deep saturation was used to linearly extrapolate the values. The purpose of Figure 8.10 is to approximate the permeability of the core during deep saturation. This information is useful when we calculate the inrush current of the transformer.

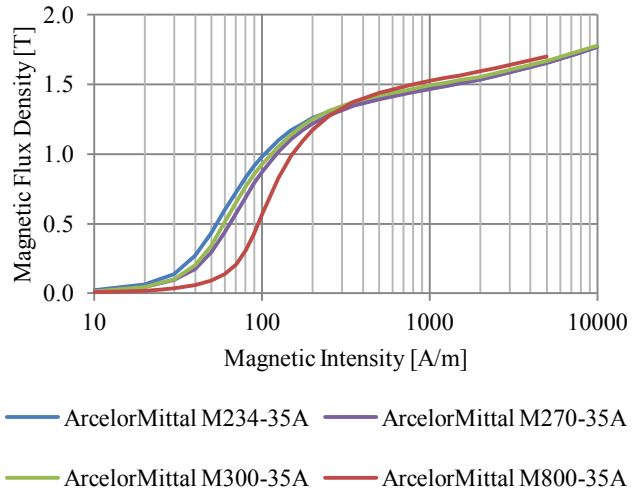

Figure 8.9: B-H Curve for various grades of .33mm silicon steel laminations as manufactured by ArcelorMittal [30].

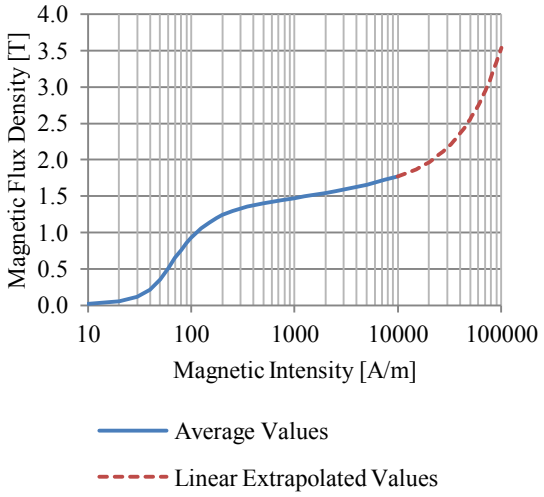

Figure 8.10: Averaged B-H curve for .33mm silicon steel laminations.

8.4.3. Number of turns on nominal tap

Looking at Figure 8.10 we will see that the core will start to saturate at a magnetic flux density of about 1.2 T. From (8.5) the maximum expected flux in the core is calculated to be 0.015 Wb. The number of turns on the nominal transformer tap is determined using (8.12),

$$V = N\frac{d\Phi}{dt}, \tag{8.12}$$

where V is the per phase RMS voltage applied to the transformer terminals, N, is the number of turns and $\frac{d\Phi}{dt}$ is the rate at which the flux in the transformer core changes. The rate of at which the flux changes is roughly determined as 3 Wb/s using Figure 8.11. The number of transformer turns is calculated to be 76.

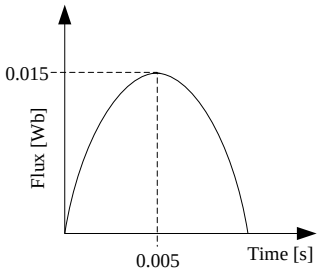

Figure 8.11: Partial flux waveform used to determine the rate at which the flux changes.

8.4.4. Series impedance

The parameters for the equivalent transformer model are determined by doing the open circuit and short circuit tests. The test results waveforms are shown in Figure 8.12 and Figure 8.13, while the results are summarised in vector form in Table 8.1. The core-loss resistance and magnetisation reactance can be calculated as shown in (8.13) – (8.14):

$$\mathrm{Z}_{core} = \frac{V_{oc}}{I_{oc}}, \tag{8.13}$$

$$= \left[\frac{1}{R_c} + \frac{1}{X_m}\right]^{-1}, \tag{8.14}$$

where Z_{core} is the shunt core impedance, V_{oc} and I_{oc} are the open-circuit voltage and current respectively. R_c is the core-loss resistance and X_m is the magnetisation reactance of the core. During the short-circuit test it is assumed that the excitation current is negligibly small, because of the small voltage applied. Using (8.15) – (8.16) the series impedances are calculated:

$$\mathrm{Z}_{eq} = \frac{V_{sc}}{I_{sc}}, \tag{8.15}$$

$$= Z_1 + Z_2', \tag{8.16}$$

where V_{sc} and I_{sc} are the short circuit voltage and current respectively. Z_1 is the primary side series impedance and Z_2' is the secondary side series impedance referred to the primary side.

Using the measured values the circuit values for the transformer side without taps are calculated and given in Table 8.2. The values for R_1 and X_1 are related to R_2 and X_2 via the turn's ratio. For every different tap, and thus different turn's ratio, the values for R_1 and X_1 change as given in Table 8.3.

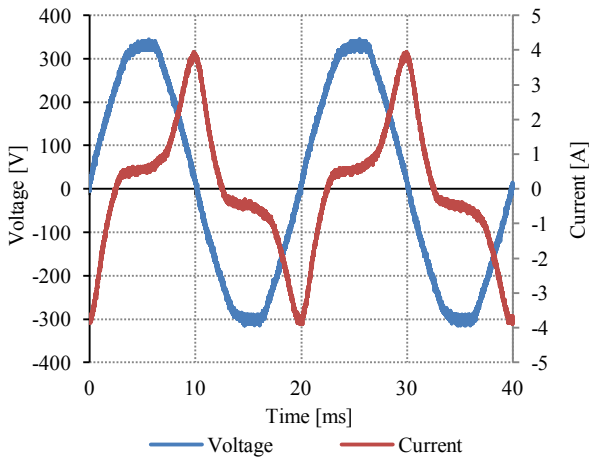

Figure 8.12: Measured per phase voltage and line current during the open circuit test.

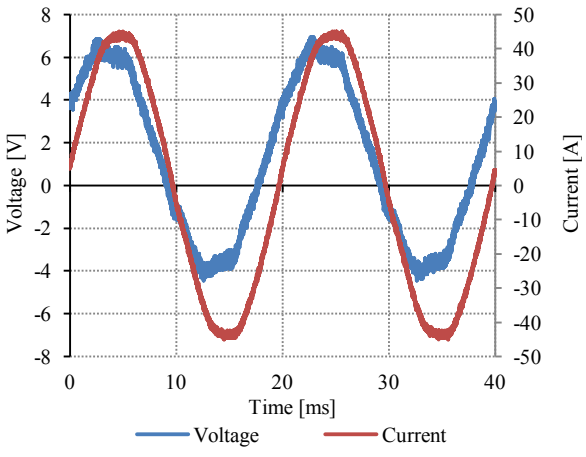

Figure 8.13: Measured per phase voltage and line current during the short circuit test.

Table 8.1: Transformer open-circuit and short-circuit test values

$\boldsymbol{V_{oc}} =$ 230∟0° V	$\boldsymbol{V_{sc}} =$ 4.2∟0° V
$\boldsymbol{I_{oc}} =$ 1.7∟80° A	$\boldsymbol{I_{sc}} =$ 30.3∟10° A

Table 8.2: Equivalent electrical circuit model parameters

$\boldsymbol{R_2}$	0.067 Ω	$\boldsymbol{R_c}$	920 Ω
$\boldsymbol{X_2}$	0.012 Ω	$\boldsymbol{X_m}$	162 Ω

Table 8.3: Series impedances for the various taps

Tap #	1	2	3	4	5	6	7	8	9	10	11	12
N_2/N_1	1.20	1.10	1.00	0.96	0.93	0.89	0.86	0.82	0.78	0.75	0.71	0.67
$\boldsymbol{R_1}$	0.080	0.074	0.067	0.064	0.062	0.059	0.057	0.054	0.052	0.050	0.047	0.045
$\boldsymbol{X_1}$	0.014	0.013	0.012	0.011	0.011	0.010	0.010	0.009	0.009	0.009	0.008	0.008

8.5. Inrush current

When a transformer is first energized it might draw a large current for a few cycles. This current is known as inrush current or transient inrush current. Inrush currents easily reach values of up to 40 times the rated steady state current of the transformer and can last about 10 cycles[25] [31] [32].

Figure x shows the transfer function block diagram for the current in (8.19). The block diagram is created using (8.15) to (8.19),

$$\Phi = \frac{1}{N}\int [v(t) - i(t)r]dt, \tag{8.15}$$

$$i(t) = k(\Phi)\Phi(\mathrm{t}) , \tag{8.16}$$

$$B = \frac{\Phi}{A_{core}}, \tag{8.16}$$

$$B = \mu(\Phi)H, \tag{8.17}$$

$$H = \frac{\mathrm{N}i}{l_{core}}, \tag{8.18}$$

$$i(t) = \frac{l_{core}}{NA_{core}}\frac{\Phi(\mathrm{t})}{\mu(\Phi)}, \tag{8.19}$$

where the permeability, μ , is non-linear and must be inserted piece wise into the transfer function.

Inrush current tend to stress the insulation of the windings and increase the possibility of breakdown and short-circuit between turns. Inrush currents can also disrupt the operation of sensitive electrical loads such as computers and can cause protection systems to operate incorrectly [31] [25].

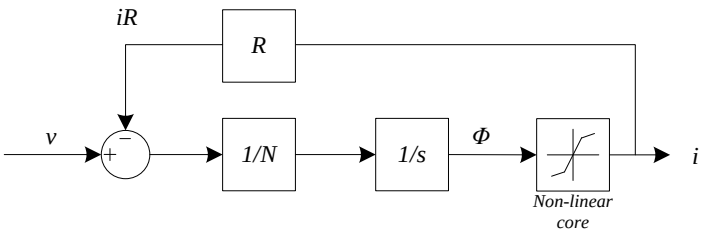

Figure 8.14: Transfer function block diagram for the inrush current.

8.5.1. Inrush current simulation without soft-starting the transformer

Using the magnetic transformer model, the worst case inrush current is simulated. During this simulation there is no residual flux in the transformer core. As shown in Figure 8.15, the transformer is connected to the grid when the phase-A voltage is at a zero crossing. This causes the transformer core to go into deep saturation leading to inrush current as shown in Figure 8.16.

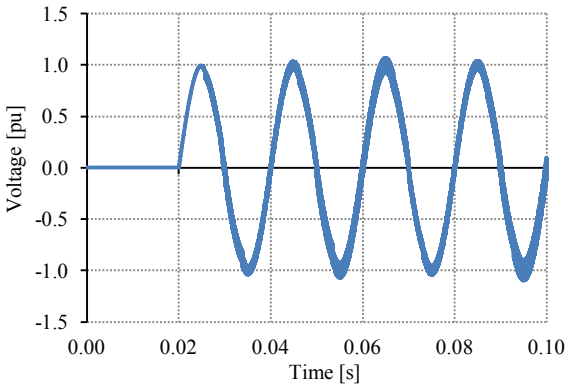

Figure 8.15: Simulated per phase voltage at the transformer primary side terminal.

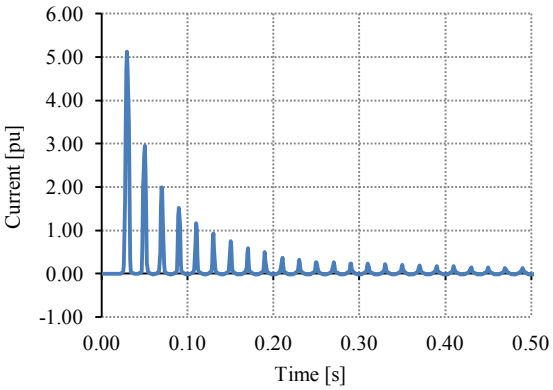

Figure 8.16: Simulated per phase line current at the transformer primary side terminal.

8.5.2. Soft start method

The thyristor switches used in the diverter circuit of the OLTC switchgear makes it possible to also soft start the transformer. Although large power transformers are not often soft started in practice, it does simplify the protection devices needed for this study.

To minimize inrush current the transformer must be energized when the phase voltages are at a maximum value. As shown in Figure 8.17 the solution can be realised by implementing zero-crossing detection and then operating power electronic switches after 90˚ delay. Each phase will have to be operated individually. This method should ensure that minimum inrush current is generated during transformer start up.

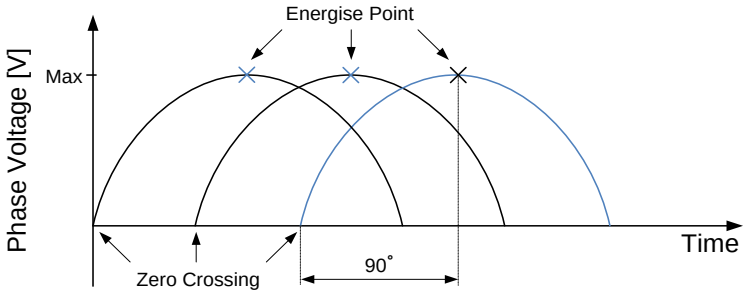

Figure 8.17: Simplified voltage waveform showing optimal soft starter switch timing.

8.5.3. Transformer soft-start simulations

The circuit showed in Figure 8.18 is simulated using MGSV. The idea is to recreate the conditions in the testing lab. The grid is modelled as an ideal three-phase 400 V line-to-line voltage source with a with a series impedance of 0.15 + j 0.15 as determined in [19].

Although all three phases were simulated only phase-A is discussed. The main controller instructs the three-phase thyristor controller to fire the thyristors with a 90˚ fire angle, as shown in Figure 8.17. At time 0.055 seconds the phase-A voltage waveform reaches maximum value (90˚) and the thyristor

gate (G2) is set to high. The simulated terminal voltage and line current is shown in Figure 8.19 and Figure 8.20 respectively.

Because the flux generated in the core is 90˚ out of phase with the voltage applied at the terminals, the current is also 90˚ out of phase with the voltage. This causes the thyristors to conduct as if the controller is sending the signal to operate at 0˚ delay angle. After the transformer core is excited the main controller gives the thyristors the command to operate at 0˚ fire delay.

As seen in Figure 8.20 no inrush current occurred. The small dc offset seen in Figure 8.20 decreases until the current waveform becomes symmetrical after about 10 seconds.

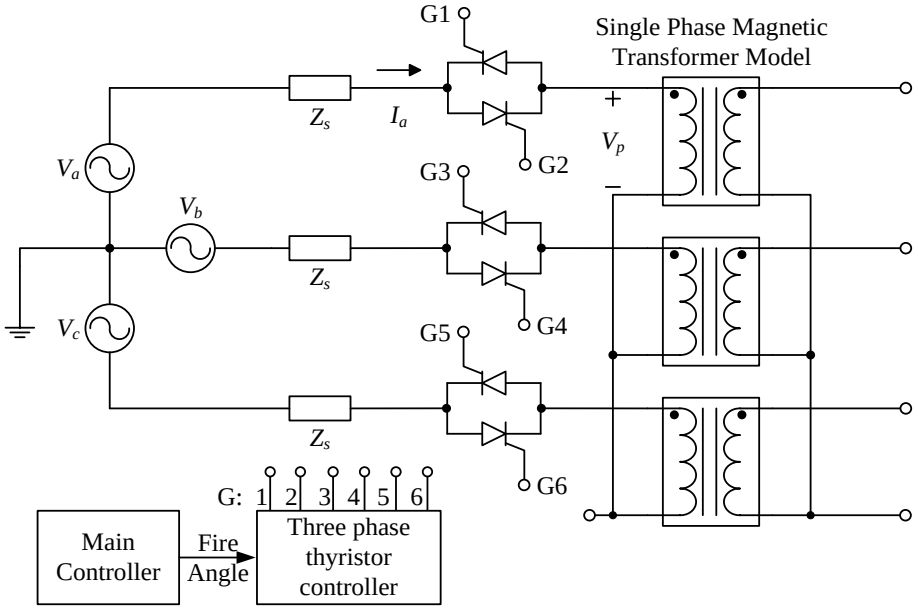

Figure 8.18: Three phase simulation setup for transformer soft start.

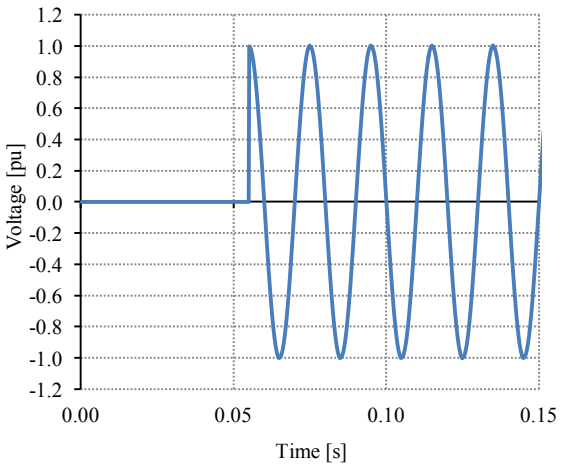

Figure 8.19: Voltage at the transformer primary side terminal during soft start.

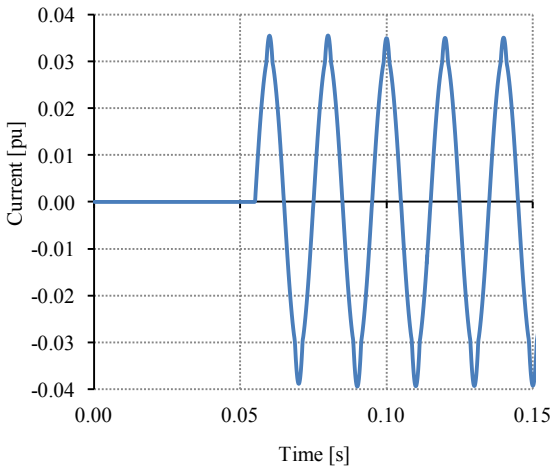

Figure 8.20: Current at the transformer primary side terminal during soft start.

8.6. Tap change simulation

The working of the solid-state-assisted OLTC is simulated using the MGSV package. The modelling parameters for the transformer are given in Table 8.2 and Table 8.3. The parameters for the generator are shown in Table 2.1.

8.6.1. Switching sequence

Consider the circuit showed in Figure 8.21 where the OLTC represents the solid-state-assisted transformer circuit as shown in Figure 7.1. At the start of the simulation the generator is connected to the grid (sync switch is already closed) via the OLTC transformer. Switch 3 (tap 3) and bypass switch A is closed and conducting rated current. The main controller receives the instruction to decrease the generator terminal voltage by 5% (tap 4 must conduct). The switching sequence is shown in Figure 8.22. The sequence start when switch 4 (tap 4) closes; switch 3 is still closed and conducting current. Thyristor A is pulsed to be able to conduct and bypass switch A opens. At this point tap 3 is conducting via the thyristor. Thyristor B is pulsed to start conducting at the same time as thyristor A stops conducting. The generator is now connected to the grid via tap 4 and thyristor B. Bypass switch B closes and thyristor B stops conducting current. This concludes the sequence of events for a single tap change.

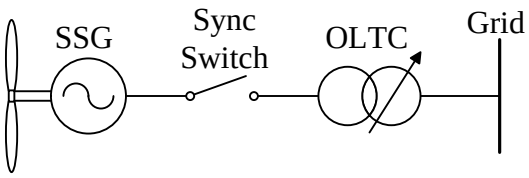

Figure 8.21: Single line diagram of the simulated circuit.

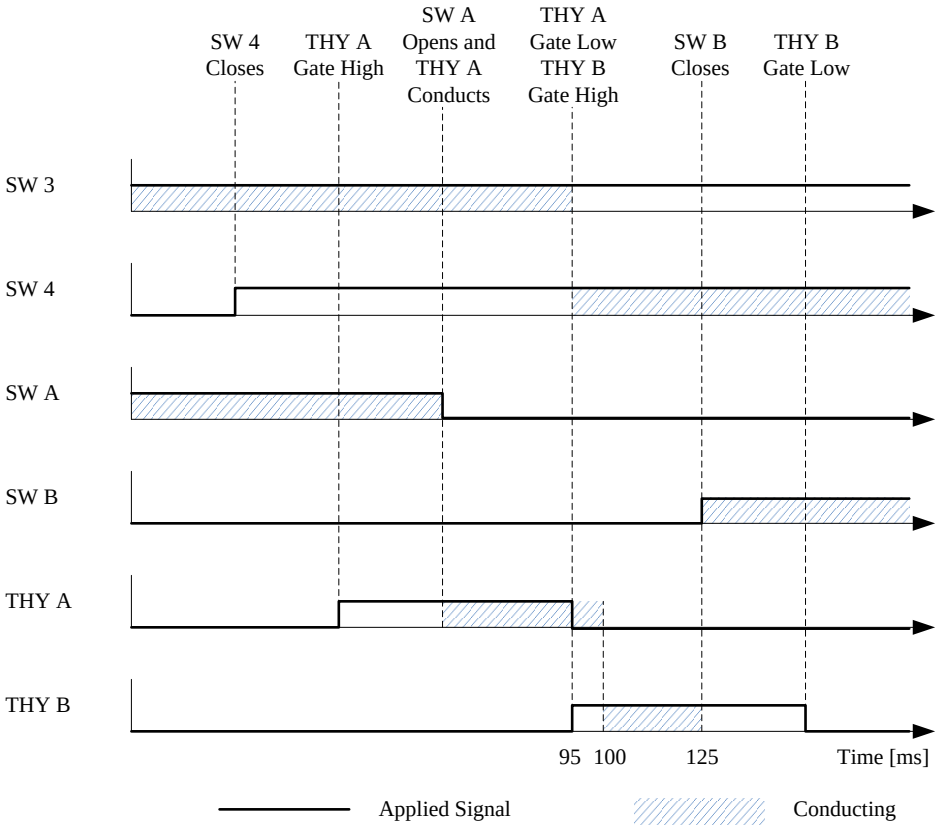

Figure 8.22: Example of the switch signals during a tap change.

8.6.2. Voltage and current during change-over

An extract of the simulated voltage and current waveform at the load current change-over between thyristor A and B is shown in Figure 8.23 and Figure 8.24. At time 95 ms the controller makes the gate of thyristor A low and thyristor B high as shown in Figure 8.22. When the current in Figure 8.23 goes through zero (at 99 ms) thyristor A stops conducting. When the voltage in Figure 8.24 goes through zero (at 100 ms) thyristor B starts conducting. The voltage spikes in Figure 8.24 are caused by the current and voltage not being perfectly in phase. This is due to the load being relatively inductive. These voltage spikes will only occur when the thyristors are conducting. At any time after thyristor B starts conducting, bypass switch B may be closed. For this simulation bypass switch B is closed at time 125 ms, as shown in Figure 8.22 and Figure 8.24. When the bypass switch closes, thyristor B stops conducting current. This concludes the tap switching operation.

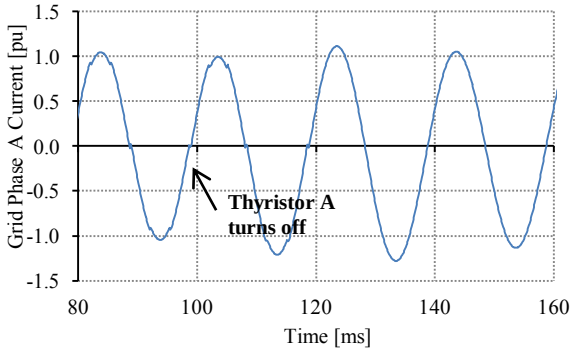

Figure 8.23: Simulated grid line current.

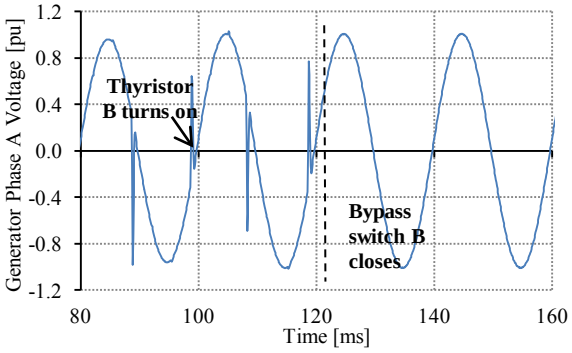

Figure 8.24: Simulated phase voltage waveform

8.6.3. Simulation to determine generator current transient caused by the tap change

To simulate the current transients associated with changing the terminal voltage on the 15 kW SSG the same simulation setup as used in Figure 8.21 is used. For this simulation rated torque is applied to the SSG. At 2.5 seconds a tap change occurs to decrease the terminal voltage by 0.05 pu.

In the simulation the controller measures the three-phase voltage and current waveforms at the grid connection point, and using the basic algorithm as shown in Figure 8.25 the angle and magnitude of the current and voltage vectors are determined. The current overshoot, as shown in Figure 8.26, is determined to be 0.025 pu with a 5% settling time of 2 ms. But for the case where the generator voltage is increased the transient spike will go upwards, leading to an expected overshoot of 0.12 pu and a 20 ms settling time.

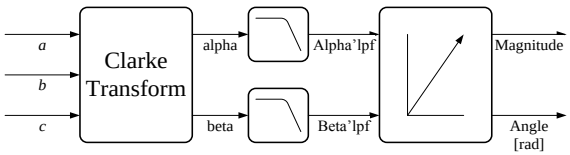

Figure 8.25: Block diagram for calculating the current and voltage vector magnitude and angle.

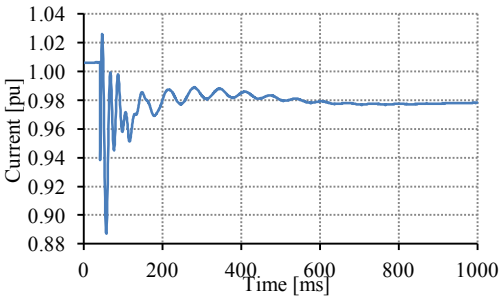

Figure 8.26: Simulated current vector magnitude response due to terminal voltage change at rated applied turbine torque.

8.7. Conclusion with regards to OLTC simulations

From the simulation results no considerable transients are expected during a tap change operation. The voltage spikes shown in Figure 8.24 must be inspected during practical testing. The simulation results show that the solid-state assisted OLTC transformer topology is able to provide voltage control without disrupting the output current and appear to be a good solution to control the terminal voltage of the generator.

Chapter 9. Reactive power control simulations

The current small scale SSG wind turbine has no reactive power control device. Reactive power control forms a vital part of any generation device since reactive power is used to help regulate the voltage across a transmission line. In this chapter various reactive power compensation devices for the SSG are discussed. A method using the tapped transformer to change the excitation mode of the generator and using a small capacitor bank to deliver additional reactive power is simulated. The goal is to reach the reactive power requirements as specified by the grid code.

9.1. Reactive power and voltage regulation

Wind farms are often situated in rural areas where the local grid may easily reach its voltage control limit. Wind turbines traditionally use induction generators, and these require reactive power operate [33]. As shown in Figure 9.2 the network voltage, at some distance from the nearest voltage control device, will increase or decrease depending on the current load condition of the transmission line. During low transmission line voltages the system operator may require the WEF to a controllable amount of reactive power to increase the grid voltage. During high transmission line voltages, the system operator may instruct the WEF to absorb a controlled amount of reactive power to decrease the grid voltage.

The power factor angle for a generating device can be represented by the phasor diagram in Figure 9.1 where β is the current angle with respect to the per phase voltage angle. As shown in Figure 9.1 the output reactive power of a generator is positive when the current is lagging ($\theta < 0$) the voltage; the generator is absorbing reactive power when the current angle is leading the voltage angle ($\theta > 0$).

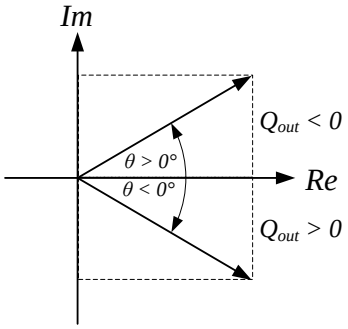

Figure 9.1: Phasor diagram illustrating reactive current.

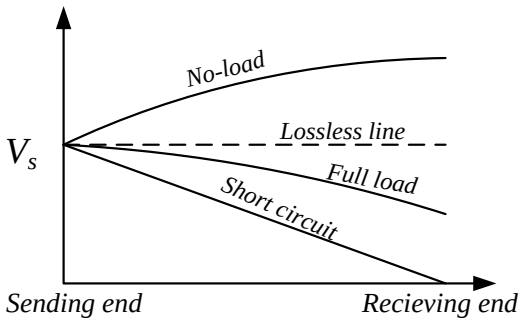

Figure 9.2: Voltage profile for uncompensated transmission line [34].

9.2. Grid code requirements

For the reasons stated in the previous section the grid code specifies that the WEF must have the capability to control its reactive power output under both normal and abnormal grid voltage conditions.

9.2.1. Normal operation

During normal operations, voltage and frequency within normal range, the system operator will specify how the WEF must control the reactive power output. There are three reactive power control functions: Q-control, PF-control and Voltage-control. The system operator will specify which of these control functions to use [20].

Reactive power or power factor control

Under Q-control the WEF must control the reactive power output independently of the active power and voltage at the PCC. This is represented by the vertical line in Figure 9.3. Under power factor control the reactive power is changed proportionally to the active power output. This is represented as a line with a constant gradient in Figure 9.3. After a set-point is received from the system operator, the WEF has 2 seconds to commence and 30 seconds to finish changing the reactive power output. The system is required to have accuracy such that the reactive power does not deviate by more than ±2% of the set-point value or ±0.5% of the rated power, depending on which yields the highest tolerance [20].

Voltage control

Under voltage control the reactive power, and transformer tap position, is controlled to regulate the voltage within a set range between V_{max} and V_{min} as shown in Figure 9.4. After a voltage set-point is received from the system operator, the WEF has 2 seconds to commence and 10 seconds to complete the voltage change. The system is required to have accuracy such that the voltage does not deviate from the set-point by more than 2%. The droop line shown in Figure 9.4 is the p.u. voltage change caused by a p.u. change in reactive power. Each WEF must be able to perform the control within its dynamic range, when the voltage control has reached the WEF's dynamic limit it shall await a possible overall control from a tap changer [20]. This control function is only applicable to large wind farms where the generating capability of the wind farm starts toexceeds the fault levels of the utility at the PCC.

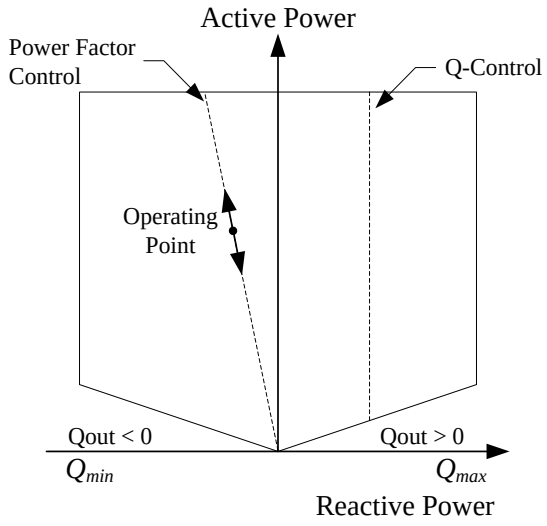

Figure 9.3: Reactive power control functions for a WEF [20].

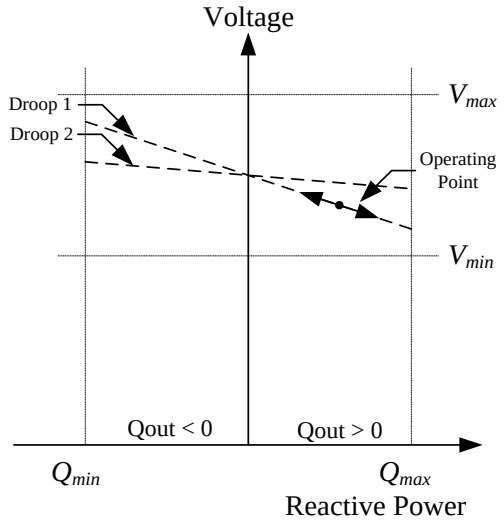

Figure 9.4: Voltage control for a WEF [20].

9.2.2. Abnormal operation

During voltage drops the WEF is required to provide voltage support by injecting a controlled amount of reactive power into the network as shown in Figure 9.5. During voltage surges, the WEF is required to absorb reactive power as specified in Figure 9.5. The reactive power control mechanism is required to follow the support curve in Figure 9.5 with a max tolerance of ±20% after 100 ms. During these fault conditions reactive power supply has primary priority above active power production. However as far possible active power output must be maintained, a decrease in active power output during fault conditions is acceptable [20].

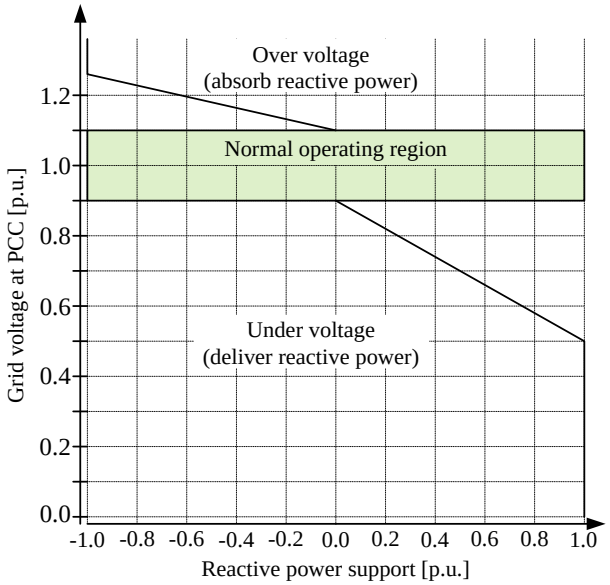

Figure 9.5: Reactive power support during voltage drop or surges [20].

9.2.3. Reactive power control requirements for a WEF smaller than 20 MVA

Figure 9.6 and Figure 9.7 show the reactive power and voltage control requirement for a WEF rated active power of less than 20 MVA. The WEF must be designed to supply reactive power of at least 0.975 lagging and 0.975 leading, calculated at rated active power output available from a minimum generation of 20%. During start-up the reactive power flow at the PCC may not exceed 5% of rated active power for more than 5 seconds [20].

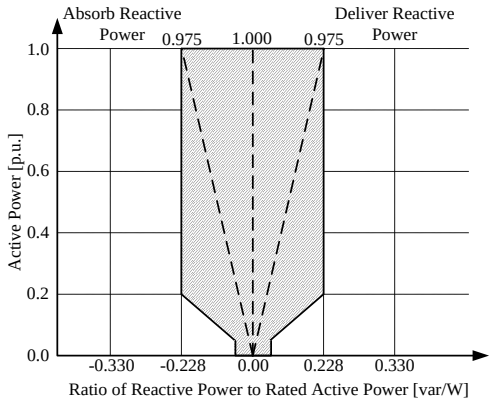

Figure 9.6: Reactive power requirement for a WEF smaller than 20 MVA [20]

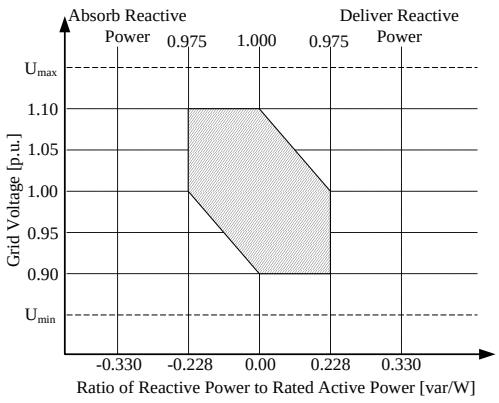

Figure 9.7: Voltage control requirements for a WEF smaller than 20 MVA [20]

9.2.4. Reactive power control requirements for a WEF larger than 20 MVA

Figure 9.8 and Figure 9.9 shows the reactive power and voltage control requirement for a WEF larger than 20 MVA operating under normal conditions. The WEF must be designed to supply reactive power of at least 0.95 lagging and 0.95 leading, calculated according to the rated active power output of the WEF. This reactive power must be available from a minimum generation of 20% to full rated active power output. No WEF may import more than 5% reactive power for more than 5 seconds from the network during start-up [20].

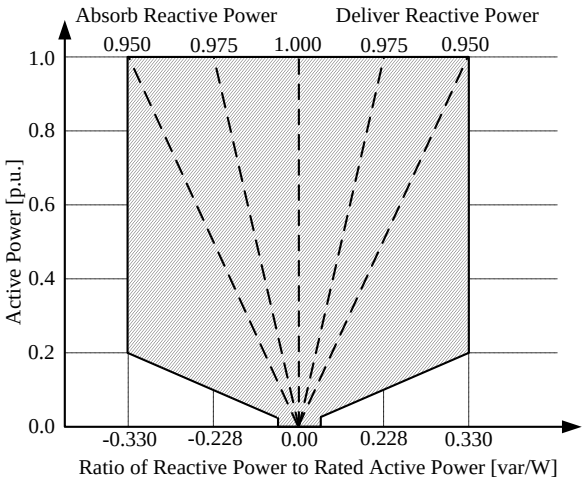

Figure 9.8: Reactive power requirement for a WEF larger than 20 MVA [20].

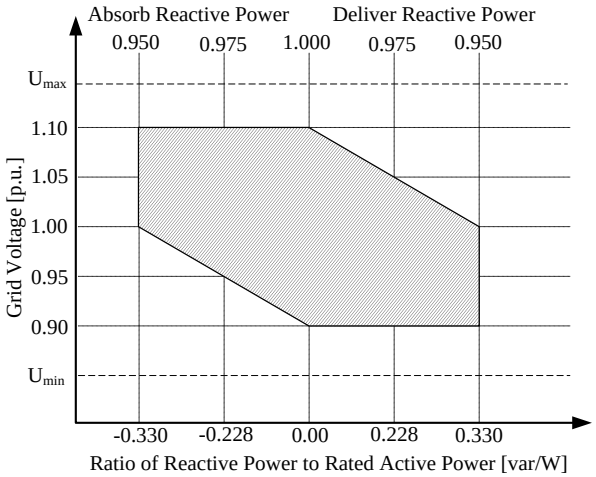

Figure 9.9: Voltage control requirements for a WEF larger than 20 MVA [20].

9.3. Control methods

There are various methods for delivering/absorbing reactive power. Four standard methods are described below.

9.3.1. Synchronous condenser

Synchronous condensers are often used as compensation devices for power systems [35]. A synchronous condenser is a synchronous machine designed to generate reactive power [36] [37]. Once connected to the electrical network it neither drives, nor is it driven by other rotating machines [38]. The amount of reactive power that a synchronous generator absorbs or delivers can be controlled by controlling the excitation of the machine [18]. Figure 9.10, Figure 9.11 and Figure 9.12 show the phasor diagrams for under, unity and over excited synchronous machines with E_A the induced per phase voltage, V_φ the per phase terminal voltage and I_A the current. Note that the magnitude of E_A stays constant, the angle of E_A changes as the magnitude of V_φ changes.

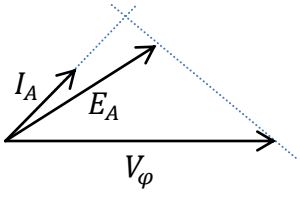

Figure 9.10: Phasor diagram of an under excited synchronous machine [18]

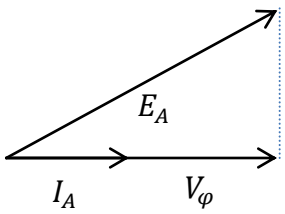

Figure 9.11: Phasor diagram of an unity excited synchronous machine [18]

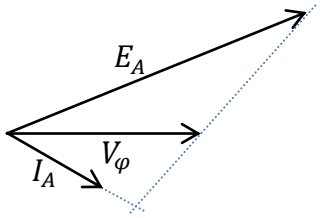

Figure 9.12: Phasor diagram of an over excited synchronous machine [18]

Advantages

The control for a synchronous condenser is very flexible. Once the machine is connected to the grid, the reactive power can be continuously controlled by adjusting the field current. The control can be fully automatic so that a desired power factor or voltage can be maintained. Due to the ease of adjusting the output power, the machine can be put on or taken out of the electrical network, without creating large disturbances [38].

Synchronous condensers have no switching transients and are not affected by harmonics (may even absorb some harmonics). Condensers will not produce excessive voltages and will provide voltage support during short faults [39].

Disadvantages
Although the initial cost of the condenser and other equipment is relatively low, the operating cost is high due to power losses [38].

9.3.2. Static VAR compensator (SVC)

Wind farms often use a fixed capacitor bank rated to meet the required reactive power compensation at maximum plant output. But due to wind fluctuations it is necessary to adjust the reactive power source very frequently to maintain the desired power factor or terminal voltage. One method of doing this is to install a thyristor controlled reactor in parallel with the fixed capacitor bank [40]. The SVC acts as a variable source of reactive power [41].

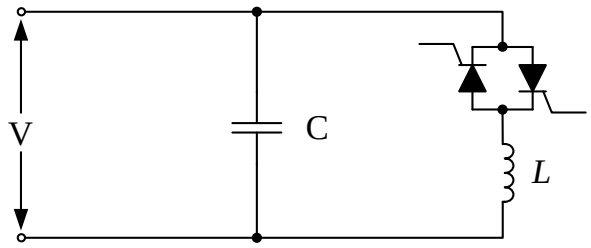

Figure 9.13: Single phase circuit for a Static VAR Compensator [40]

Advantages
The SVC works better than fixed capacitor banks, because the amount of reactive power delivered can be controlled. It has lower transients and also improves the voltage ride through capability of the system [40]. Simulations done by [41] shows that a SVC can greatly improve the bus voltage and provide variable reactive power.

Disadvantages
The initial cost of the SVC system is higher than for fixed capacitor [40]. It has slower response when compared to STATCOM and also induces low order harmonics due to the anti-parallel thyristors [41].

9.3.3. Static synchronous compensator (STATCOM)

The STATCOM is a shunt device and is part of the Flexible AC Transmission Systems (FACTS) family using power electronics to improve network stability. The static compensator (STATCOM) consists of a transformer (normally step down) and a voltage-sources converter (VSC) connected in shunt with a transmission line [42] [43]. In most cases the DC voltage support is provided by a DC capacitor with small energy storage capacity, hence there should not be any active power exchange [44]. The AC voltage difference across the leakage reactance of the transformer produces reactive power exchange between the STATCOM and the power system [42]. Thus by controlling the output AC voltage of the VSC the reactive power flow can be controlled. As shown in Figure 9.14 no active power flows into or from the STATCOM. In recent years the use of STATCOMs has gained popularity in wind energy applications [41].

An example of a STATCOM installed in a single-machine infinite-bus power system is shown in Figure 9.14. When using a capacitor to provide DC bus voltage the voltage V_2 must be shifted slightly behind V_1 to compensate for the transformer and VSC losses. Then by changing the voltage magnitude the reactive power flow can be controlled. When $V_1 > V_2$ the STATCOM is absorbing reactive power, and when $V_1 < V_2$ the STATCOM is supplying reactive power to the network [43].

Advantages
STATCOMs provide very good control and have very fast response time, leading to improved voltage ride through capability and better control of reactive power [41]. STATCOMs are less sensitive to voltage changes than SVCs and capacitor banks [35].

Disadvantages
STATCOMs are very expensive due to expensive switches and the additional transformer [41].

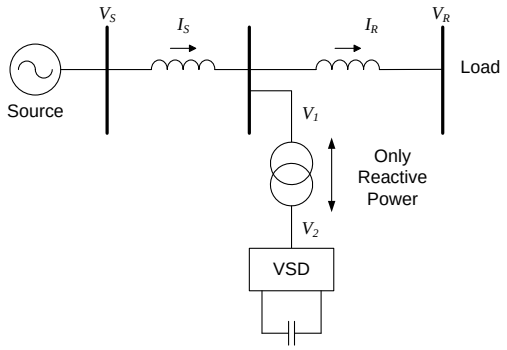

Figure 9.14: STATCOM installed in a single-machine infinite-bus power system [42][43].

9.3.4. Shunt capacitor

Wind farms commonly use a fixed shunt connected capacitor bank [35] rated to compensate for reactive power at maximum power output [41]. Capacitor banks are normally mounted in the bottom of the tower or in the nacelle [35]. Sometimes the capacitor bank consists of up to four individual capacitor banks in parallel. These can be switched in and out and compensate for reactive power at 25%, 50%, 75% and 100% of rated active power output.

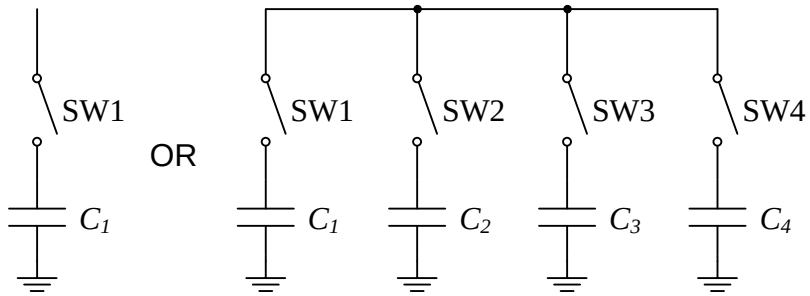

Figure 9.15: Shunt capacitor banks used for power factor correction.

Advantages
Capacitor banks are regarded as the easiest and cheapest method of providing reactive power [41].

Disadvantages
Capacitor banks do not provide any voltage support, on the contrary the amount of reactive power they supply is very sensitive to the voltage ($Q = V^2\omega C$). Thus if the voltage drop slightly, the amount of reactive power provided will drop considerably [35] [41].

Switching multiple capacitor banks provide better control over the amount of reactive power delivered but create large over voltage spikes, as is shown later in simulation [41]. Capacitors are very susceptible to harmonics (5^{th} and 7^{th}), and it is recommended that the capacitor bank be designed as a harmonic filter by adding tuned inductors.[39].

9.3.5. Summary of the various reactive power compensation methods
A comparative summary of the reactive power compensation devices discussed in section 9.3 is given in Table 9.1 below.

Table 9.1: Comparison of reactive power compensation equipment

Equipment Type	Control Type	Response Time	Voltage Support	Initial Cost	Operating Cost
Synchronous Condenser	Continuous	Fast	Very Good	Medium	High
SVC	Continuous	Fast	Poor	High	Medium
STATCOM	Continuous	Fast	Good	High	Medium
Capacitor Bank	Discreet	Slow	Poor	Low	Very low

9.4. Power factor control using the OLTC transformer
The OLTC can be used to control the terminal voltage of the SSG in discreet steps. The internal flux and induced voltage stays constant in a PM generator. By changing the terminal voltage of the generator the excitation-mode can be controlled [33]. Decreasing the terminal voltage has the equivalent effect of over-excitation and the generator will start to produce reactive power. The opposite is also true; increasing the terminal voltage will cause the generator to absorb more reactive power.

Using the equivalent dq-model for the 15 kW SSG the power factor vs. terminal voltage is plotted, in Figure 9.16, for various power levels. The downside of this method to control the output reactive power is the effect that decreasing the terminal voltage has on the overall efficiency of the generator as shown in Figure 9.17.

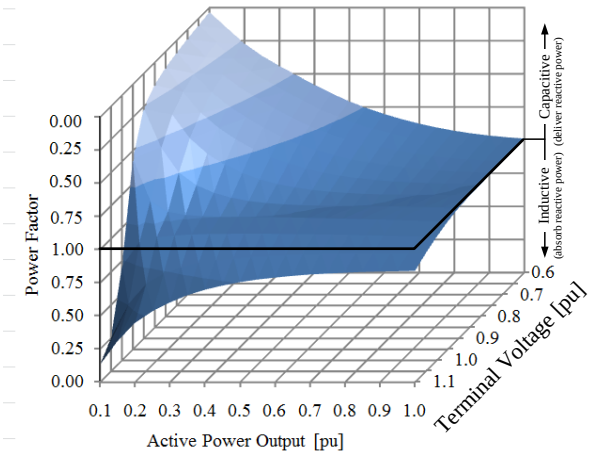

Figure 9.16: Power factor angle for variable power and terminal voltage.

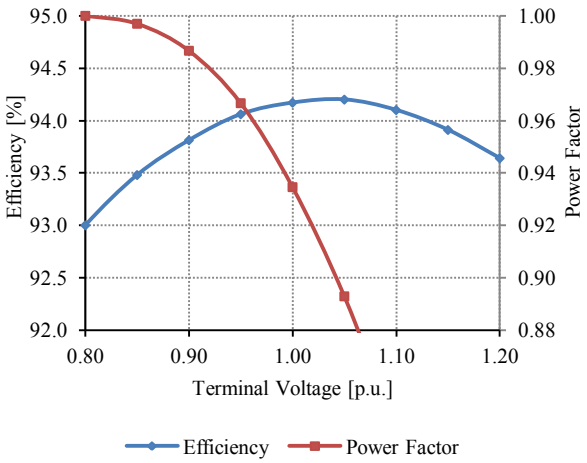

Figure 9.17: Simulated efficiency vs. terminal voltage at rated power.

9.4.1. Obtaining unity power factor using the OLTC

Using the OLTC to control the reactive power output of the 15 kW SSG is simulated using MGSV. The simulation setup is shown in Figure 9.18. The SSG is connected to a 400 V bus with the grid line impedance values as determined by [14].

The turbine torque versus time signal shown in Figure 9.19 is applied to the SSG-model during the simulation. The controller measures the current and voltage at the PCC and then changes the generator terminal voltage, using the OLTC, in such way that the power factor angle is at or near zero, i.e. at unity power factor. The change in voltage applied to the generator terminals at the various power levels is also shown in Figure 9.19. Note how the applied terminal voltage decreases as the applied torque increases.

Figure 9.20 shows the change in power factor with the change in active power output due to the applied turbine torque from Figure 9.19. At low power levels the difference in power factor between the different taps is very large. In this case the controller is unable to control the power factor at power levels below 0.2 pu.

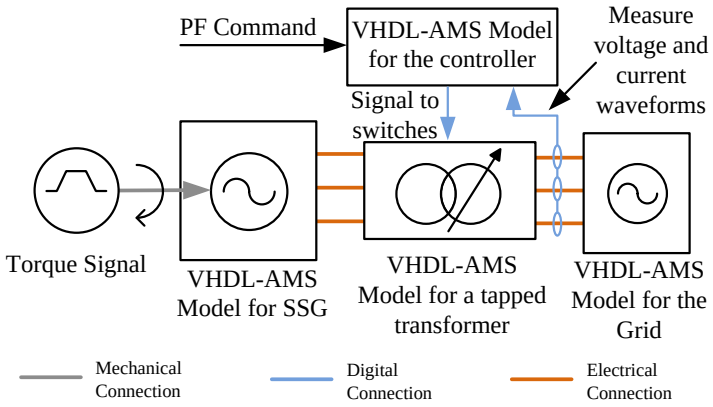

Figure 9.18: Reactive power control simulation setup in MGSV.

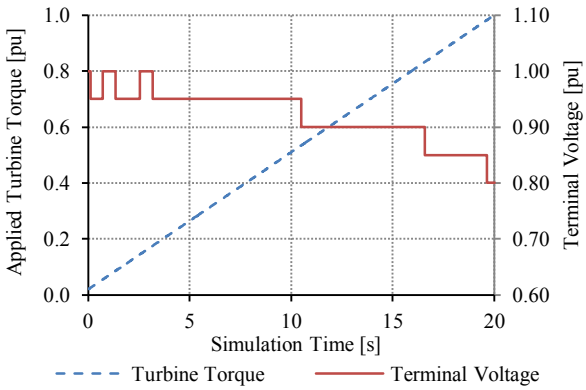

Figure 9.19: Applied turbine torque and terminal voltage during the simulation.

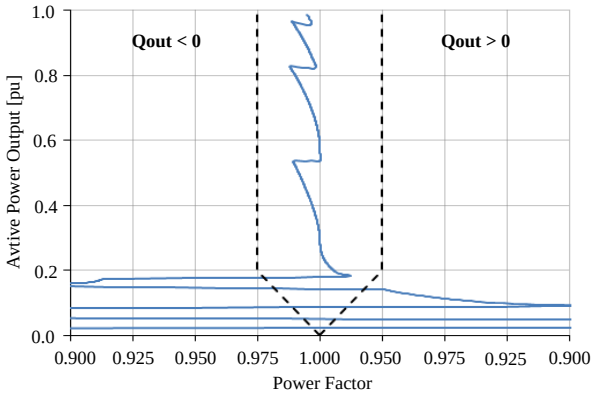

Figure 9.20: Power factor during simulation when using the OLTC.

9.4.2. Remarks

Figure 9.20 shows the power factor vs. active power output while the controller tries to keep the power factor at unity. As can be seen the discreet steps are very large and exceed the minimum accuracy as specified in the grid code. At low active power (below 0.2 p.u.) levels the controller is not able to control the reactive power in a sensible manner.

A solution to this problem is to increase the number of taps and decrease the amount by which the voltage changes between consecutive taps. The taps sizes should also be consistent. Another possible solution is to add another method of providing reactive power. The effect of adding two small capacitor banks is investigated. The goal is to decrease the amount by which the reactive power output changes per control operation.

9.5. Method for determining the individual capacitor sizes

The capacitor bank will be used to provide reactive power in between consecutive tap changes. In order to specify the size of the capacitors, the amount by which the reactive power output of the generator changes per tap must be determined. The reactive power output for the generator at various power and voltage levels are shown in Figure 9.21. As can be seen from Figure 9.21 the change in reactive power output versus the change in voltage ($\Delta Q/\Delta V$), decreases as the active power output increases. The expected operating area for a typical SSG WTG is between 0.2 and 0.4 p.u. active power output (3 to 6 kW in Figure 9.21). The reactive power output vs. active power for this region is shown in Figure 9.22. As indicated in Figure 9.22 the expected change in reactive power (ΔQ) per tap operation is about 1000 var in this operating region.

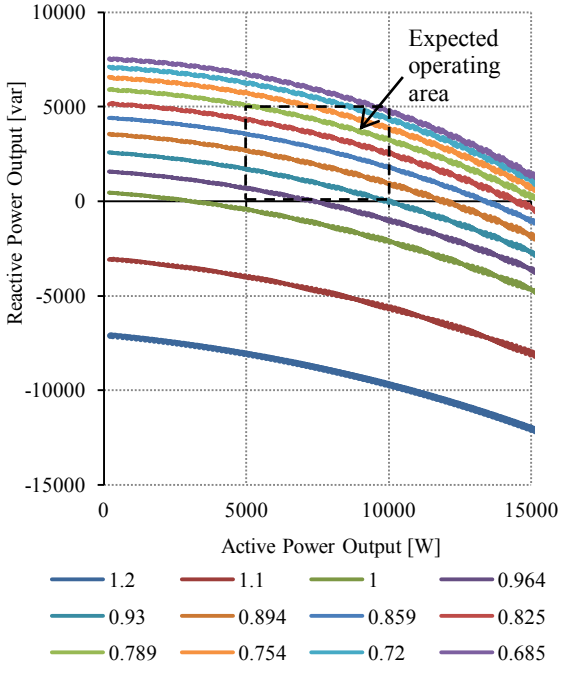

Figure 9.21: Simulated reactive power output versus active power output with terminal voltage as a parameter.

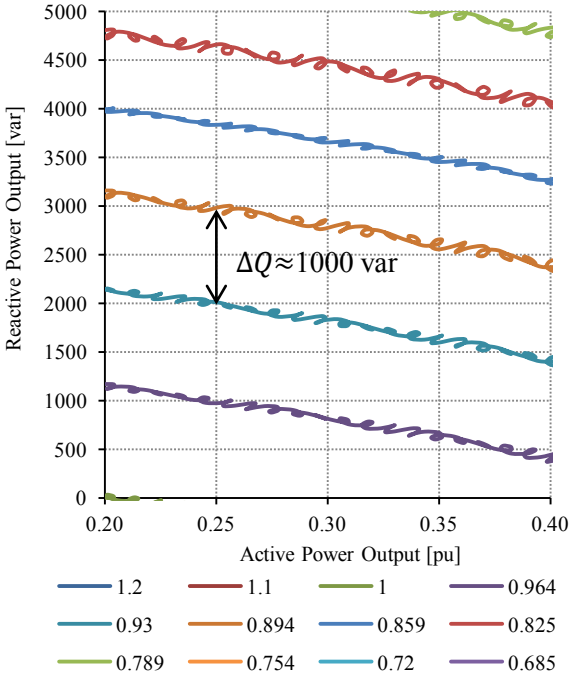

Figure 9.22: Extract of the simulated reactive power output in the expected operating region with terminal voltage as a parameter.

9.5.1. Single capacitor bank

For the case when using a single capacitor bank to provide additional reactive power, the capacitor bank must be rated to deliver $\Delta Q/2$ (500 var). The logic behind this is illustrated in Figure 9.23. If for instance tap 3 is conducting and the capacitor bank is active, the controller does not need to change a tap until the error in reactive power exceeds $\Delta Q/2$ var.

Assuming that a delta connected capacitor bank is used the size of a single capacitor can be calculated using (9.1),

$$C_{\Delta 1} = \frac{\Delta Q/2}{3\omega v_{LL}^2} = 3.31\ \mu\text{F}\ , \tag{9.1}$$

where $\Delta Q/2$ is the reactive power delivered by the capacitor bank, ω is the electrical frequency and v_{LL} is the line-to-line voltage applied to the capacitor bank.

9.5.2. Two capacitor banks

The control accuracy can be increased by implementing a second capacitor bank rated to half the reactive power of the previous bank ($\Delta Q/4$ or 250 var). The effect of adding a second capacitor bank on the control accuracy is illustrated in Figure 9.24. Assuming that a delta connected capacitor bank is used the size of a single capacitor in the second capacitor bank can be calculated using (9.2),

$$C_{\Delta 2} = \frac{\Delta Q/4}{3\omega v_{LL}^2} = 1.66\ \mu\text{F}, \tag{9.2}$$

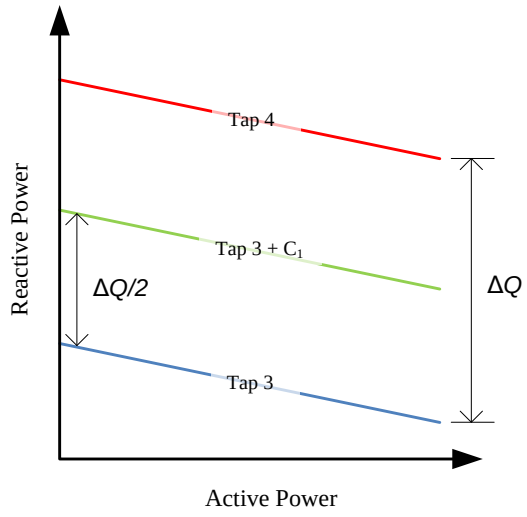

Figure 9.23: Reactive power control resolution using a single capacitor bank.

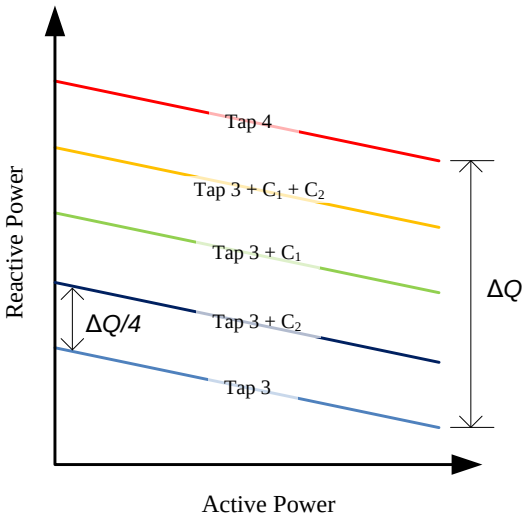

Figure 9.24: Reactive power control resolution using two capacitor banks.

9.5.3. Standard capacitor sizes

The capacitor sizes as determined in (9.2) and (9.3) are not commercially available. The closest available capacitors are 3.3 µF and 1.5 µF.

9.6. Addressing transients associated with capacitor switching

One of the major problems related to the use of switched shunt capacitor is high frequency transients that occur due to the inrush current of the capacitor.

9.6.1. Transients

When a capacitor bank is energized, transient oscillations occur between the capacitor bank and the system, the system may include capacitor banks that have already been energized. When a capacitor bank is energized near a capacitor bank that is already energized, common in multi-step automatic capacitor banks, the energized bank dumps high frequency high magnitude current into the uncharged bank. This is known as back-to-back switching and can cause extreme overvoltages [45] [46] [47]. Depending on the position of the energized, and energizing, capacitor bank the magnification of transient voltages in one part of the system may also produce overvoltages in another part [48][49].

9.6.2. Factors that influence transients

There are various factors that influence the magnitude and frequency of the transients. The most notable being: capacitor size, system short circuit capacity at the switched capacitor, impedance between adjacent capacitor banks and the customer load characteristics [45] [49] [50]. As the capacitor bank size increases, the peak inrush current increases and the frequency decreases [47]. The voltage across the switch at the closing time will also determine the inrush current magnitude. Resistive loads will provide damping which reduces the magnitude of the energizing transient [45].

9.6.3. Effects of the transients

The energisation transients cause power quality issues. Due to the use of power electronics, customer loads are tending to become more sensitive to power quality issues. The problem increases if the customer uses low voltage capacitors for power factor correction [50]. Overvoltages may cause system flashovers, equipment damage [48] and cause protection devices to operate. Adjustable-speed drives are particularly sensitive to these transients [50]. Large transients will compromise system reliability, damage sensitive equipment and will lead to economic losses [45][47].

9.6.4. Limiting the transients caused by capacitor switching

Two methods for decreasing the transient response are investigated. One method is to include closing resistors as shown in Figure 9.25(a) [45][48] [50]. A resistance value equal to halve the positive sequence capacitive reactance is the optimal value to limit the transient voltages at the switch [48]. This is a difficult solution to implement due to the unavailability of optimal sized resistors for distribution switching devices [45][50].

A better method is synchronized switching, where the switches are closed when there is no voltage across the switch terminals. This method can easily be implemented using solid-state switches, shown in Figure 9.25(b). Vacuum switches and vacuum breakers are the only conventional switches, to the knowledge of the author, that operate fast enough to implement this method [**2**][46][50].

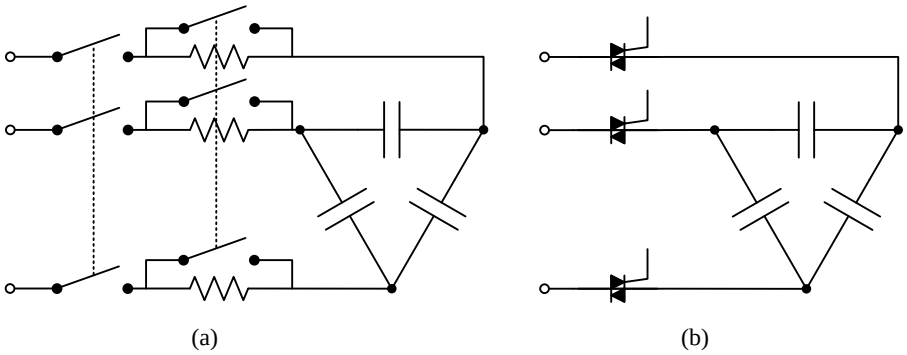

Figure 9.25: Capacitor inrush current limiting resistor circuits.

9.6.5. Simulated transient during shunt capacitor switching

The transients associated with switching the capacitors (sizes as determined in 9.5.3) are simulated using MGSV. Figure 9.26 shows the per phase circuits used to determine the transient. Initially only a single capacitor bank is energized as showed in Figure 9.26(a). Thereafter the circuit showed in Figure 9.26(b) is simulated.

Rated voltage (230 V_{rms} @ 50 Hz) is generated with the ideal voltage source. The source impedance is 0.15 + 0.15j. A base current value of 22 A is used to determine the per unit current showed in the results. The applicable switch is closed when the voltage waveform is at a peak value, this will cause the greatest inrush current. The capacitor values given in 9.5.3 are for a delta connected bank. These are per phase simulations, so the per phase equivalent capacitor values are used (4.5 μF and 9.9 μF).

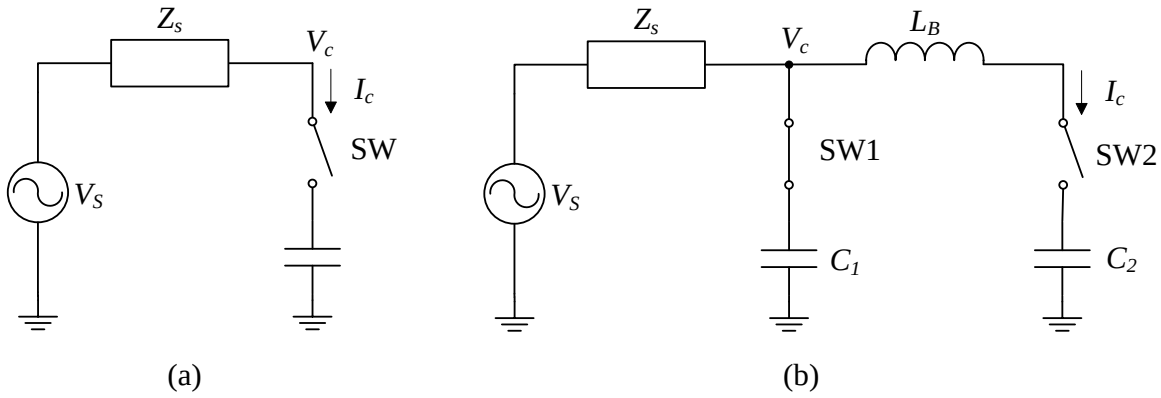

Figure 9.26: Per phase circuit simulated to determine capacitor switching transient; (a) single capacitor bank, (b) including a pre-energised capacitor bank

Single capacitor bank

The circuit in Figure 9.26(a) is simulated. Two simulations were run, one for each capacitor size. The results for both simulations are shown in Figure 9.27 to Figure 9.30. From the results the high transients can be observed. The currents reach steady state after about a half cycle (10 ms). So although the currents and voltage transients are relatively high, they should not damage surrounding equipment due to their short duration.

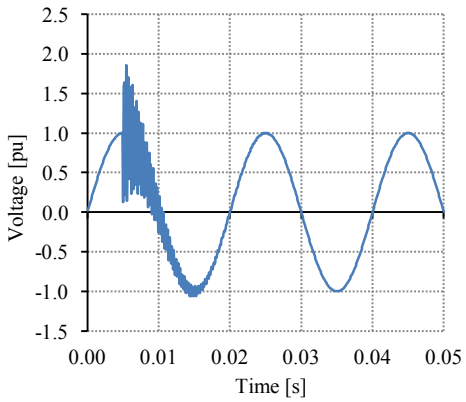

Figure 9.27: Simulated per phase voltage waveform when a 4.5 µF capacitor is energised.

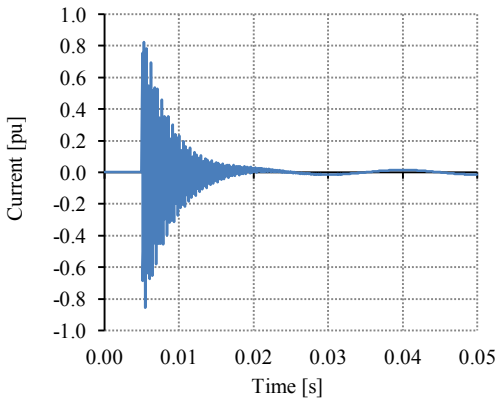

Figure 9.28: Simulated line current waveform when a 4.5 µF capacitor is energised.

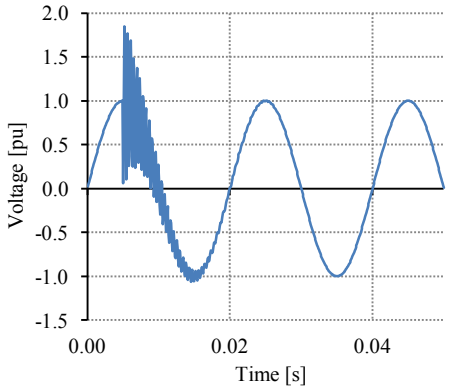

Figure 9.29: Simulated per phase voltage waveform when a 9.9 µF capacitor is energised.

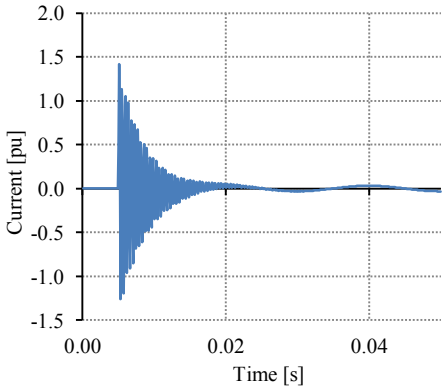

Figure 9.30: Simulated line current waveform when a 9.9 µF capacitor is energised.

Two capacitor banks

The circuit in Figure 9.26(b) is simulated. Two simulations were run. In the first simulation the 4.5 µF capacitor is switched while the 9.9 µF capacitor is energised. In the second simulation the 9.9 µF capacitor is switched while the 4.5 µF capacitor is energised. The voltage and currents as indicated in Figure 9.26(b) is shown for both simulations in Figure 9.31 to Figure 9.34. When comparing the transients to those in the previous simulation it is apparent that the inrush current amplitude is higher, but the effect of the voltage is less. This is due to the fact that the high frequency inrush current is delivered by die nearby energised capacitor bank and not the voltage source.

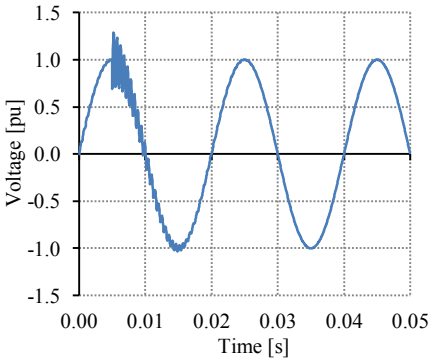

Figure 9.31: Simulated per phase voltage when closing a 4.5 µF capacitor while the 9.9 µF capacitor is energised.

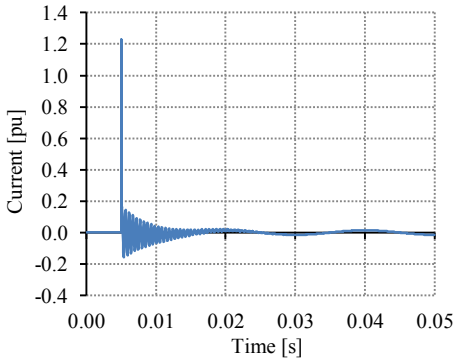

Figure 9.32: Simulated capacitor current when closing a 4.5 µF capacitor while the 9.9 µF capacitor is energised.

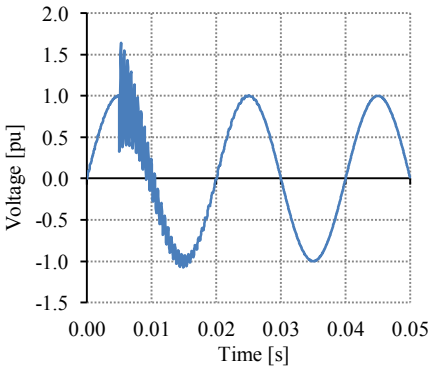

Figure 9.33: Simulated per phase voltage when closing a 9.9 µF capacitor while the 4.5 µF capacitor is energised.

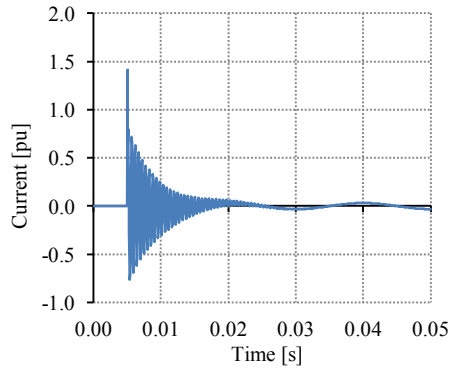

Figure 9.34: Simulated capacitor current when closing a 9.9 µF capacitor while the 4.5 µF capacitor is energised.

Recommendations

If the transient prove troublesome during practical testing, one of the methods for minimizing transients should be implemented. The cheapest option would be to implement closing resistors.

9.7. Power factor control simulation using a combination of OLTC and capacitors

The circuit shown in Figure 9.35 is used to control the power factor during simulation. The assumption is made that the grid voltage is constant while the generator terminal voltage is controlled with the OLTC. The size of the capacitor banks are as discussed in 9.5.3. The rest of the circuit is the same as for the simulation where only the OLTC transformer was used to control the power factor. Simulations are run to determine if the system will reach the reactive power and power factor control requirements as specified in sections 9.2.1 and 9.2.3. Using the power factor control function, the WEF must be able to control the power factor between 0.975 lagging and 0.975 leading. Using the reactive power control function the WEF is required to be able to deliver 3.3 kvar and also absorb 3.3 kvar when the active power is higher than 0.2 pu. The WEF must be able to control the reactive power with deviation of no more than 75 var.

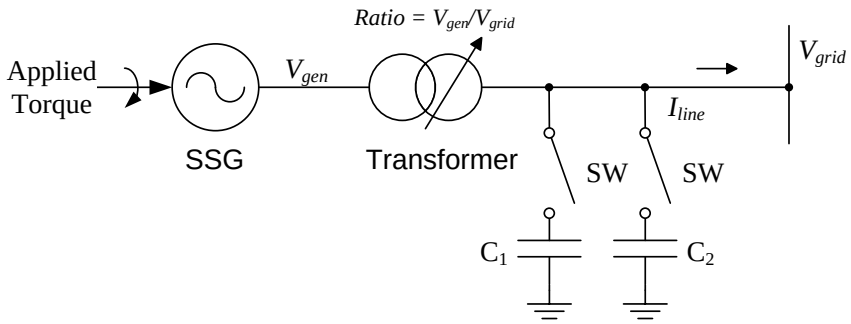

Figure 9.35: Proposed circuit for controlling the reactive power of a SSG

9.7.1. Simulation with unity power factor as set-point

In this simulation the controller is programmed to maintain unity power factor for all active power levels. Figure 9.36 shows the simulated power factor for all active power levels.

An improvement can be seen when comparing the results in Figure 9.36 to those in Figure 9.37. There are however a few power levels where the controller is unable to make a decision as to what capacitor-tap combination to use, 0.55, 0.78 and 0.92 p.u. active power. This is caused by the fact that the value with which the reactive power changes as the terminal voltage changes is not constant throughout the active power range.

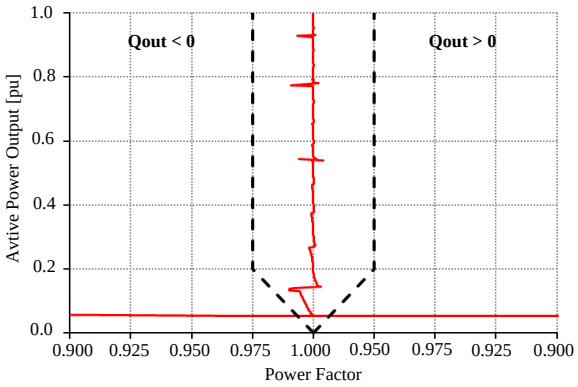

Figure 9.36: Simulation results for power factor control using the combination only the OLTC with two capacitor banks

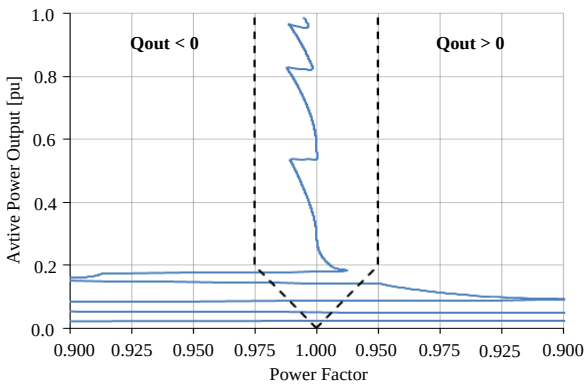

Figure 9.37: Simulation results for power factor control when using the only the OLTC.

9.7.2. Simulation with power factor of 0.975 lagging as set-point

In the next simulation the controller is set to keep the power factor at 0.975 lagging. The simulated power factor measured at the grid connection point is shown in Figure 9.38. As can be seen in Figure 9.38 the controller is trying to keep the power factor at 0.975 lagging. From the results it is apparent that the system lacks the required ability to maintain a constant power factor value.

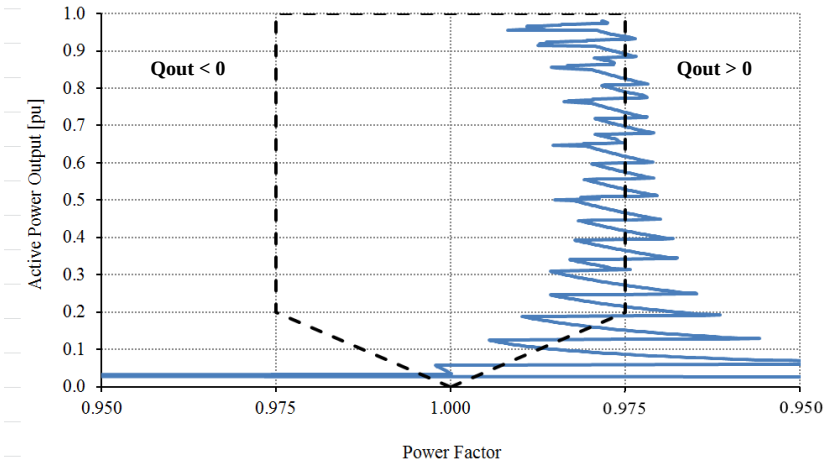

Figure 9.38: Simulation results for power factor control using the combination of the OLTC with capacitor banks with the set-point set to 0.975 leading.

9.7.3. Simulation with power factor of 0.975 leading as set-point

In the next simulation the controller is set to keep the power factor at 0.975 lagging. The simulated power factor measured at the grid connection point is shown in Figure 9.39. As can be seen in Figure 9.39 the controller is trying to maintain a leading power factor of 0.975 but is unable to do so with the required accuracy.

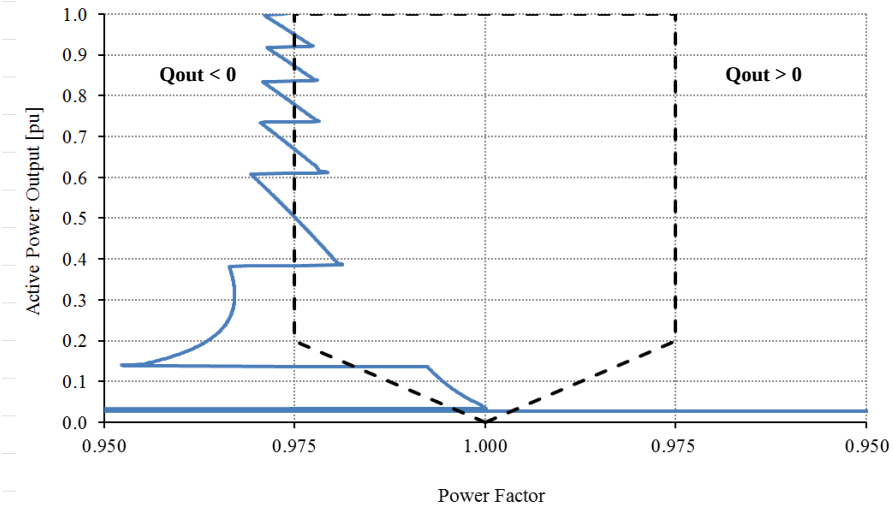

Figure 9.39: Simulation results for power factor control using the combination of the OLTC with capacitor banks with the set-point set to 0.975 lagging.

9.7.4. Simulation with maximum reactive power delivered as set-point

In the next simulation the controller is set to deliver the 3.3 kvar. The simulated output reactive power measured at the grid connection point is shown in Figure 9.40. As can be seen in Figure 9.40 the controller is trying, with limited success to maintain a reactive power output of 3.3 kvar. Although the reactive power is in the region of 3.3 kvar, the deviation is more than the required 75 var.

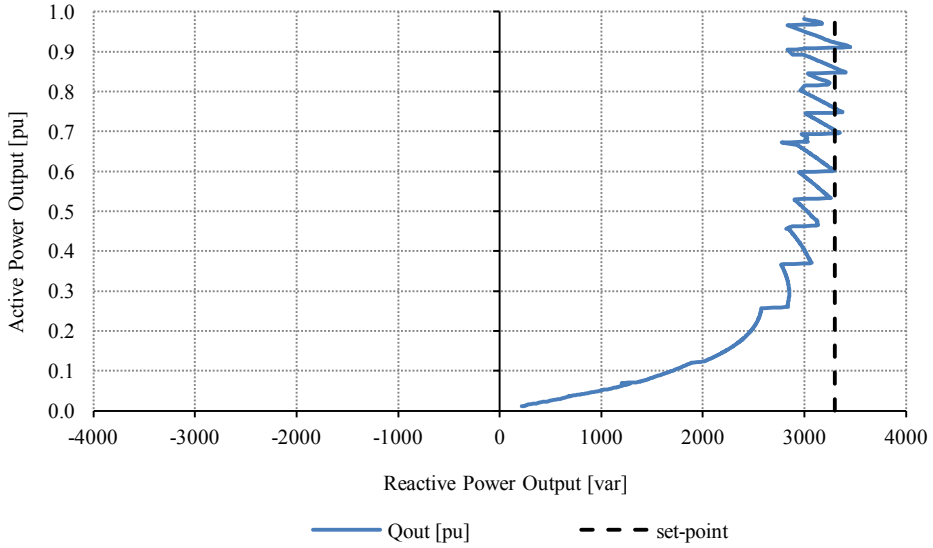

Figure 9.40: Simulation results showing the reactive power output when using the combination of the OLTC with capacitor banks with the set-point set to the maximum required reactive power delivered.

9.7.5. Simulation with maximum reactive power absorbed as set-point

In the next simulation the controller is set to absorb the 3.3 kvar. The simulated output reactive power measured at the grid connection point is shown in Figure 9.41. Again the controller is unable to maintain the required accuracy.

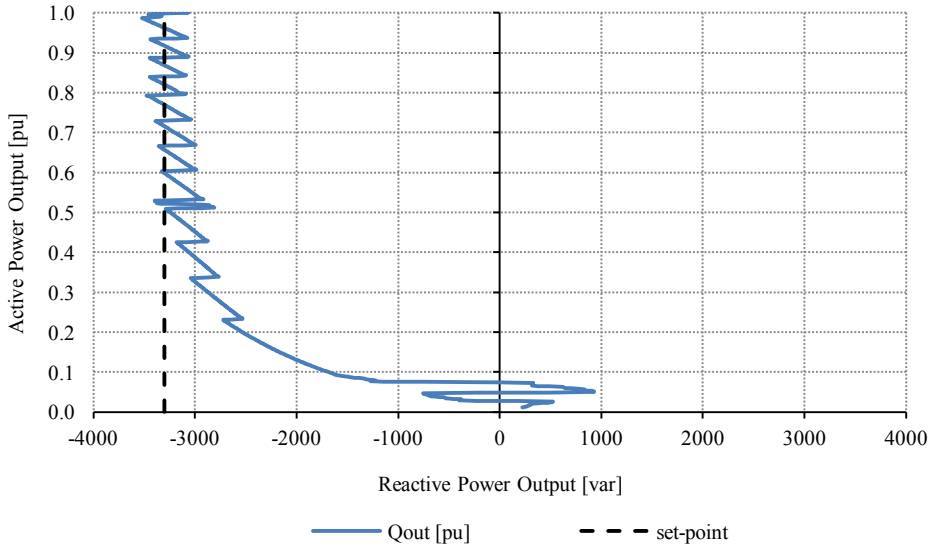

Figure 9.41: Simulation results showing the reactive power output using the combination of the OLTC with capacitor banks with the set-point set to the maximum required reactive power absorbed.

9.8. Conclusion regarding reactive power control

From the simulation results an improvement can be seen when using capacitors with the OLTC to control the reactive power output of the WEF. However, using the current transformer, two capacitor banks will not be able to provide adequate reactive power control resolution. Using the current transformer at least four shunt capacitor banks, with their capacitive values determined using the method described in section 9.5, are needed before the maximum reactive power deviation is smaller than 75 var. It is recommended that for the next iteration of this reactive power control device, the voltage change per tap change not exceed 1% nominal voltage. This will dramatically increase the control resolution of the system.

Chapter 10. Practical results of the OLTC

This chapter contains all the practical results regarding the OLTC transformer. During these tests the 15 kW SSG is driven by a 45 kW induction motor fed by a 37 kW Allen-Bradley variable speed drive. During these tests grid synchronisation of the generator is done manually. The aim of this chapter is to evaluate the performance and viability of the designed system.

10.1. Soft-starting the transformer

The relevant circuit components for describing the practical soft-start procedure are shown in Figure 10.1. The transformer is soft-started by first selecting tap 3 (nominal voltage). After waiting 0.5 seconds the thyristors are turned on with a 90˚ fire angle. After 0.5 seconds the thyristors start to conduct the full load. After another 0.5 seconds the bypass switch is closed and the thyristors stop conducting current. Thereafter the thyristor gate is set to low and the thyristors cannot turn on again.

This procedure was conducted multiple times to ensure that the protection breaker does not trip. The lowest and highest measured inrush current is shown in Figure 10.2 and Figure 10.3 respectively. The variation in inrush current is most probably due to different residual flux values in the transformer core at the time when the transformer is turned on.

Various attempts were made to connect the transformer to the grid without using the soft-start procedure. They were all unsuccessful as the protection breaker keeps tripping due to over currents. The breaker allows for inrush current of up to 10 times the rated current for 0.1 seconds before disconnecting. It can be assumed that the transformer inrush current, without soft-starting, would exceed the conduction rating of the switches and other component.

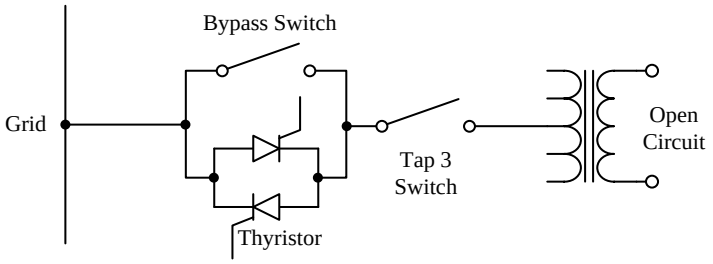

Figure 10.1: Per phase circuit for describing the practical soft-start procedure

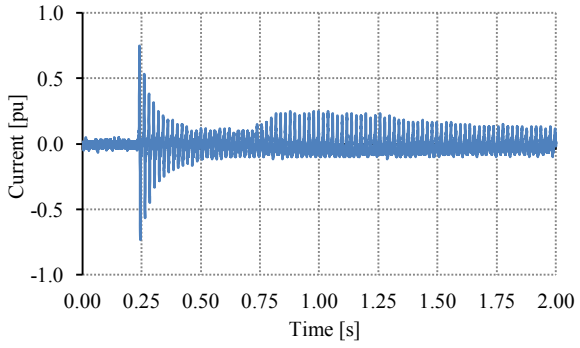

Figure 10.2: Smallest inrush measured current during practical testing of the transformer soft-start procedure

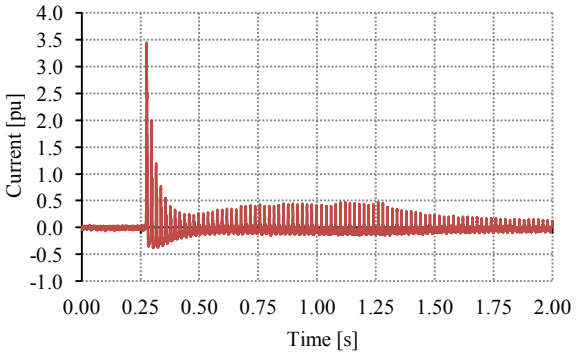

Figure 10.3: Largest measured inrush current during practical testing of the transformer soft-start procedure

10.2. SSG efficiency and power factor angle

The change in the power factor angle and efficiency of the SSG is investigated in this section. The power factor at the grid connection point is measured for various voltages while the applied torque to the generator is increased. The efficiency of the generator is also measured at rated torque for the relevant terminal voltage.

Figure 10.4 shows how the reactive power output of the SSG increases with decreasing terminal voltage. The decrease in generator efficiency at non-nominal terminal voltage values is shown in Figure 10.5. These results confirm the suspicion with regards to the decrease in that the generator efficiency while using the OLTC to control the output reactive power of the generator.

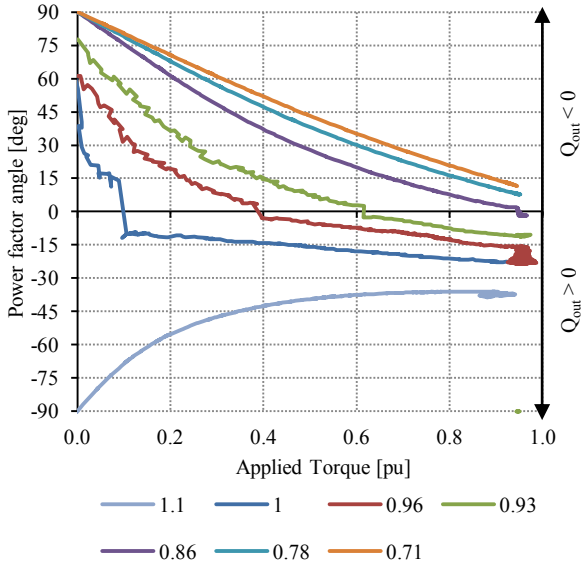

Figure 10.4: Measured current angle of the stator with terminal voltage a parameter in per unit.

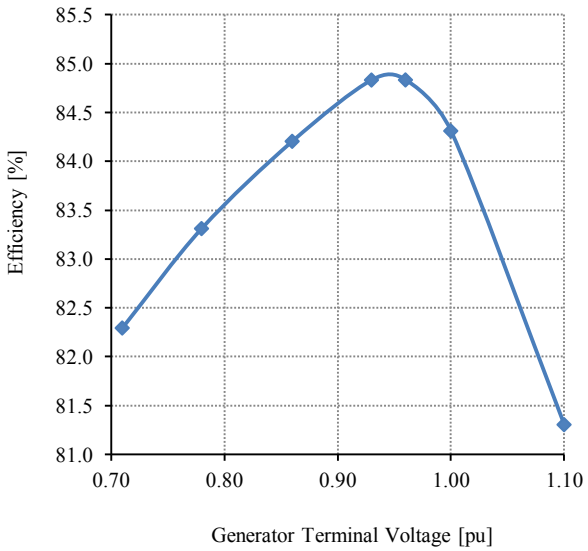

Figure 10.5: Measured SSG efficiency at rated torque.

10.3. Arcing in the diverter bypass switch

To determine if there is considerable arcing in the diverter bypass switch the current through and the voltage over the switch is measured as shown in Figure 10.6. Arcing is most prevalent during the opening of a switch conducting current. Figure 10.7 shows the measured current through and the voltage over the bypass switch as it opens while conducting rated current.

By integrating the product of the voltage and current waveform the energy dissipated in the switch is calculated as 2 mJ. This value is in line with previous research and testing done by [28]. Thus very little arcing occur in the bypass switch and the switch is expected to have a very long lifetime.

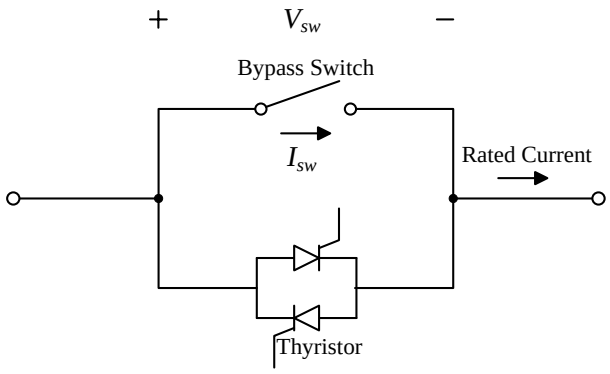

Figure 10.6: Per phase circuit for measuring the possible arcing in the diverter bypass switch

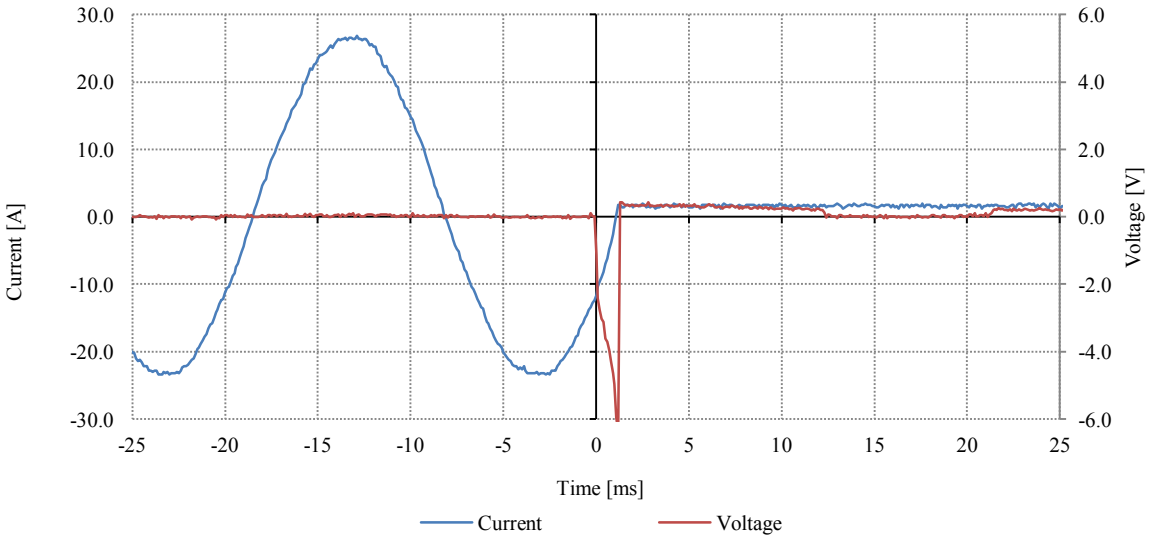

Figure 10.7: Measured current through and voltage over the bypass switch as it "breaks" rated current.

10.4. Generator voltage and currents during a switching operation

The goal of this test is to determine the transients of the generator during a tap operation. The generator per phase voltage and line current is measured, as shown in Figure 10.8, during a tap change at rated power. Figure 10.9 shows the small decrease in terminal voltage, without interrupting the line current. Even though the voltage and current waveforms are not in phase there are no voltage spikes as simulated in Figure 8.24.

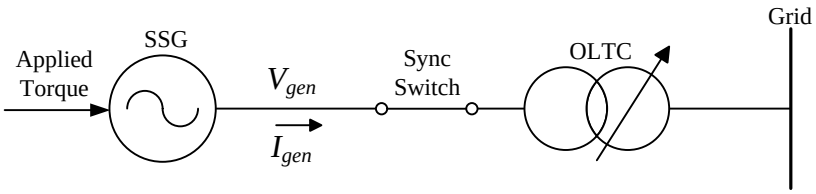

Figure 10.8: Per phase circuit for measuring the generator voltage and current during a switching operation

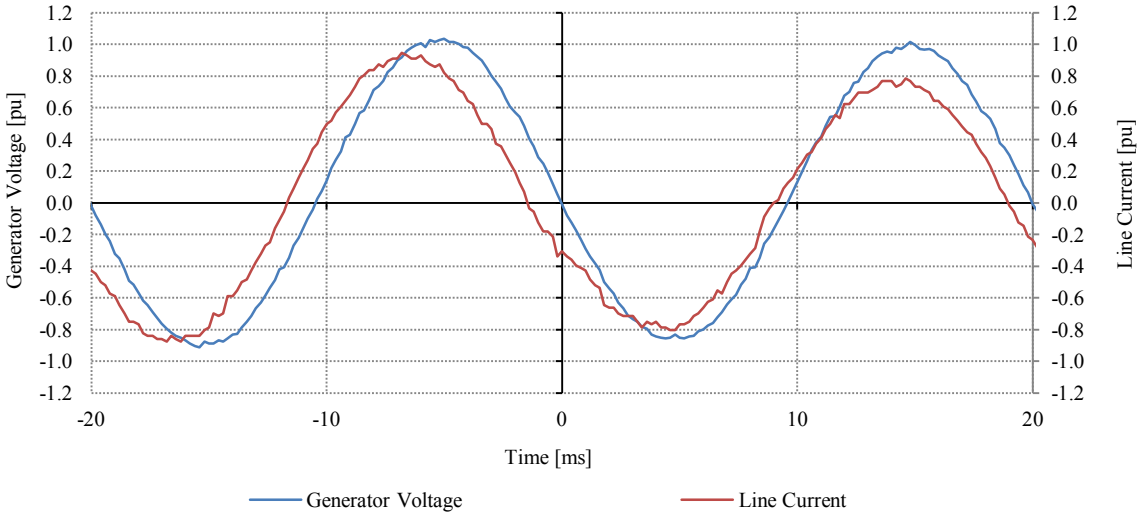

Figure 10.9: Measured generator per phase voltage and line current during a tap change, decreasing the terminal voltage by 0.03 pu at time zero.

10.5. Reactive power control using the OLTC

As shown in Figure 10.10 the generator is connected to the grid (400V) via the OLTC transformer. At the start of this test the generator is already synchronised with the electrical network. The OLTC controller is set to provide unity power factor. The applied torque is increased slowly from zero to rated torque (100 N.m.). The test was repeated various times. The results for two of the tests are shown in Figure 10.11. The lower limit of the no-operation bandwidth is decreased from 1000 var in test 1 to 650 var in test 2. This allowed for better power factor results at higher power levels.

From the test result it is apparent that the reactive power output of the SSG can be controlled with an OLTC transformer. The control resolution is very rough and reactive power control using a stand-alone OLTC does not meet the accuracy requirements as specified in the grid code.

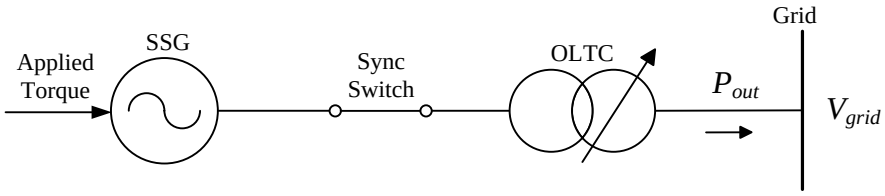

Figure 10.10: Generator connected to the grid via an OLTC transformer for reactive power control test

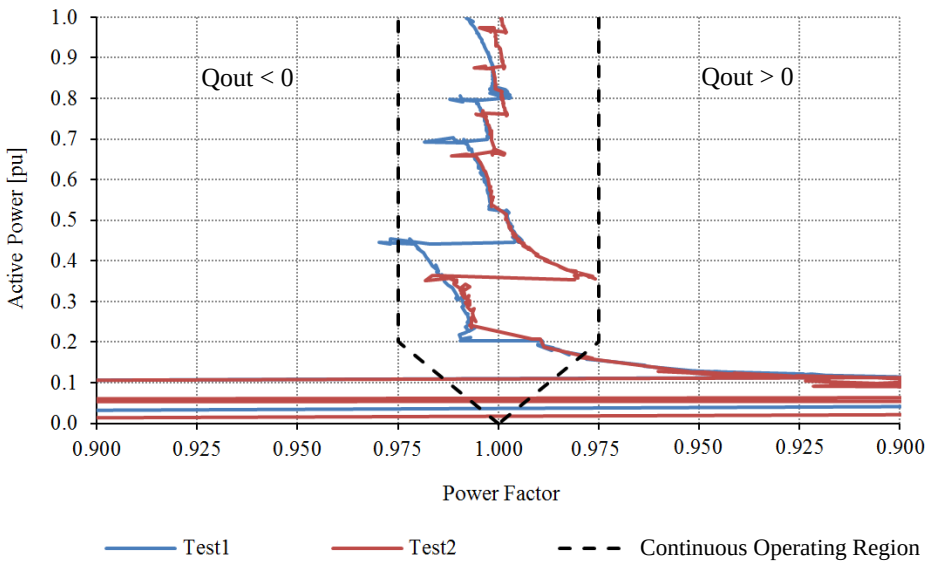

Figure 10.11: Practical results for power factor control using only the OLTC

Chapter 11. Conclusion and recommendations

This chapter contains the final conclusions with regards to the various aspects of the grid code investigated in this study. A suggestion is also made with regards to a possible design goal for the next iteration of the SSG.

11.1. Conclusions

11.1.1. Active power curtailment

At this moment the SSG WTG does not comply with the active power curtailment requirements as specified in the grid code of South Africa. At present there is no dedicated system to limit the active power output. The current thyristor based electric braking circuit, used during speed control for grid synchronisation, can be used to limit the output power, however this circuit is not currently set up for this purpose and according to the simulation results using the thyristor braking circuit will create large harmonics on the current waveform.

An IGBT-rectifier based speed control circuit is proposed as an alternative method of limiting the active power output. According to simulation results the IGBT braking circuit show better current waveform characteristics when compared to the thyristor braking circuit. The IGBT braking circuit can also replace the thyristor braking circuit during speed control for the grid synchronisation process, without excessive modification to the existing controller functions in the GCC.

Both the thyristor based and the IGBT-rectifier based electric braking circuit allow for very fast power curtailment. By implementing either braking circuit the SSG WTG will comply with the grid code requirement with regards to the response time and active power limiting capacity.

11.1.2. Frequency disturbance response

The dynamic response of the SSG WTG due to grid frequency disturbances is determined via simulation. Grid frequency variations cause over current transients and the magnitude of these transient are directly proportional to the rate at which the frequency changes. The grid code specifies that a WEF be designed to cope with frequency changes of up to 0.5 Hz/second. Simulation results showed that a 10% increase in line current can be expected during such a frequency disturbance. Due to the relatively short duration for which a WEF must be connected to the grid during large frequency disturbances, the overcurrent should not cause any damage to the system components.

Over frequencies will cause up to a 4% increase in the turbine speed of the WTG. Since it is normal practice to design a wind turbine with some safety factor with regards to rotational speed, to allow for times when the actual wind speed is higher than the rated wind speed, the small increase in turbine speed is not a concern.

From the simulation results it seems that the SSG WTG will not have a problem complying with the connection conditions as specified in the grid code.

11.1.3. Reactive power control method

An OLTC transformer utilizing a solid-state assisted diverter circuit was developed in this study. The purpose of the OLTC transformer is to control the terminal voltage of the generator in order to change the excitation mode of the SSG. In this manner the reactive power output of the generator can be controlled.

Both simulation and measured results show that the OLTC transformer using a solid-state assisted diverter circuit is a viable method of controlling the terminal voltage without interrupting the load current. Measured test also show that there is very little arcing in the bypass switches, leading to longer intervals between maintenance.

Although the current OLTC can change the reactive power output of the generator, the current control resolution is very rough and does not meet the accuracy requirements as specified in the grid code. A method of using small shunt capacitors to provide additional reactive power support in between consecutive tap changes is evaluated in simulation. The simulation results show an improvement in the reactive power control resolution of the system.

11.2. Recommendation

11.2.1. Improving the reactive power control resolution

Consider Figure 11.1 where ΔQ is the change is output reactive power due to a control decision, in this case a tap change. The grid code requires that the reactive power output not deviate by a value of more than 0.5% the rated active power of the WEF.

This means that the required maximum change in reactive power due to a control decision, $\Delta Q'_{pu}$, is 0.005 pu calculated with regards to the rated active power. If the per unit change in the reactive power due to a per unit change in terminal voltage, $\frac{\Delta Q_{pu}}{\Delta V_{pu}}$, is known the maximum change in terminal voltage, $\Delta V'_{pu}$, can be determined as shown in (11.1) – (11.2),

$$\frac{\Delta Q_{pu}}{\Delta V_{pu}} = \frac{\Delta Q'_{pu}}{\Delta V'_{pu}}, \tag{11.1}$$

$$\Delta V'_{pu} = \Delta Q'_{pu} \frac{\Delta V_{pu}}{\Delta Q_{pu}}. \tag{11.2}$$

During tests the $\frac{\Delta Q_{pu}}{\Delta V_{pu}}$ for the current SSG is determined to be 3.45. Thus, if no additional reactive power compensation devices are used in the system, the required change in voltage step size is determined to be 0.01725 pu or 6.9 V_{LL}. Since it is not conceivable that a tapped transformer will be built with such small voltage steps, additional reactive power compensation devices will need to be added to the system.

For each capacitor bank added the control resolution increases two fold. If four capacitor banks are used, with reactive power ratings determined using the method in 9.5, the required control resolution can be achieved with transformer voltage steps of 0.276 pu. This is a more realistic voltage step size for a tapped transformer.

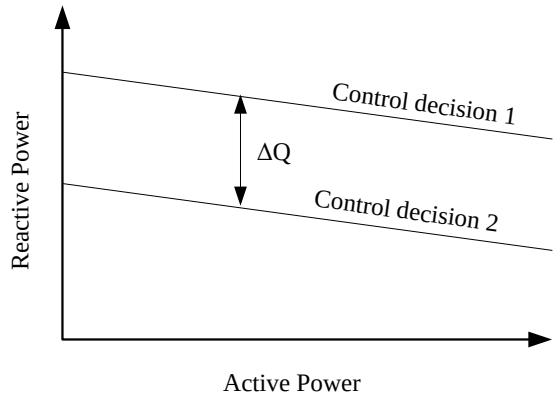

Figure 11.1: Reactive power control resolution.

11.2.2. Suggestion regarding the future design of the SSG

Figure 11.2 shows the proposed efficiency and power factor angle relationship for a SSG operating at a certain power level; between 20 and 40% rated active power output. The generator should be designed in such a manner that the power factor angle is unity at nominal voltage. This will minimize the negative effect with regards to lower efficiency associated with the changes in terminal voltage due to the reactive power control mechanism developed in this study.

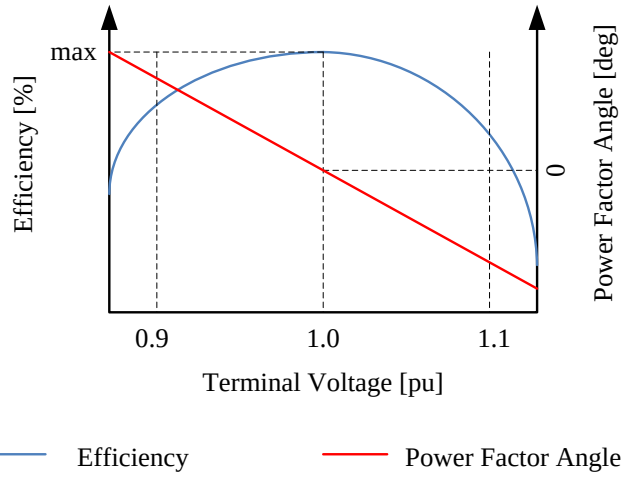

Figure 11.2: Proposed design goal for future SSG models with regards to the efficiency-power factor angle relationship at a predetermined power level.

11.3. Closing remarks

Throughout this study various aspects of the proposed SSG based WTG has been investigated. The main focus was the evaluation of a method by which the reactive power output of the wind farm is controlled using an OLTC transformer. Preliminary tests showed that it is indeed possible to control the reactive power output of the SSG by changing the excitation mode of the generator. Further study is required to determine the application of this technique on larger wind farms.

Chapter 12. References

[1] The World Bank, January 2011. [Online]. Available: http://data.worldbank.org/data-catalog/world-development-indicators?cid=GPD_WDI.

[2] World Wind Energy Association, "World Wind Energy Report 2010," Bonn, Germany, 2011.

[3] A. Niez, "Comparative study on rural electrification policies in emerging economies," OECD Publishing, 2010.

[4] J. Quilter, May 2012. [Online]. Available: http://www.windpowermonthly.com/news/1132927/South-Africa-approves-562MW-wind-projects.

[5] April 2012. [Online]. Available: http://www.jobyenergy.com.

[6] March 2012. [Online]. Available: http://www.altaerosenergies.com/.

[7] D. M. Dodge, January 2011. [Online]. Available: http://telosnet.com/wind/index.html.

[8] A. D. Hansen and H. a. L. H., "Market penetration of wind turbine concepts over the years," in *Proc. of the European Wind Energy Conference & Exhibition*, Milan, Italy, 2007.

[9] A. Causebrook, D. Atkinson and A. Jack, "Fault Ride-Through of Large Wind Farms Using Series Dynamic Braking Resistors (March 2007)," in *Power Systems, IEEE Transactions on*, 2007.

[10] J. H. J. Potgieter, A. N. Lombard, R.-J. Wang and M. J. Kamper, "Evaluation of permanent magnet exited induction generator for renewable energy applications," in *Southern African Universities Power Engineering Conference*, Stellenbosch, Jan 2009.

[11] J. H. J. Potgieter and M. J. Kamper, "Design of New Concept Permanent Magnet Induction Wind Generator," in *Energy Conversion Congress and Exposition (ECCE), 2010 IEEE* , 2010.

[12] P. Fairlwy, "Steady as she blows [wind power, energy storage]," *Spectrum, IEEE,* vol.

40, no. 8, pp. 35 - 39, August 2003.

[13] N. Jenkins, “Electrical Design of Wind Farms,” in *Athens Power Tech, 1993. APT 93. Proceedings. Joint International Power Conference*, 5 - 8 Sep 1993.

[14] U. Hoffmann, P. Bouwer and M. Kamper, “Direct grid connection of a slip-permanent magnet wind turbine generator,” in *Energy Conversion Congress and Exposition (ECCE)*, Phoenix, USA, 2011.

[15] U. Hoffmann and M. .. Kamper, “Low Voltage Ride-Through Compensation for a Slip-Permanent Magnet Wind Turbine Generator,” in *Southern African Universities Power Engineering Conference*, Cape Town, 2011.

[16] L. H. Hansen, L. Helle, F. Blaabjerg, E. Ritchie, S. Munk-Nielsen, H. Bindner, P. Sørensen and B. Bak-Jensen, “Conceptual survey of Generators and Power Electronics for Wind Turbines,” 2001.

[17] P. Bouwer, J. Potgieter and M. Kamper, “Modelling and dynamic performance of a direct-drive direct-grid slip permanent magnet wind generator,” in *Electric Machines & Drives Conference (iemdc), IEEE*, Niagara Falls, Canada, 2011.

[18] S. J. Chapman, Electric Machinery Fundamentals, 4th ed., New York: McGraw-Hill, 2005.

[19] U. Hoffmann, “Direct Grid Connection and Low Voltage Ride-Through for a Slip Synchronous-Permanent Magnet Wind Turbine Generator,” Stellenbosch, 2012.

[20] NERSA, “Grid code requirement for wind energy facilities connected to distribution or transmission systems in South Africa,” July 2012. [Online]. Available: http://www.nersa.org.za.

[21] O. B. a. Z. M. M. Kesraoui, “Power Control of a PMSG based Wind Turbine System Above Rated Wind Speed,” in *International Renewable Energy Congress*, Sousse, Tunisia, November 2010.

[22] H. Barnard, “Steekhoekbeheer van 'n 50 kW Windgenerator,” Stellenbosch, 2011.

[23] P. Bauer and S. de Haan, “Solid State Tap Changers for Utility Transformers,” in *AFRICON, IEEE 1999*, Cape Town, South Africa, 1999.

[24] J. Serdyn, “Electronic Voltage Regulation Technology for rural Electrification,” Stellenbosch, South Africa, 2008.

[25] M. Heathcote and D. Franklin, The J & P Transformer Book, 12th ed., Oxford: Reed Educational and Professional Publishing Ltd, 1998.

[26] D. J. Rogers, “Hybrid and Thin Power Electronics for Electrical Power Networks,” Londen, March 2011.

[27] D. Gao, “A Novel Thyristor Assisted Diverter Switch for On Load Transformer Tap Changer,” in *Transmission and Distribution Conference and Exhibition 2002: Asia Pacific. IEEE/PES*, Yokohama, Japan, 2002.

[28] D. J. Rojers and T. C. Green, “A Hybrid Diverter Design for Distribution Level On-load Tap Changers,” in *IEEE Energy Conversion Congress & Expo*, Atlanta, USA, 2010.

[29] D. J. Rojers and T. C. Green, “Zero-Current Zero-Voltage Switching for On-Load Tap Changers,” in *IET Power Electronics Machines and Drives*, Brighton, UK, 2010.

[30] The Electic Motor Education and Research Foundation. CD-ROM, Lamination steels third edition, 3rd ed., S. Sprague, Ed., 2007.

[31] F. Asghar and K. Basu, “Reduction of three-phase transformer magnetizing inrush current by use of point on wave switching,” in *2009 IEEE Student Conference on Research and Development (SCOReD)*, Serdang, Malaysia., 2009.

[32] Tyco Electronics, [Online]. Available: http://relays.tycoelectronics.com/appnotes/app_pdfs/13c3206.pdf.

[33] N. Jenkins, “Embedded generation,” *Power Engineering Journal,* vol. 9, no. 3, pp. 145 - 150, June 1995.

[34] J. D. Glover, M. S. Sarma and T. J. Overbye, Power Systems Analysis and Design, 4th ed., H. James, Ed., Thomson Corporation, 2008.

[35] L. H. Hansen, L. Helle, F. Blaabjerg, E. Ritchie, S. Munk-Nielsen, H. Bindner, P. Sørensen and B. Bak-Jensen, “Conceptual survey of Generators and Power Electronics for Wind Turbines,” Roskilde, Denmark, December 2001.

[36] A. E. Fitzgerald, C. J. Kingsley and S. D. Umans, Electric Machinery, 6th ed ed., New York: McGraw-Hill, 2003.

[37] C. Corvin, "SLAC synchronous condenser," in *Particle Accelerator Conference, Proceedings of the 1995*, 1-5 May 1995.

[38] P. L. Alger, "Synchronous Condensers," in *Transactions of the American Institute of Electrical Engineers* , 1928.

[39] Ideal Electric, [Online]. Available: http://www.fishermensenergy.com/dms/showfile.php?id=286.

[40] C. Chompoo-inwai, C. Yingvivatanapong, K. Methaprayoon and W.-J. Lee, "Reactive compensation techniques to improve the ride-through of induction generators during disturbance," *Industry Applications Conference, 2004. 39th IAS Annual Meeting. Conference Record of the 2004 IEEE,* vol. 3, no. Seattle, USA, pp. 2044- 2050, Oct. 2004.

[41] M. Elnashar, M. Kazerani, R. El Shatshat and M. Salama, "Comparative evaluation of reactive power compensation methods for a stand-alone wind energy conversion system," *Power Electronics Specialists Conference, 2008. PESC 2008. IEEE,* no. Rhodes, Greece, pp. 4539 - 4544, 15-19 June 2008.

[42] H. Wang, "Applications of damping torque analysis to STATCOM control," *International Journal of Electrical Power & Energy Systems,* vol. 22, no. 3, pp. 197 - 204, March 2000.

[43] C. Schauder, M. Gernhardt, E. Stacey, T. Lemak, L. Gyugyi, T. Cease and A. Edris, "Development of a ±100 MVAr static condenser for voltage control of transmission systems," in *Power Delivery, IEEE Transactions on*, 1995.

[44] J. Bebic, June 2012. [Online]. Available: http://hpfc.ca/facts.html.

[45] D. Coury, C. dos Santos and M. Tavares, "Transient analysis resulting from shunt capacitor switching in an actual electrical distribution system," in *Harmonics And Quality of Power, 1998. Proceedings. 8th International Conference*, Athens , Greece , 1988.

[46] Northeast Power Systems, Inc., October 2011. [Online]. Available: http://www.mty.itesm.mx/etie/deptos/ie/profesores/jabaez/clases/e074/parcial_3/Sobre

voltajes/switchingtransients.pdf.

[47] G. Gopakumar, H. Yan, B. A. Mork and K. K. Mustaphi, “Shunt capacitor bank switching transients: A tutorial and case study,” in *Minnesota Power Systems Conferenc*, Michigan, USA, 1999.

[48] A. J. Schultz, I. B. Johnson and N. R. Schultz, “Magnification of Switching Surges,” in *Power Apparatus and Systems, Part III. Transactions of the American Insitute of Electrical Engineers*, April 1958.

[49] P. Jota and S. Islam, “Effect of realistic system modelling on low-voltage capacitor transient overvoltages,” in *Generation, Transmission and Distribution, IEE Proceedings*-, Nov 1998.

[50] M. McGranaghan, R. Zavadil, G. Hensley, T. Singh and M. Samotyj, “Impact of utility switched capacitors on customer systems-magnification at low voltage capacitors,” in *Power Delivery, IEEE Transactions on,* , vol.7, no.2, pp.862-868, Apr 1992.

[51] NERSA, September 2011. [Online]. Available: http://www.nersa.org.za.

[52] B. Guru and H. Hiziroglu, Electromagnetic Field Theory Fundamentals, 2nd ed., Cambridge University Press, 2005.

[53] D. Povh and W. Schultz, “Analysis of Overvoltages Caused by Transformer Magnitizing Inrush Current,” in *IEEE Transactions on Power Apparatus and Systems*, 1978.

[54] Mohan, Undeland and Robbins, Power Electronics, 3rd ed., B. Zobrist, Ed., John Wiley and Sons, Inc, 2003.

[55] J. W. Nilsson and S. Riedel, Electric Circuits, 9th Edition ed., Prentice Hall, 2011, pp. 285 - 288, pp. 285 - 288.

[56] L. Gyugyi, C. Schauder and K. Sen, “Static synchronous series compensator: a solid-state approach to the series compensation of transmission lines,” in *Power Delivery, IEEE Transactions on*, Jan 1997.

[57] S. Javadi, B. Vahidi and S. Hosseinian, “Three phase transformer modeling with considiration the core effect,” in *International Conference on Electrical Machines and Systems, ICEMS 2008*, Wuhan, China, 2008.